Proceedings of

JSPS-CAS Core University Program Seminar on PWI/PFC and Fusion Technologies

Oct. 27-29, 2008, Huangshan, Anhui

Eds. Tomoaki Hino (Hokkaido Univ.) and Junling Chen (ASIPP)

JSPS-CAS Core University Program Seminar

on PWI/PFC and Fusion Technologies

Organized by Junling Chen, Institute of Plasma Physics, Chinese Academy of Science, and Tomoaki Hino, Hokkaido University

China and Japan collaborations have been rapidly progressed by the supports of JSPS and CAS. In particular, very aggressive collaborations have been conducted in the field of PWI and PFCs, Blanket, Tritium, Superconductor and Experiments in LHD, HT-7 and EAST. In addition, both counties have very actively investigated on fusion plasma and technologies toward next generation of fusion devices such as ITER, Helical Reactor and Tokamak Reactor. Thus, it is quite useful to conduct the C-J Symposium on PWI and Fusion Technology to exchange results of both countries and to enhance the R&D of both countries.

The present symposium has the topics on plasma wall interaction, plasma facing materials and components, core plasma behavior, blanket, tritium, superconductor, ITER related R&D and theory. The number of the presented papers was 39, and the participants were 45, 18 from Japan and 27 from China. Very aggressive discussions were conducted in this symposium, and the understanding for important issues toward to ITER and Demonstration Reactor was deepened.

We acknowledge to Ms. Xinfeng Luan, Secretary of this symposium, Mr. Kazuma Shimizu and Ms. Mayumi Kato, the NIFS CUP Officers, for their very excellent and kind supports for this symposium.

Keywords:

Plasma wall interaction, Plasma facing materials and components, Core plasma behavior, Blanket, Tritium, Superconductor, ITER, Demonstration reactor

Scope and Organization

Scope

China and Japan collaborations have been rapidly progressed by the supports of JSPS and CAS. In particular, very aggressive collaborations have been conducted in the field of PWI and PFMCs, Blanket, Tritium, Superconductor and Experiments in LHD, HT-7 and EAST. In addition, both counties have very actively investigated on fusion plasma and technologies toward next generation of fusion devices such as ITER, Helical Reactor and Tokamak Reactor.

It is very useful to conduct the C-J Symposium on PWI and Fusion Technology to exchange results of both countries and to enhance the R&D of both countries.

Topics

Workshop on Plasma wall interaction
Plasma facing materials and components
Core plasma behavior
Blanket
Tritium
Superconductor
ITER related R&D
Theory

Scientific Program Committee

Prof. Chen Junling (ASIPP) Chair
Prof. Luo Guanglan (ASIPP)
Prof. Wu Yu (ASIPP)
Prof. Song Yuntao (ASIPP)
Prof. Feng Kaiming (SWIP)
Prof. Liu Xiang (SWIP)
Prof. Guo Quangui (SICCCAS, Shanxi Institute of Coal Chemistry, Chinese

Academy of Sciences)
Prof. Fang Qianfeng (ISSP, Institute of Solid State Physics, Chinese Academy of Sciences)
Assoc. Prof. X.Z. Gong (ASIPP)
Assoc. Prof. J.S. Hu (ASIPP)

Prof. T. Hino (HokaidoUniversity) Co-chair
Assoc. Prof. N. Ashikawa (NIFS)
Prof. K.Okuno (Shizuoka University)
Prof. M. Matsuyama (Toyama University)
Prof. N. Yoshida (Kyushu University)

Local organizing Committee

Chen Junling (ASIPP, Chair)
Luan Xinfeng (ASIPP, Secretary)

Contents

Progress and Status of Chinese Helium-cooled solid breeder TBM

K.M. Feng[1)], C.H. Pan[1)], G.S. Zhang[1)], T. Yuan[1)], Z. Chen[1)], Z. Zhao[1)], H.B. Liu[1)], Z.Q. Li[1)], G. Hu[1)], X.Y. Wang[1)], X.F. Ye[1)], D.L. Luo[2)], C.M. Gao[4)], T.Y. LUO[2)], Y.J. Feng[1)], H.Y. Wang[2)], Y.J. Chen[1)], Z.W. Zhou[3)]， Z. X. Li[1)], G.Y. Zheng[1)]

[1)] *Southwestern Institute of Physics, Chengdu 610041, P.R.China*
[2)] *Institute of Engineering Physics, Chinese Academy of Science, P.R. China*
[3)] *Tstinghua University, Beijing 100084, P.R.China.*
[4)] *University of Electronic Science and Technology of China, Chengdu 610054, P.R. China*
Email: *fengkm@swip.ac.cn; Fax:+86-28-82850956*

Abstract

Testing TBM (Test Blanket Modules) is one of important engineering test objectives in ITER project. China is performing the TBM design and R&D based on Chinese development strategy of fusion DEMO. Ceramic breeder with helium-cooled test blanket module concept for testing on ITER will be one of the basic options in China. The current progress and status on design and R&D of CH HC-SB (Chinese Helium-cooled Solid Breeder) TBM are introduced briefly. The modified designs of HC-SB TBM and related ancillary sub-systems, test strategy on ITER, as well as relevant R&D activities are summarized.

1. Introduction

Testing TBM (Test Blanket Modules) is one of important engineering test objectives in ITER project. China is implementing the TBM design and R&D plan based on Chinese development strategy of fusion DEMO [1-2]. Ceramic breeder with helium-cooled test blanket module concept for testing during ITER operation period should be one of the basic options in China. Different design of HCSB TBM on module size, sub-module arrangement and modification and optimization of system have been carried out since 2004.

The current progress and status on design and R&D of CH HC-SB (Chinese Helium-cooled Solid Breeder) TBM are introduced. The modified designs of HC-SB TBM and related ancillary sub-systems, test plan on ITER, relevant R&D activities are summarized. An international and domestic collaboration plan on R&D and construction of related facilities of TBM are proposed.

Under the cooperation of domestic institutes, the preliminary design and performances analysis as well as an updated Design Description Document (DDD) have been carried out in 2007. Preliminary design and analysis have shown that the proposed TBM module concept is feasible within the existing technologies.

2. Design Description

A modified design of the HC-SB TBM based on 2×6 sub-modules arrangement, and 3-D global neutronics calculation have been completed [3]. The structure design outline of CH HC-SB module based on “half-port” size of ITER test port is described. The HCSB-TBM is located in vertical frame of the equatorial test port. Dimension of vertical frame is 1700mm in poloidal direction, 524mm in toroidal direction and 800mm in radial direction. Taking into account 20mm gap between TBM and frame, the dimension of HCSB-TBM is 1660mm height and 484mm width. Facing plasma side of HCSB-TBM is needed to be protected by beryllium layer of 2mm. the radial dimension of the HCSB-TBM is 670mm except for beryllium layer thickness. The HCSB-TBM consists of the following main components:

U-shaped first wall, caps, back-plate, grid, breeding sub-modules, and support plate. The detailed of HCSB-TBM illustrated in firgure1.

The Reduced-Activation Ferritic/Martensitic (RAFM) steel and the helium gas are used as structure material and coolants, respectively. To assure an adequate tritium breeding ratio (TBR), beryllium pebbles with diameters of 0.5-1mm and pebble-bed structure are adopted to as neutron multiplier; The lithium orthosilicate (Li_4SiO_4) with lithium of 80% enriched in ^6Li is used as tritium breeder. The pressure of the helium cooling system and the tritium extraction system are 8MPa and 0.1 MPa, respectively. The explosive view of HCSB TBM and the cross-section of sub-module are shown in Fig.1-2. Main parameters of the HCSB TBM design are shown in Table 1. Comparison with others TBM designs [4-5], Chinese solid TBM have obvious characteristics of simple structure, mature technical in domestic.

Table 1 Main parameters of the HCSB TBM design

Neutron surface loading, [MW/m^2]	0.78
Surface heat flux,[MW/m^2]	0.5
Total power (includes surface heat flux), [MW]	0.99
Tritium production ratio, [g/FPD]	0.0127
Tritium breeder	Lithium orthosilicate, Li_4SiO_4
Form	Ø=0.5-1mm, pebble bed
^6Li enrichment, [%]	80
Max. temperature, [℃]	693
Neutron multiplier	Beryllium
From	Binary, Ø=0.5-1mm, pebble bed
Max. temperature, [℃]	635
Coolant	(He)
Pressure, [MPa]	8
Temperature(inlet/outlet), [℃]	300/500
Pressure drop, [MPa]	0.3
Structure material	Ferritic steel, CFL-1
Max. temperature, [℃]	528

The tritium exaction system (TES), helium-cooling system (HCS), and the coolant purification system (CPS) have been designed as auxiliary systems. Main design parameters for the tritium extraction system (TES) follow that the composition of purge gas is He+ 0.1%H_2, pressure at the inlet of TBM blanket is 0.12 MPa, extracted amount of tritium is 0.1 g/d, helium mass flow is 0.65 g/s, and tritium extraction efficiency ≥95%.

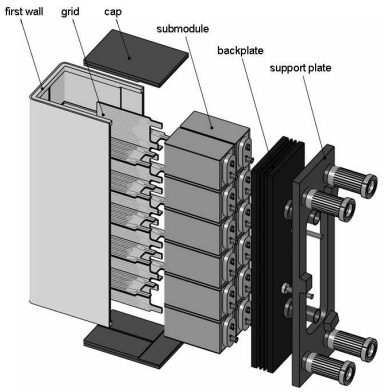

Fig.1 Explosive view of the HCSB-TBM

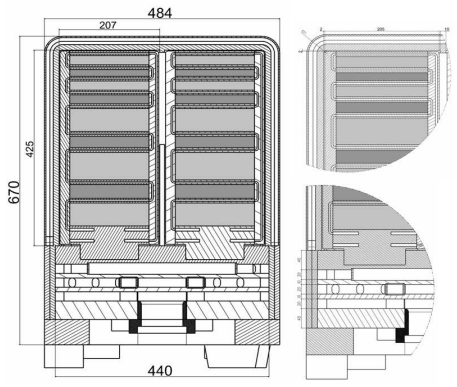

Fig.2 Cross-section of Sub-module

3. Performance Ansysis

3.1 Neutronics Analysis

Three-dimensional neutronics calculation based on the ITER-FEAT structure model using MCNP/4C [6] code and the data library FENDL2.0 [7] give the total energy deposition of 0.567MW, and a peak power density of 5.85 W/cm^3 under a neutron wall loading of 0.78 MW/m^2. The 3-D model of neutronics calculation is shown in Fig.3. The power density distribution in the radial zone is shown in Fig.4. The tritium generation amount is 0.0127g for a full power day (FPD). In order to improve the power density in the blanket module, the arrangement of the Be neutron multiplier in the breeding zone has been optimized. Binary Be pebbles with diameter 0.5 and 1 mm were are chosen.

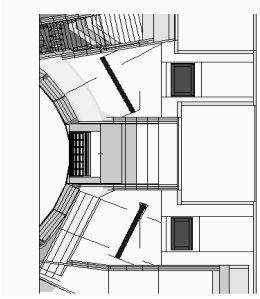

Fig.3 The MCNP model of neutronics calculation

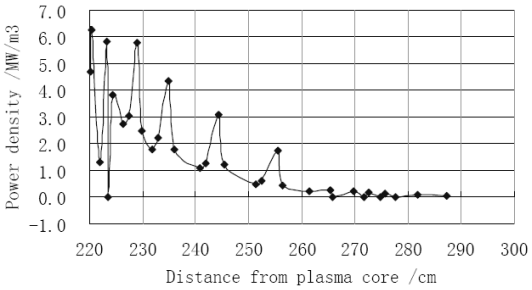

Fig.4 Power Density distribution in the radial zones

3.2 Thermal-hydraulics

For the CN HCSB TBM, the inlet and outlet temperature of the helium coolant is 300 ^{0}C and 500 ^{0}C, respectively. The serial connection scheme is adopted in the coolant flow loop of TBM, that is the coolant flows into the first wall, cap/grid, and the sub-module in series. The thermal-hydraulic analysis is performed using the ANSYS [8] and FLUENT codes. The results show that, under the extreme operative condition with a surface heat flux of 0.5MW/m^2, the peak temperature of TBM amounts to 693 ^{0}C which occurred in the second breeder zone of sub-module, and the peak temperature of different zones (listed in table 1) is in permissible range of different materials (700 ^{0}C for Be, 550 ^{0}C for ferritic steels and 900 ^{0}C for ceramic Li_4SiO_4). The temperature distribution of first wall, cap/grid, and sub-module are shown in Figs.5-8.

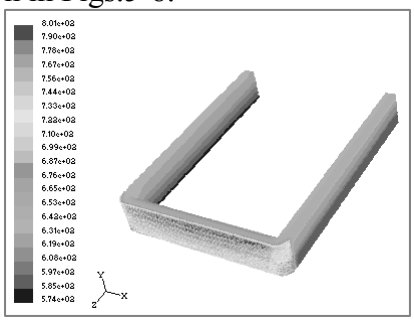

Fig.5 Temperature distribution of first wall

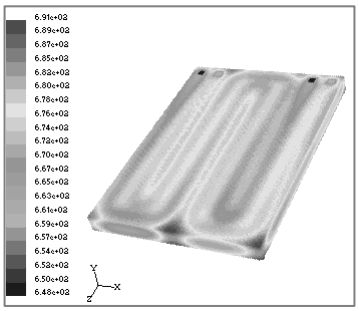

Fig.6 Temperature distribution of cap

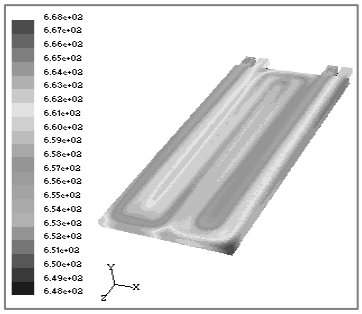

Fig.7 Temperature distribution of grid

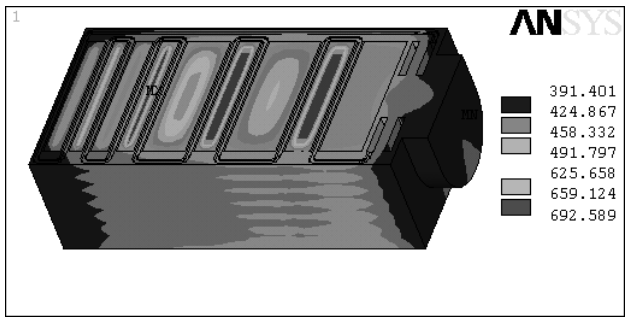

Fig.8 Temperature distribution of first wall

The pressure drop in the TBM is about 0.3MPa. The estimated pressure drop in the TBM external circuit is about 0.1MPa, assuming the total length is 100m, the inner diameter is 100mm, and includes 20 bends 90° for the hot and cold leg, respectively. So the total pressure drop in the TBM helium circuit system is about 0.4MPa and the needed pumping power is 100KW assuming the pump efficiency is 80%.

3.3 Radioactivity Calculation

Activation analysis has been performed assuming a continuous irradiation over 1 year at full fusion power (500 MW). Neutron fluxes are provided in46 energy groups by 3-D neutron transport code, MCNP for each specified material zone. Activation and dose calculations are performed by means of computation codes FDKR [9] and DOSE. The composition data of structure material in the module is from reference material, EUROFER97. Results shown that the total activation inventory is 7.86×10^{16} Bq at shutdown time and drops slowly thereafter and reaches an extremely low level value of 1.09×10^{13} Bq after 100 years. The dose rate is 3.34×10^{7}mSv/hr at shutdown time. Thereafter the dose rate declines rapidly and reach 2.62mSv/hr after 10 years. Considering ITER operation factor 0.22, after 10 years' cooling, the dose rate is enough to meet ALARA threshold.

3.3 Safety Analysis

Preliminary safety analyses including LOCA, LOFA and accident analysis based on FMEA method have been completed by using FDKR, RELAP5 and DOSE codes.

The thermal-hydraulic safety analysis has to testify that the TBM and its Helium Cooling System (HCS) will not impact the safe operation of ITER under normal and accidental conditions. In order to simulate the transient accidents, TBM and HCS are modeled using system code RELAP5/MOD3 [10]. The performance of the TBM and HCS during normal operation and accidents has been investigated [11-12]. Steady state and three postulated initiating events are considered, and these are In-Vessel LOCA, Ex-Vessel LOCA and In-Box LOCA.

The Ex-Vessel LOCA will induce the melting of first wall beryllium armor after about 80 seconds of the LOCA initiation and some controlling measures have to be taken before melting. The pressurization of Vacuum Vessel induced by In-Vessel LOCA is about 10kPa, and it's within the allowable value of ITER design 200kPa. The variety of the temperature in Ex-Vessel LOCA and the variety of the VV helium pressure in In-Vessel LOCA are shown in Figs.9-10, respectively. The In-Box accident would lead to pressurization of the TBM box including all pebble beds, and the pressure of purge gas pipes to the system pressure of 8MPa in about 2 seconds. So there must have a pressure relief for the blanket box, and at the same time the fast isolation of the TES from TBM has to be taken to keep the TES safety.

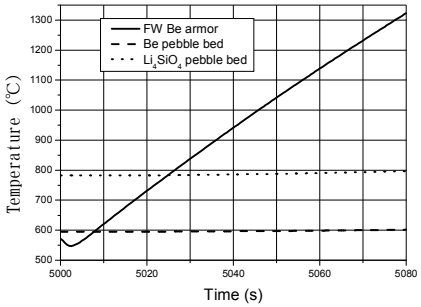

Fig. 9 Temperature in Ex-Vessel LOCA

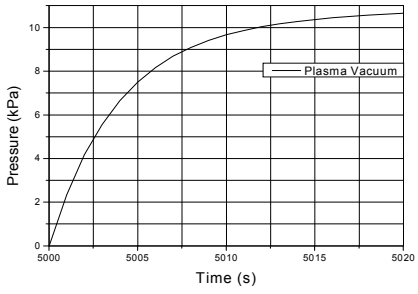

Fig.10 VV helium pressure in In-Vessel LOCA

4. R&D Progess

4.1 Heilium Test Loop

In order to validate TBM design, especially regarding mass flow and heat transition processes in narrow cooling channels, it is indispensable to test mock-ups in a helium loop under realistic pressure and temperature profiles [13]. According to TBM design parameters, requirements for the test section are summarized in table 3.

Table 3 Requirements for test sections

Test section	HE mass flow rate /kg^{-1}s	Pressure /MPa	Pressure difference at test section /MPa	He inlet/outlet temperature /℃	power supply /MW
TBM	0.13～1.3	8	<0.3	300/500	1
DEMO Blanket	～4	8	<0.4	300/500	5

The loop includes the primary helium heat transport loop and the secondary water loop. Main components of the primary loop are, besides the test module, a heat exchanger, circulator, electrical heater, dust filter, control valves and pipe work. The primary loop is directly connected to the helium purification subsystem via small pipes by taking a small bypass flow. Another interface to the pressure control unit is needed for system evacuation, helium supply and protection against overpressure. Thermal stress has been calculated by software CAESAR. Corrugated pipe is not used. If use it, the footprint will be smaller and the pipeline could be simpler.

The preliminary designs of the helium gas test loop with pressure 8-10MPa and temperature 550-600^{o}C have been completed [11-12]. The flow chart and layout diagram of the test loop are shown in Fig.11. The layout diagram of the test loop is shown in Fig.12.

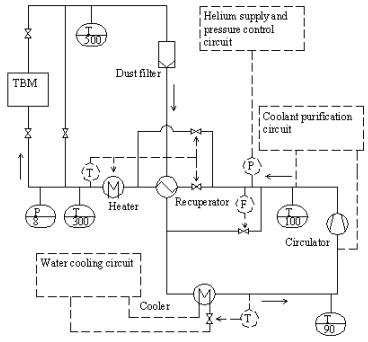

Fig.11 Flow chart of the test loop

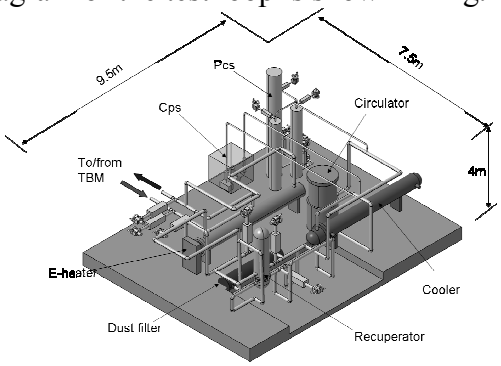

Fig.12 Layout diagram of the test loop

4.2 Ceramic Breeder

Investigation of two kinds of ceramic breeder, Li_2TiO_3 and Li_4SiO_4 on fabrication and performance test is undergoing in China. Relevant R&D on the key issues for the ceramic breeder, the tritium permeation barrier is also introduced. The study on experimental technologies relative to pebble bed has also been started. The primarily investigated the influence of pebble bed dimensions and filling factor on pebble bed properties. In order to study the heat transfer in the blanket, the experimental apparatus will be planed to design and measure the effective thermal conductivity of pebble beds. The foundational study on tritium behavior in solid breeder has been conducted with cooperation of the foreign universities. The sample of Li_4SiO_4 pebbles of diameter 1mm is shown in Fig.13.

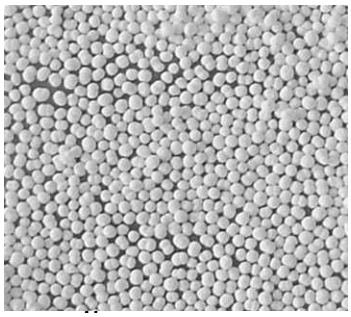

Fig.13 Li_4SiO_4 pebbles of diameter 1mm

4.3 Neutron Multiplier

The fabrication of beryllium pebbles has been investigated. Rotating Electrode Process (REP) developed by NGK co. in EU [14] and Japan Gas Atomization Method (GAM) developed by Brush Wellman co. in USA are considered as candidate fabrication processes of beryllium pebbles for CH HCSB TBM.

The study on experimental technologies relative to pebble bed has also been started. We primarily investigated the influence of pebble bed dimensions and filling factor on pebble bed properties. In order to study the heat transfer in the blanket, the experimental apparatus will plan to design and measure the effective thermal conductivity of pebble beds.

China has large yielding ability and relevant fabrication experiences of neutron multiplier (Be). Under the support of ITER Shielding Blanket Module (SBM) qualification task, development of Chinese VHP-Be is undergoing.

4.4 Structure Materials

Reduced Activation Ferritic/Martensitic (RAFM) steels are the reference structural materials for the in vessel components of DEMO. Also, this type of materials will be used in the test blanket modules (TBM) to be tested on ITER test port. Chinese Low-activated Ferritic/martensitic steel, CLF-1, is being developed. The CFL-1 steel is used as the primary candidate structural material for Chinese HCSB TBM design.

The structural materials for the first wall blanket must maintain their mechanical integrity and dimensional stability for adequate lifetimes under the severe radiation thermal, chemical and stress condition imposed in a fusion reactor environment. The candidate materials must be resistant to neutron radiation damage, capable to elevated temperature operation under stress, compatible with other blanket and plasma materials, compatible with the hydrogen plasma, and capable of withstanding high surface heat fluxes. The structural material must have adequate resources and be easily fabricated. In addition, the structural material should not produce high levels of long-lived radioactive products and that short-lived products should not produce unacceptable safety consequences. Some test results of CLF-1 are shown in Figs.14-15.

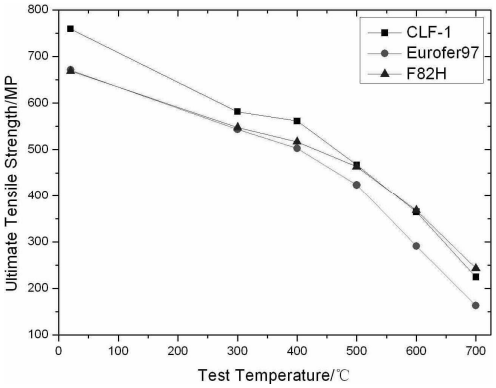

Fig.14 Tensile Strength of CLF-1

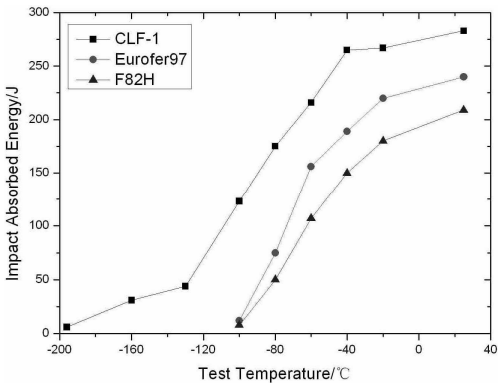

Fig.15 DBTT of CFL-1

5. Summary

A modification design and performance analysis of Chinese ITER HC-SB TBM has been completed. Preliminary design and performance analysis for the TBM module have been performed. The results show that the current design of HCSB TBM is feasible within the existing technologies. It is characterised by simple structure, mature technical in China. Updated design description document

(DDD) of HCSB TBM has been carried out in 2007. The further design works will update and optimize the structure design as well as ancillary subsystem parameters. The fabrication technology of components and ceramic breeder for HCSB TBM are being developed in China.

Acknowledgements

This work was partly supported by the JSPS-CAS Core University Program in the field of Plasma and Nuclear Fusion.

References

[1] K.M. Feng, P.C Pan, G.S. Zhang, T. Yuan, Z. Chen, et al., Overview of design and R&D of solid breeder TBM in China, Presented at 8th International Symposium on Fusion Nuclear Technology (ISFNT-8), Heidelberg, Germany, , Sept.30-Oct.5, 2006.

[2] K.M. Feng, C.H. Pan, G.S. Zhang, D.L. Luo, Z.W. Zhou, et al., Preliminary design for a China ITER test blanket module, J. of Fusion Engineering and Design, 81(2006)1219-1224.

[3] PAN Chuanhong. Definition of DEMO reactor and DEMO development strategy in CH[R] Test Blanket Working Group Meeting (TBWG-12) Naka, Japan Mach 10-11, 2004.

[4] G. S. Hatalov, I. Kirillov, et al., Russian DEMO-S reactor with continues plasma burn [J] .Fusion Engineering and Design 51-52 (2000) 289-298.

[5] S. Nishio, T. Ando, et al., Engineering aspects of a steady state tokamak reactor [J] .Fusion Engineering and Design 15 (1991) 121-135.

[6] J. F. Briesmeister (ed.): MCNP - A General Monte Carlo N-Particle Transport Code, Version 4C, LA-13709-M, April 2000.

[7] H. Wienke and M. Herman, FENDL/MG-2.0 and FENDL/MC-2.0, The processed cross-section libraries for neutron-photon transport calculations, version 1, March 1997, IAEA Vienna, Report IAEA-NDS-176, Rev. 1, October 1998.

[8] ANSYS Technical Report, Rev. 5.1, IMAG Industries Co., February, 1995.

[9] Y.X.Yang, K.M.Feng and J.H.Huang, CCC-541/FDKR, Radiation Shielding Information Center, Oak Ridge National Laboratory, 1989.

[10] The RELAP5 Code Development Team: RELAP5/MOD3 Code Manual Volume I: Code Structure, System Models, and Solution Methods, NUREG/CR-5535, INEL-95/0174, Aug. 1995.

[11] Boccaccini L.V., Design Description Document for the European Helium Cooled Pebble Bed (HCPB) Test Blanket Modules, Forschungszentrum Karlsruhe, December, 2005.

[12] Jin Xuezhou, R.Meyder, Thermal-Hydraulic System Study of the Helium Cooled Pebble Bed (HCPB) Test Blanket Module (TBM) for ITER Using System Code RELAP5, Chinese Plasma Science and Technology, Vol.2 2005.

[13] Ionescu Bujor, M, et al., Helium Loop Karlsruhe (HELOKA) – large experimental facility for the in-vessel ITER and DEMO components, 20th IAEA fusion energy conference, 2005.

[14] K.M. Feng, G.S. Zhang, Z Chen, T, Yuan, Z Zhou, et al., Design Description Document for the Chinese Helium- cooled Solid Breeder (CH HCSB) TBM, (Draft Design Report), 2007.

Elucidation of retention behavior of hydrogen isotope during formation of tungsten-carbon mixture layer

Kenji Okuno[1], Yasuhisa Oya[1], Yohei Kikuchi[1], Yuji Inagaki[1], Guangnan Luo[2], Naoko Ashikawa[3], Naoaki Yoshida[4], and Akio Sagara[3]

[1]Radioscience Research Laboratory Faculty of Science, Shizuoka University, 836 Ohya, Suruga-ku, Shizuoka 422-8529, Japan

[2] ASIPP, China,

[3] National Institute for Fusion Science, Japan

[4] Kyushu University, Japan

E-mail of corresponding author: srkokun@ipc.shizuoka.ac.jp

Abstract

To elucidate C^+ implantation effects on deuterium retention in tungsten, simultaneous C^+ and D_2^+ implantations were performed on tungsten. It was found that the deuterium retention for the simultaneous implanted tungsten was lower than that for the sequential one, indicating that sputtering of carbon and deuterium trapped by carbon would prevent from deuterium trapping. In addition, the deuterium retention was decreased as the ion flux ratio of C^+/D^+ increasing and no deuterium trapping by carbon were observed for high C^+/D^+ ratio. These facts indicated that for lower ion flux ratio, D trapping by formation of C-D bond would govern mainly D retention, and for higher ones, on the other hand, damages of W produced by the simultaneous ion implantation.

Keywords: Tungsten, Deuterium inventory, Impurity, Desorption, Carbide

1. Introduction

Plasma facing materials are one of key boundary to keep high purity D-T plasma and their selections are quite important. In recently, the combination of several materials for the plasma facing materials including first wall, divertor and baffles is thought to be one of the best solutions [1-3]. The tungsten-carbon system is widely studied recently [3-9]. There are lots of reports related to the formation of carbon layer and carbide by the implantation of carbon ions and the data of as-received pristine materials are usually used for design activities and some data may be quite different from the actual results in fusion conditions. These reports are based on the results of the carbon ion pre-implanted tungsten and the mixed layers have been formed before the deuterium implantation. However, in the case of fusion environment, simultaneous implantations of carbon and deuterium ions were dynamically occurred and continuous deuterium and carbon recycling will proceed. These facts motivate us to perform the simultaneous implantations of carbon and

deuterium ions to understand a more realistic deuterium trapping mechanism in tungsten and find out the role of carbon on the deuterium retention during the simultaneous ion implantation.

2. Experiments

C^+ and D_2^+ simultaneous implantation system established in Shizuoka University was illustrated in Fig. 1. The disk-type samples with 10 mm diameter and 0.5 mm thickness were prepared from a rod of tungsten under stress-relieved conditions supplied by Allied Tungsten Co. Ltd. The samples were polished mechanically and pre-heated at 1173 K for 10 minutes in vacuum to remove the surface impurities and damages induced by the polishing process. At first, to evaluate the implantation sequence effect, two different implantation procedures, namely sequential implantation and simultaneous implantation, were performed. In the sequential implantation, the 10 keV C^+ implantation was performed with the ion flux of 1.0×10^{18} C^+ m^{-2} s^{-1} up to the fluence of 1.0×10^{22} D^+ m^{-2}. Thereafter the 3 keV D_2^+ implantation was done with the same ion flux and fluence with C^+ implantation. For the evaluate the flux dependence of C^+ to D^+, the ion flux of C^+ was changed from 2.0×10^{17} C^+ m^{-2} s^{-1} to 2.0×10^{18} C^+ m^{-2} s^{-1} and the ion flux and fluence of D_2^+ were fixed to be 1.0×10^{18} D^+ m^{-2} s^{-1} and 1.0×10^{22} D^+ m^{-2}. Therefore, the flux ratio of C^+/D^+ was changed from 0.2 to 2. After the implantation, the chemical states of W and C were evaluated by XPS (ESCA1600 system, ULVAC-PHI Inc.) using Mg-kα X-ray source (1253.6 eV) and a hemispherical electron analyzer [8, 9]. To evaluate the D desorption behavior and retention, the TDS experiment was performed at a heating rate of 0.5 K s^{-1} and at heating temperatures up to 1173 K and desorbed molecules were measured by a quadruple mass spectrometer.

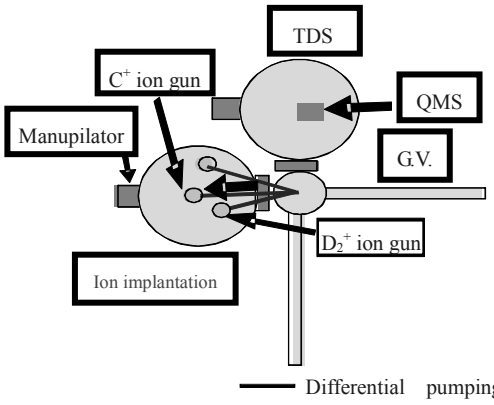

Fig. 1 C^+ and D_2^+ simultaneous implantation system

3. Results

Figure 2 (a) summarizes the D_2 TDS spectra for the sequential implanted tungsten and simultaneous implanted one. The D_2 TDS spectra for pure tungsten and WC were also shown. It was found that the deuterium desorption at higher temperature was only found for the sequential implanted tungsten. This high desorption temperature was almost the same as that for WC,

indicating that the deuterium desorption trapped by carbon. In the case of simultaneous implanted tungsten, the shape of TDS spectra was almost the same as that for pure tungsten. To evaluate the chemical state of carbon implanted into tungsten, XPS analyses were performed. The C-1s XPS spectra were found to be divided into two peaks; C-W bond and C-C bond. The peak areas for these peaks were summarized in Fig. 2 (b). It was clear that the major chemical state for the only C^+ implanted tungsten was C-C bond. However, in the case of sequential implanted tungsten, the amount of C-C bond was clearly decreased, indicating that the C-C bond was chemically sputtered by D_2^+ implantation.

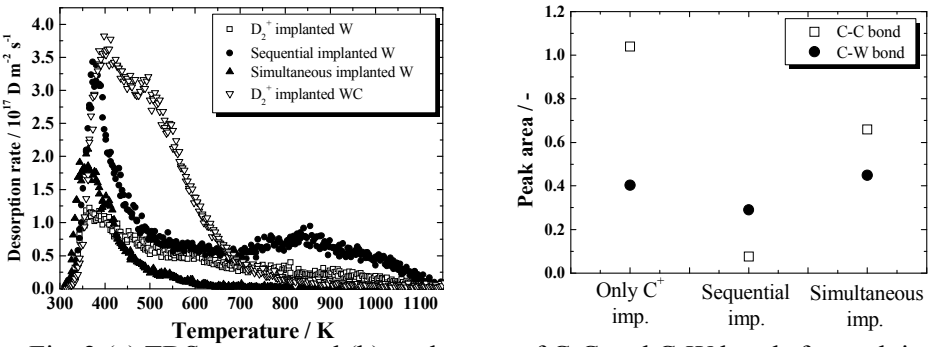

Fig. 2 (a) TDS spectra and (b) peak areas of C-C and C-W bonds for each implantation.

For the simultaneous implanted tungsten, not only C-W bond but also C-C bond were existed. However, the amount of C-W bond was almost constant among these samples, indicating that the formation of C-W bond was almost saturated among these samples and the carbon with forming C-C bond was accumulated near the surface region of the tungsten sample.

Figure 3 shows the D_2 TDS spectra for the simultaneous implantation tungsten. In the case of C^+/D^+=0.2, the TDS spectrum was clearly different from the other spectra, especially in the higher temperature region. The desorption stages were extended to higher temperature side and the large desorption was found at around 800 K, which is almost the same as that for the sequential implantation tungsten. For the C^+/D^+=1 and 2, the higher desorption stage at around 800 K was disappeared and only one large desorption peak was found at lower temperature.

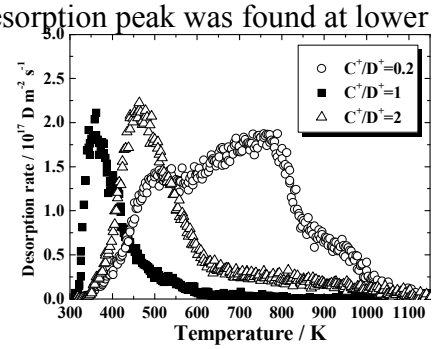

Fig. 3 The D_2 TDS spectra for the simultaneous implanted tungsten with various C^+/D^+ flux ratio.

From these experimental results, C^+ implantation effect on deuterium trapping in tungsten is

discussed. Large amounts of carbon would form C-C bonds, which was easily sputtered by succeeding D_2^+ implantation in case of sequential implantation. Therefore some of deuterium would be bound to carbon with forming C-D bond in tungsten, which contribute to the higher temperature desorption stage of TDS. In the case of simultaneous implantation, the C-C bonds were still remained in tungsten and simultaneous deuterium trapping with carbon in tungsten would not enhance the deuterium retention, indicating that the sputtering of carbon and deuterium trapped by carbon would prevent the enhancement of deuterium trapping in simultaneous implanted tungsten. In addition, the flux ratio of C^+/D^+ would be one of key factor for deuterium retention in tungsten. In the low C^+/D^+ ratio, the deuterium retention evaluated by TDS was highest and deuterium trapping by carbon would be a major trapping state compared to deuterium trapping by available traps. This fact indicated that the tungsten sputtering by carbon would be low, and simultaneous carbon and deuterium would be occurred in tungsten.

4. Conclusion

To elucidate C^+ implantation effects on deuterium retention in tungsten, simultaneous C^+ and D_2^+ implantations were performed on tungsten. It was found that the deuterium retention for the simultaneous implanted tungsten was lower than that for the sequential one, indicating that sputtering of carbon and deuterium trapped by carbon would prevent from deuterium trapping. In addition, the deuterium retention was decreased as the ion flux ratio of C^+/D^+ increasing and no deuterium trapping by carbon were observed for high C^+/D^+ ratio. These facts indicated that for lower ion flux ratio, D trapping by formation of C-D bond would govern mainly D retention, and for higher ones, on the other hand, damages of W produced by the simultaneous ion implantation.

Acknowledgements

This study has been supported by NIFS collaboration program of No. NIFS07KOBA020, JSPS Kakenhi No. 19686055 and 19055002 from MEXT, Japan, and the Center for Instrumental Analysis at Shizuoka University. This work was partly supported by the JSPS-CAS Core University Program in the field of Plasma and Nuclear Fusion.

References

[1] M. Kaufmann, and R. Neu, Fusion Eng. Des. **82** (2007) 521-527.
[2] J. Pamela et al., J. Nucl. Mater. **363-365** (2007) 1-11.
[3] R.P. Doerner, **363-365** (2007) 32-40.
[4] Ch. Linsmeier et al., J. Nucl. Mater. **290-293** (2001) 25-32.
[5] V. Kh. Alimov, Phys. Scr. **T108** (2004) 46-56.
[6] O. V. Ogorodnikova et al., J. Nucl. Mater. **313-316** (2003) 469-477.

[7] R.A. Anderl et al., J. Nucl. Mater. **290-293** (2001) 38-41.
[8] H. Kimura et al., Fusion Eng. Des. **81** (2006) 295-299.
[9] E. Igarashi et al., J. Nucl. Mater. **363-365** (2007) 910-914.

Recent Progress of Plasma Facing Material Research at SWIP

X. Liu[1], J.M. Chen[1], J.H. Wu[1], Z.H. Wang[2] and L. Wang[2]
1 Southwestern Institute of Physics, P.O. Box 432, Chengdu 610041, Sichuan, China
2 Ningxia Orient Non-ferrous Metals Group Co. Ltd, Shizuishan City, Ningxia, China
E-mail of corresponding author: xliu@swip.ac.cn

Abstract

Vacuum sprayed tungsten coating and vacuum hot press beryllium as plasma facing materials were being studied at Southwestern Institute of Physics (SWIP) recently several years according to the domestic fusion research and development program and ITER-China fabrication tasks. The former will be tested as the armor materials of limiters in the HL-2A tokamak, and might be also tested in the modified tokamak machine HL-2M. The latter will be used for ITER-FW mock-ups if it satisfied the requirements of ITER qualification tests. In this paper the progress of VPS-W coating and VHP-Be will be reviewed.

Keywords: Plasma facing materials, Tungsten coating, Vacuum hot press beryllium, HL-2A, ITER-FW mock-ups

1. Introduction

Carbon, tungsten and beryllium are the major plasma facing materials in the present fusion experiment devices. Carbon materials, such as graphite and C/C composites, were commonly used in the previous and the present fusion devices. Tungsten as plasma facing materials was tested in many tokamak machines, such as TEXTOR and ASDEX Upgrade. ASDEX upgrade was the only fusion experiment device in which tungsten was adopted as the whole armor materials of the first wall. Beryllium with very low Z value and good compatibility with fusion plasma was selected as the plasma facing materials of ITER-FW mock-ups.

Recently years tungsten coated graphite and copper have been developed in China and commonly a interface layer as diffusion barrier was used for tungsten coated graphite and gradient interface for tungsten coated copper. Tungsten coated graphite with multilayered Si and W interface pre-deposited by physical vapor deposition (PVD) has been developed by cooperation with Shanghai Institute of Ceramics, Chinese Academy of Science. Up to now the fabrication processes have been optimized and basic physical properties and high heat flux performances were measured. Next step we will use this fabrication technology to coat the limiter tiles of HL-2A tokamak machine and test the tungsten armor in the next operation campaign.

As we known, S-65C beryllium fabricated by Brush Wellman Company (USA) has been selected

as the armor materials of ITER-FW mock-ups. China, as one of the participate members of ITER, will share the fabrication tasks of ITER-FW mock-ups. Therefore, ITER grade beryllium was being developed by cooperation with raw material supplier and beryllium block production companies in China. Up to now one kind of VHP beryllium (CN-G01) has been successfully developed, although its fundamental thermo-mechanical properties are very close to the requirements of ITER grade beryllium, however its thermal shock resistance capabilities are not satisfied. Therefore, a modification of beryllium fabrication processes has to be carried out. In this paper, the main progress and results of tungsten and beryllium researches will be reported.

2. Experiments and Results

2.1 Tungsten

Tungsten coated graphite was made by cooperation with Shanghai Institute of Ceramics, Chinese Academy of Science, multilayered Si, W interface with thickness of about 2 μm pre-deposited by physical vapor deposition (PVD) was used for the carbon diffusion barrier to restrain brittle tungsten carbide formation. Fig.1 is the cross-section photo of tungsten coated graphite. The porosity of tungsten coating is about 6 % and thermal conductivity is 89 w/m.k at room temperature. Thermal fatigue test indicated that it can endure 1000 cycles under a heat flux of 4.8 MW/m^2 without visible damages [1].

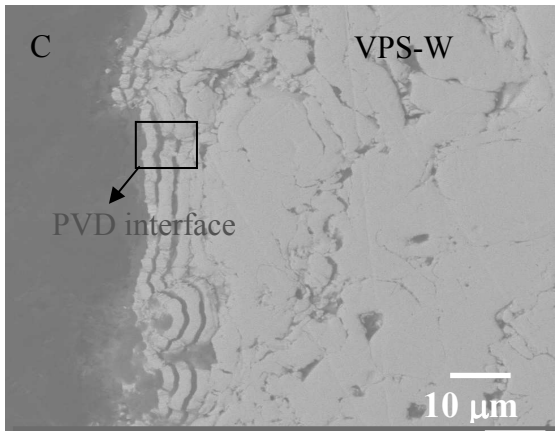

Fig. 1 Cross-section of VPS-W/C coating

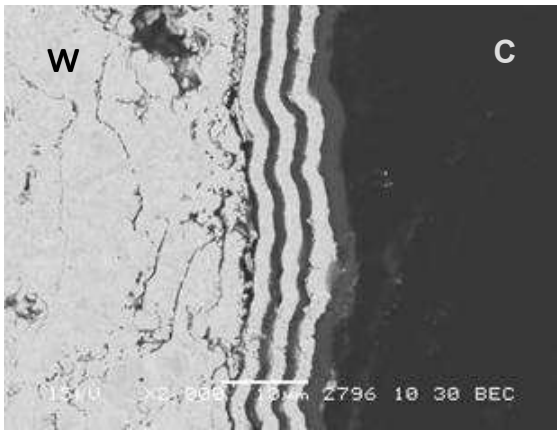

Fig. 2 Image after annealing at 1200 °C for 2h.

In order to investigate the microstructure evolution of W/C coating, in particular the multilayer interface, an annealing experiment was performed in Kyushu University. The annealing temperature is 800°C, 900°C, 1000°C, 1100°C and 1200°C, respectively, and the incubation time is 2 hours for every annealing temperature. After those annealing processes, the interface keeps a good integrality without cracking or failure appearance. Fig.2 shows the interface structure of VPS-W/C coating after annealing at 1200 °C for 2 hours, and no tungsten carbides are detected in the interface region.

Based on the coating technology, tungsten coating of limiter tiles of HL-2A will be prepared and will be tested in HL-2A next campaign.

2.2 Beryllium

ITER grade beryllium study began at the year of 2003, one kind of VHP beryllium had been successfully developed by the middle of last year. The content of beryllium oxides is slightly less than 1 %, and total elongation rate is in the rang of 2.5-2.7 at room temperature, which is very close to the requirements of ITER grade beryllium, but different to S-65C beryllium by a magnitude of about 10 %. Other thermo-mechanical properties, such as tensile strength, thermal conductivity, thermal expansion coefficient etc, basically satisfied the requirements of ITER grade beryllium. A report titled of characterization of Chinese beryllium CN-G01 has been submitted to ITER-IO (International Organization) [2]. A pre-evaluation test of CN-G01 beryllium has been performed at an electron beam facility JUDITH-1 at FZJ, Germany. The results indicated that cracking was its main damage mechanisms [3]. Since the acceptance criteria of other candidate materials must be of the comparative performance with S-65C beryllium. Therefore, the present fabrication technology for CN-G01 beryllium has to be modified.

Up to now, two important modifications are being done, one is to reduce the oxygen content of beryllium, the other is to increase the elongation rate. Firstly, the content of oxygen could be the key factor to determine the physical and HHF performances of beryllium since most of oxygen in beryllium existed in the form of BeO and it commonly distributed at the grain boundary, thus inducing the degradation of thermal conductivity and the decrease of bonding strength among grains, eventually negatively influencing the HHF performance. Secondly, increasing the elongation rate of beryllium will improve the plasticity, thus restraining the crack formation and extension. If we only look at the vacuum hot pressing process, two modifications could be adopted, one is increasing the temperature of vacuum hot press and another is promoting the vacuum degree of VHP chamber. Now a modified beryllium (CN-G01m) has been prepared after the efforts, its chemical composition was concluded in table 1, the relevant data of CN-G01 beryllium and S-65C beryllium were also listed in this table for comparison.

Table 1 Composition of Chinese VHP beryllium

Material type	Beryllium assay	Beryllium oxide	C	Fe	Al	Mg	Si	Other metals
CN-G01	>99 %	0.9-1 %	0.06 %	0.06 %	0.006 %	0.005 %	0.01 %	<0.04 %
CN-G01m	>99 %	~0.7 %	0.05 %	0.06 %	0.006 %	0.005 %	0.01 %	<0.04 %
S-65C	99.4 %	0.6 %	0.01 %	0.08 %	0.04 %	<0.01 %	0.03 %	<0.04 %

The physical and mechanical properties of beryllium were measured, for example, thermal

conductivity was measured by means of laser flash, tensile strength and total elongation rate in the

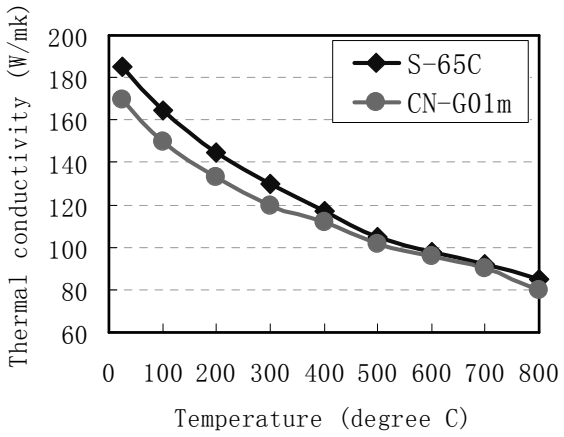

Fig. 3 Thermal conductivity of CN-G01m VHP beryllium

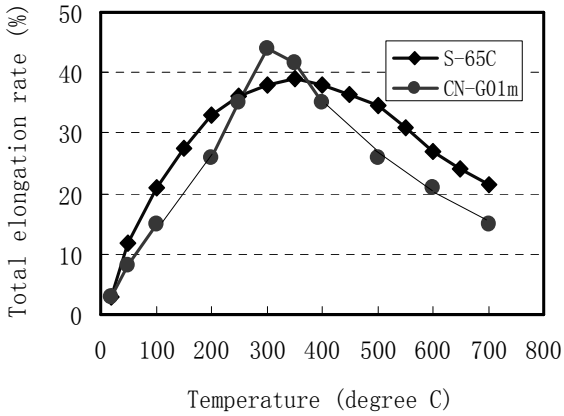

Fig. 4 Total elongation rate of CN-G01 VHP beryllium

range of room temperature to 800 °C were measured. Fig. 3 and 4 showed the thermal conductivity and total elongation rate of CN-G01 beryllium, the corresponding data of S-65C beryllium were showed in the figures for comparison. From figure 3 and figure 4, one can see that the newly developed VHP beryllium CN-G01m is very close to S-65C beryllium in the two key thermo-mechanical properties, only the elongation rate at the high temperature has some difference with S-65C beryllium. However, the difference might be less influence on the cracking behaviors since the high temperature plasticity of beryllium was relatively good and permitted larger margin to resist the thermal stresses during thermal shock. We think the low elongation rate of previous Chinese beryllium CN-G01 could be the main reason of poor thermal shock resistance capabilities. The newly developed beryllium samples will be tested in JUDITH-1 very soon, it is expectable that the new beryllium has better high heat flux performances.

3. Summary

Recently years, tungsten coating and beryllium as plasma facing materials were studied in our institute, respectively for the requirements of HL-2A tokamak operation program and ITER-China task agreements. A kind of VPS-W/C coating with multilayered Si, W interface pre-deposited by PVD will be tested as limiters in HL-2A tokamak machine for the first step, then it may be tested in the modified HL-2A in the future. For beryllium study, a newly VHP beryllium CN-G01m has been evaluated in the view point of physical/mechanical properties, it shows better elongation rate and lower BeO contents than the previous beryllium grade. Its HHF performance will be evaluated very soon and a better HHF performance is expected.

Acknowledgements

This work was partly supported by the JSPS-CAS Core University Program in the field of Plasma and Nuclear Fusion.

References

[1] X. Liu, et al, J. Nucl. Mater., **363-365** (2007) 1299-1303.

[2] Z.H. Wang et al, Characterization of CN VHP-Be , ITER_D_28M3L5 v1.0.

[3] X. Liu, et al, 9th China-Iapan Symposium on Materials for Advanced Energy System and Fission & Fusion Engineering Jointed with CAS-JSPS Core-university Program Seminar on Fusion Materials, System and Design Intergration, Oct. 23-26, 2007, Guilin, China.

Tritium Distribution in Surface Layers of Metallic Materials

M. Matsuyama[1)*], Z. Chen[2)], K. Nisimura[3)], S. Akamaru[1)], Y. Torikai[1)], Y. Hatano[1)]
N. Ashikawa[3)], Y. Oya[4)], K. Okuno[4)], and T. Hino[5)]

1) Hydrogen Isotope Research Center, University of Toyama, Toyama 930-8555, Japan
2) The Southwestern Institute of Physics, Chengdu 610041, Sichuan, China
3) National Institute for Fusion Science, Toki 509-5292, Japan
4) Radiochemistry Research Laboratory, Shizuoka University, Shizuoka 422-8529, Japan
5) Laboratory of Plasma Physics and Engi., Hokkaido University, Sapporo 060-8628 Japan
E-mail of corresponding author: masao@ctg.u-toyama.ac.jp

Abstract

Surface of the as-received samples cut off from the used SS316L plate in LHD was covered with depositions, which mainly consisted of carbon along with a small amount of titanium. Large retention of tritium was observed for the depositions. On the other hand, it was found that considerably high tritium retention in surface layers was brought about in Cu-Be alloy as well as SS316L in spite of tritium concentration in the bulk being very low and almost constant.

Keywords: tritium distribution, surface enrichment, stainless steel, Cu-Be alloy

1. Introduction

Basic data such as trapping and release rate of tritium as well as solubility, diffusion, permeation constants in various materials will play an important role for evaluation of tritium behavior in the fusion reactor materials. Especially, it is of a great importance to clarify behavior of the amount and/or distribution of tritium in surface layers of materials from view points of precise control of fuel particles, reduction of tritium inventory in materials, and safe waste management of materials contaminated with tritium.

When stainless steel type 316 (SS316) was exposed to tritium gas at a given temperature, it has been recently reported by Torikai et al. [1] that quite large enrichment of tritium in surface layers of the samples was caused. Difference in tritium concentration between surface and bulk was larger than a few 100 times although it depends on the exposure conditions of tritium to materials. It was considered that the trapping of tritium by metallic oxides such as chromium and iron oxides on the surface of SS316 was a main cause of the surface enrichment. Surface enrichment of tritium in the surface layers is also severe problem for development of tritium handling devices.

From this view point, in this study, the amount and/or distribution of tritium in surface layers of stainless steel type 316L (SS316L) used as protection plates in LHD and a commercial Cu-Be alloy have been examined in detail.

2. Experimental

Small plates of SS316L and Cu-Be alloy were exposed to molecular tritium at elevated temperatures. The former sample had been exposed to various plasmas so far. Two kinds of samples were obtained from the protection plate: namely, (1) one surface was the plasma-exposed surface and the rear surface was mechanically polished with a buff, which is denoted as the "as-received", and (2) both surfaces were polished with a buff. Examination of roughness effect of a sample surface on tritium retention was carried out by polishing one surface of the second samples with emery papers from #1500 to #320. On the other hand, both surfaces of Cu-Be alloy samples were finally polished with a buff. Composition of Be in Cu-Be alloy was 2 mass%. An original alloying plate of Cu-Be was delivered from Furuuchi Chemical Co. Size of the samples of SS316L and Cu-Be alloy was 10x10x0.5 mm^3.

As a first step, a SS316L sample was exposed to tritium gas diluted with deuterium (tritium concentration: 0.6 %) under the given conditions of temperature, pressure and time. Prior to the tritium exposure, all of the samples were stepwise heated in vacuum in a tritium exposure device from room temperature to the maximum temperature of 623K. The tritium was exposed after cooling down and then exposed to tritium gas of 1.3 kPa at a given temperature. After the exposure, the tritium amount retained in surface layers of the sample was evaluated by β-ray-induced X-ray spectrometry (BIXS), and the distribution of tritium concentration in the bulk of a Cu-Be alloy sample was evaluated by a chemical etching method used an aqueous solution of nitric acid.

3. Results and discussion

3.1. Observation of the surface of a SS316L sample

The plasma-exposed surface of an as-received sample and the surface after immersing into an aqueous solution of acid were observed by a scanning electron microscope (SEM). Depositions were fixed on the surface exposed to plasma particles. In addition to this, it was seen the original surface of a sample was rather rough, and the roughness was larger than 5 μm. To examine what elements are deposited on the surface of the as-received sample, cross-section of the sample was observed in detail, and elemental analysis of the depositions of which location was illustrated by a circle in the photograph was also conducted by an energy dispersion X-ray spectrometry (EDX). The results were shown in Fig. 1.

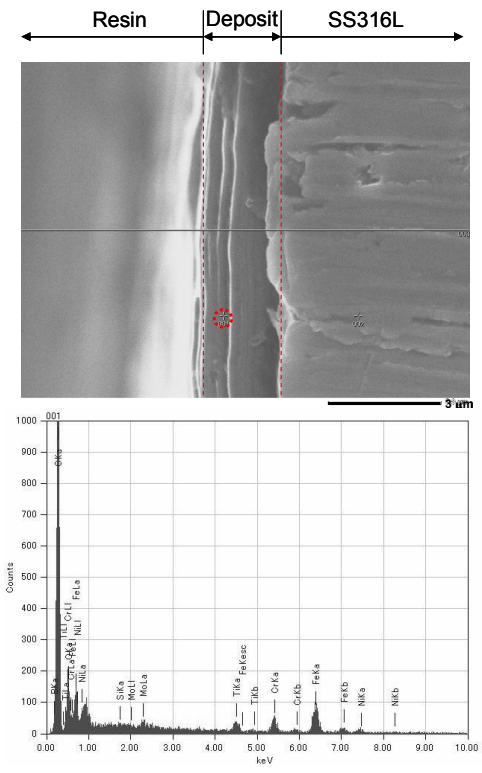

Fig. 1 Observation and analyses of cross-section by SEM and EDX.

Thickness of the depositions was about 2 μm, and a major element in the depositions was carbon. As can be seen from the photograph, the depositions piled up on the surface of SS316L. The EDX analyses described exist of a small amount of titanium along with carbon in the depositions as shown in the result of EDX analyses. Existence of titanium on the surface of the as-received sample was also confirmed by BIXS. It is considered that mixing of titanium is due to usage of a titanium sublimation pump.

3.2. Evaluation of the ad- and absorbed amount of tritium by BIXS

Effects of surface roughness of the SS316L sample on the amount of tritium adsorbed on the surface and the amount of tritium absorbed in surface layers were examined by means of BIXS. As a result, the ratio (R) of a surface-polished-sample with an emery paper to that with a buff was in the range from 1.1 to 1.8 except for the as-received sample (R=5.7). It was suggested, therefore, that roughness of the surface of a sample does not significantly affect the evaluation of tritium amount by BIXS.

Figure 2 show the comparison of X-ray spectra for SS316L and Cu-Be alloy samples. Surfaces of both samples were finally polished with a buff and the simultaneous exposure to tritium gas under the same conditions was employed. Although almost same intensity of Ar(Kα) peak was observed for both samples, a large difference in intensity of bremsstrahlung X-rays was observed. This indicates that the amount of tritium dissolved into the bulk of each sample is largely different. This agrees with the reported data about the solubility of hydrogen in both samples.

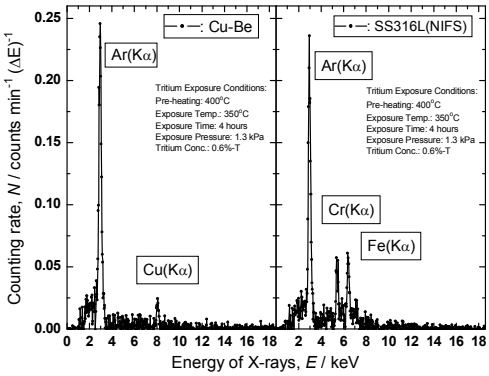

Fig. 2 Comparison of X-ray spectra between Cu-Be alloy and SS316L samples.

3.3. Depth profile of tritium in the surface layers

Large retention of tritium in the surface layers of SS316L and Cu-Be alloy samples was observed irrespective of the samples, indicating that a part of the exposed tritium is strongly fixed by oxygen atoms in the surface layers. Especially, a great amount of tritium was trapped on the surface of the as-received SS316L sample in which depositions such as carbon and titanium were observed. From this viewpoint, tritium depth profiles of these samples were examined by a chemical etching method. The result for a SS316L sample is elsewhere [2]. In this paper, depth profile of tritium in a Cu-Be

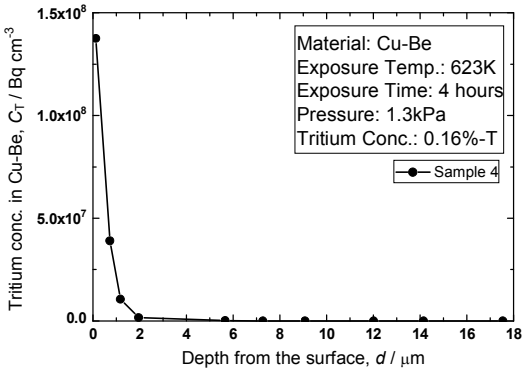

Fig. 3 Tritium depth profile in surface layers of a Cu-Be alloy sample.

alloy sample only will be presented. The results are shown in Figs. 3 and 4.

Figure 3 shows the result for surface layers within 18 μm from the surface. It was found that tritium concentration in thinner layers than 1 μm was very higher than that in deep region. When only a few μm of surface layers was removed by chemical etching, anomalously high concentration of tritium disappeared. This is similar behavior to a SS316L sample. On the other hand, Fig. 4 shows the tritium concentration in the bulk. Although tritium concentration in the bulk is very low, it was almost uniform. Tritium concentration in Cu-Be alloy was about 200 times lower than that in SS316L. This great difference may be basically due to the difference in solubility of tritium.

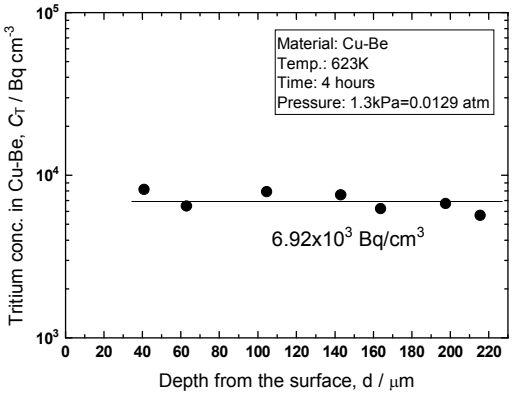

Fig. 4 Tritium depth profile in the bulk of a Cu-Be alloy sample.

4. Summary

Basic data such as solubility, diffusion coefficient, permeation constant and trapping and release rate of tritium play an important role for evaluation of tritium behavior in the fusion reactor materials. From this view point, the present study was examined concerning the amount and/or distribution of tritium retained in surface layers of stainless steel type 316L (SS316L) used as the protection plates in LHD and a commercial Cu-Be alloy.

Surface of the as-received samples cut from the SS316L plate was covered with depositions and a large amount of tritium was retained in the depositions. In addition, it was found that the surface enrichment of tritium can be also caused for a Cu-Be alloy sample, although the bulk concentration was very low and it was kept almost constant.

Acknowledgements

Present study was partly supported by the NIFS LHD Project Research Collaboration (NIFS07KOBS009), the Grant-in-Aid for Scientific Research of the Ministry of Education, Culture Sports, Science and Technology, and the JSPS-CAS Core University Program in the field of "Plasma and Nuclear Fusion".

References

[1] Y. Torikai et al., "Tritium uptake by SS316 and its decontamination", *J. Nucl. Mater.*, **329-333** (2004) 1624-1628.

[2] Y. Torikai et al., "Migration and release behavior of tritium in SS316 at ambient temperature", *J. Nucl. Mater.*, **363-365** (2007) 462-466.

Vacuum and wall conditioning system on EAST in the Exp' 2008

J.S. Hu, X.M. Wang, Y. Chen, J. H. Li, J.H. Wu, H.Y. Wang, D.W. Yang, N.C. Luo, S.F. Li, G.Y. Li, L. Wang, Q.S. Hu, L.M.Bao, Y.P. Zhao, J.G. Li and EAST vacuum group

Institute of Plasma Physics, Chinese Academy of Sciences, P.R. China
Hujs @ipp.ac.cn

Abstract. EAST is a non-circular advanced steady-state experimental device and the first whole superconducting tokamak in the world. Vacuum system is one of the most important sub-systems of EAST device. Wall conditionings, such as baking, discharge cleaning and boronization, also play a very important role for the plasma operation. Due to Ion Cyclotron Resonance Frequency(ICRF) wall conditioning technique could be carried out in the presence of a high toroidal magnetic field, it is routine used for wall cleanings on EAST. After the 2nd campaign in 2007, the plasma facing walls was modificated to fullic carbon walls and vacuum system was upgraded to meet the requirment of particles exhaust. This paper will introduce the new statues of vacuum system, such as pumping, fueling and wall conditionings on EAST. Then the vacuum operation and wall conditionings in 2008 campaign is introduced.

Keywords: Vacuum, Wall conditioning, EAST
PFCS:

1. Introduction

The Experimental Advanced Superconducting Tokamak (EAST), formerly known as HT-7U, is a non-circular advanced steady-state experimental device. It had a major radius of R=1.75 m, a minor radius of a=0.4m. For divertor operation, an elongation of 1.2–2 and with single null divertor and doublenull divertor will be used. The scientific mission of the EAST project is to study the physical issues involved in steady-state advanced tokamak devices. The engineering mission of the EAST project is to establish the technology basis of fully superconducting tokamaks in support of future reactors. Coils on EAST is the first trial test in the world for the sake of International Thermonuclear Experimental Reactor (ITER). To achieve the steady state operation, the EAST comprises 16 D-shaped superconducting toroidal field coils, which can create and maintain a toroidal magnetic field B up to 3.5 T. The key components of EAST also include superconducting poloidal field coils, current leads and superconducting buslines, vacuum vessel, thermal shields, cryostat, divertor and in-vessel components[1-4].

The assembling of the device was completed in Jan. 2006 and in Mar. the cryogenic system was commissioned. The first plasma discharge was successfully achieved in EAST in 2006 [3,4], while the single-null and double-null divertor plasma discharges were achieved on fullic matel walls in Jan., 2007. After the 2nd campaign in 2007, the plasma facing walls were modificated to fullic carbon walls and vacuum system was upgraded to meet the requirment for particles exhaust. Reference[5-7] give the vacuum system before 2008. In the 3rd campaign in 2008, new big progresses, such as increasing heating power and extension of plasma duration, were made. This paper will introduce the new statues of vacuum system, such as pumping, fueling, and wall conditionings on EAST.

2. Vacuum system

2.1. Chambers

The EAST vacuum system is comprised of a few independent chambers, Plasma Vacuum Vessel (PVV), Cryostat Vacuum Vessel (CVV) and Cryogenic Valve Box vacuum chamber (CVB). The PVV consists of 16 completely welded stainless steel sections, with the capacity of resisting more than 13atm pressure difference between PVV and CVV, which indicated pumping for PVV could be seperated from others. The volume of PVV is about 40m^2 excluding 48 ports. Plasma facing area is about 60m^2. The surface of vessel walls, including window ports, is about 162m^2. If considering plasma facing components(PFCs), the surface should be increase more than 5 times in the view of outgassing from in-vessel components. Before 2008, the plasma facing materails was mainly made of stainless steel. In 2008, the PFCs, including divetors, were modificated to fullic carbon walls, doped garphite with 50~100um SiC coating. CVV has two parts, main body and current lead tanks(CLT). The former contains all the superconducting coils, inner and outer thermal shields with the volume of about 160 m^3. The later is comprised of two current lead tanks and current lead transfer lines, and the volume is about 22m^3. There are vacuum isolation blocks between these two parts for easier leak localization. However, the blocks are not strong enough to sustain a pressure difference as big as 1 atm, and there is a bypass tube connecting two parts. CVB contains the valves controlling the flow of the cryogenic circuits inside tree CVVs, and it is an independent chamber. The volume is about 16m^3.

The vacuum requirements are different for the vacuum chambers. For PVV, it is important to provide clean enviroment for plasma discharge. The designed ultimal pressure is 1.3×10^{-5} Pa. For CVV, it is required that the pressure should be low for a good thermal isolation, while it is crucial for a superconductin device to have higher vacuum for better electrical isolation after the coils are charged [2]. The design specifications for CVV are <0.1 Pa at room temperature and $<5\times10^{-4}$ Pa at surperconducting state. For CVB, design requirements are not as high as those for CVV, because there is no electrode inside.

2.2. Pumping station

These chambers have independent pumping systems. For the PVV, pumping system could be divided to three kinds, respectively for main chamber, divertor chamber and diagnostic system. The first, the pumps on a pumping duct (0.8 m in diameter and 6 m in length) connecting with one horizontal port of PVV including 4 sets of Turbo-Molecular Pumps (TMP) , each with the nominal pumping speed of 3.5m^3/s, as shown in figure 1. There are 3 sets of Roots (nominal speed of 0.6m^3/s) plus rotary pumping stations (0.07 m^3/s) acting as the fore pumps of the TMPs. One TMP station(0.45m^3/s) is also used as fore pumps of the main TMPs to improve the ultimate vacuum of PVV. Between the 3 TMPs and the Roots there is a liquid nitrogen trap of 0.07 m^3 for removing water from the pumped air and suppressing oil diffusion to the TMP stage. There are also 4 Cryo-Pumps (CP) on the duct, each with the nominal pumping speed of 13m^3/s for H_2, 17m^3/s for H_2O, 5.8m^3/s for air. Two more CPs are installed at the bottom ports and four new CPs are installed at top ports, connecting with the divertor region through tubes (2.5 m in length, and cross section area of 0.07 m^2). Beside those pumps outside the vessel, a new dedicated inner cryo-pump located under the outer target of low diveter was designed in 2008 for divertor pumping, as shown in figure 2. During this pump working, liquid helium and nidrogen flow flow continues in pipes. It takes about 3hr to be cooled down to 7.5K. One recycle of re-generation to 80K requires about

30min. The calibrated pumping speed for D_2 is about 7.5m^3/s , and it could absorp 2500Pa.m^3 D_2 before satuartion. Besides those pumps, there are a lots of pumps served for other system, which are connetced to PVV, such as pumps for LHCD system(one CP and one 1.5m^3/*s* TMP), for differential measurement system and diagnostic system. Two dry pumps are used for re-generation for those CPs.

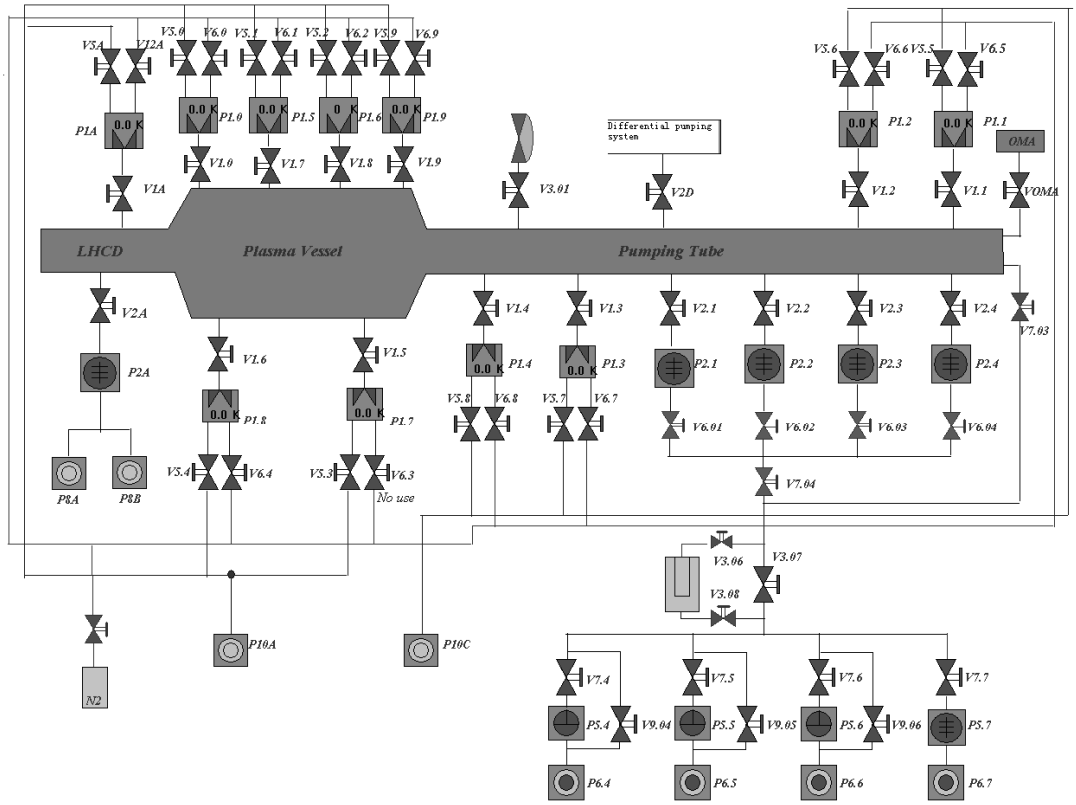

Fig.1. Main pumping system for plasma vacuum vessel of EAST

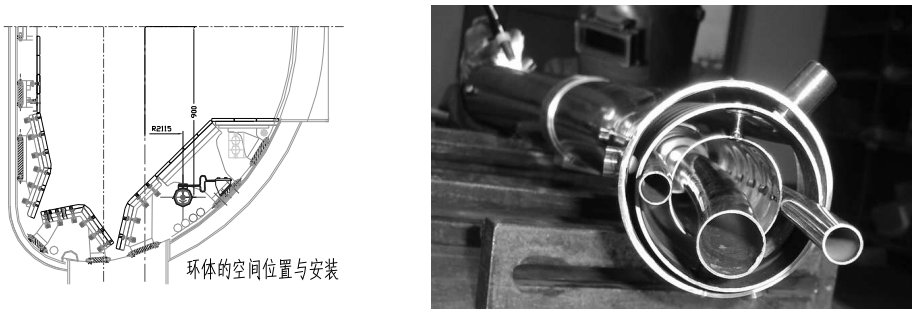

Fig.2. Inner vessel cryopump under outer target of low divertor in EAST

The pumping system of CVV main body is similar to that for PVV, as shown in figure 3. There are 4 sets of TMPs with lower pumping speed (each with the nominal speed of 1.5 m^3/s), and the fore pumps are the same as that for PVV. After cooling down of the cryostat, the magnet structure and its thermal shields act as a huge CP with superconducting coils at about 5 K and

thermal shields at about 80K. There are 3 more TMPs (each with nominal speed of 1.2 m^3/s) located at 2 current lead tanks and the transfer lines. For CVB, there is one TMP station with the pumping speed of 0.6 m^3/s.

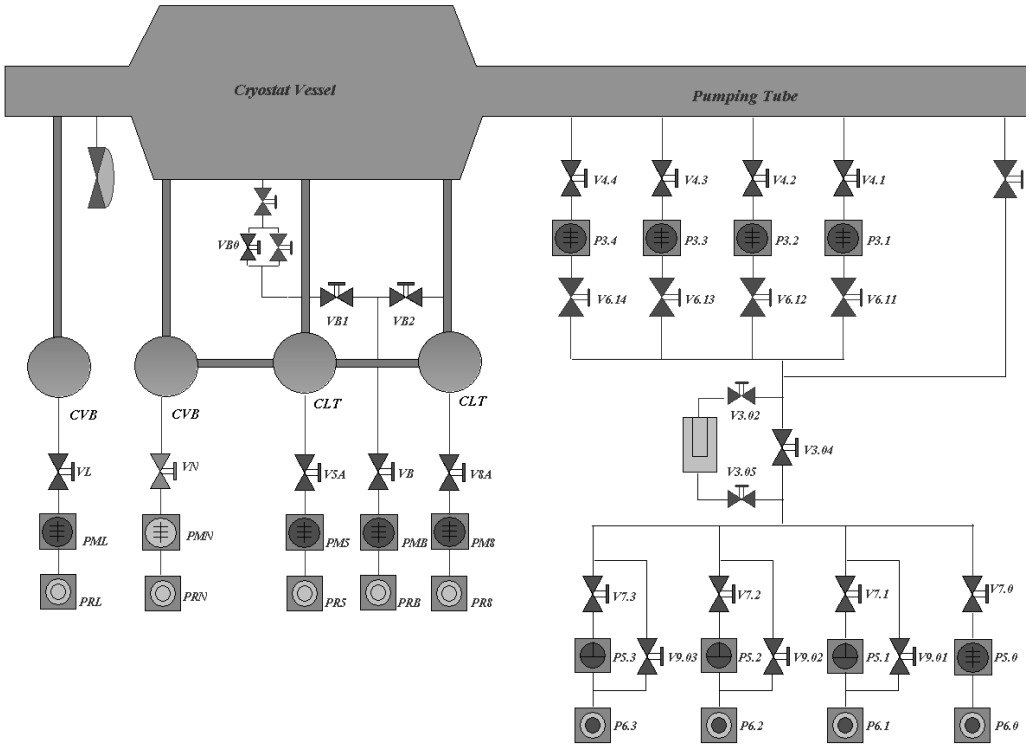

Fig.3. Pumping system for cryostat vessel and cryogenic valve box chamber of EAST

2.3. Gas injection system

The gas injection system is quite important for EAST operation. In present phase, plasma density feedback controlled gas puffing is the sole methode for plasma fueling on EAST. Another main functions of gas injection system is for wall conditioning with different working gases. Gas injection system also required to provide some special gas for physics research, such as diagnostic, heat load control and disruption mitigation.

The gas injection system include gas supply, transfer lines, gas tanks, pressure gauges and valves, as shown in figure 4. The injected gases during each plasma discharges could be measured by the gauges on standard tanks. And pressure in the tanks are kept in a range for presice measurement, which acheived by feedback controlled electrical magnetic valve. There are 12 plasma fueling ports for plasma fuleing at top and bottom divertors(outer and inner target, dome), and 4 ports at midplane(high and low field side). There are also 2 ports for gas injection during wall conditioning and one port for impurities injection. There are 9 piezo-valves for plasma fueling, and each one is used for two fueling ports. Two kinds of piezo-valves (maximum throughput being 60 and 4200 sccm respectively) are used.

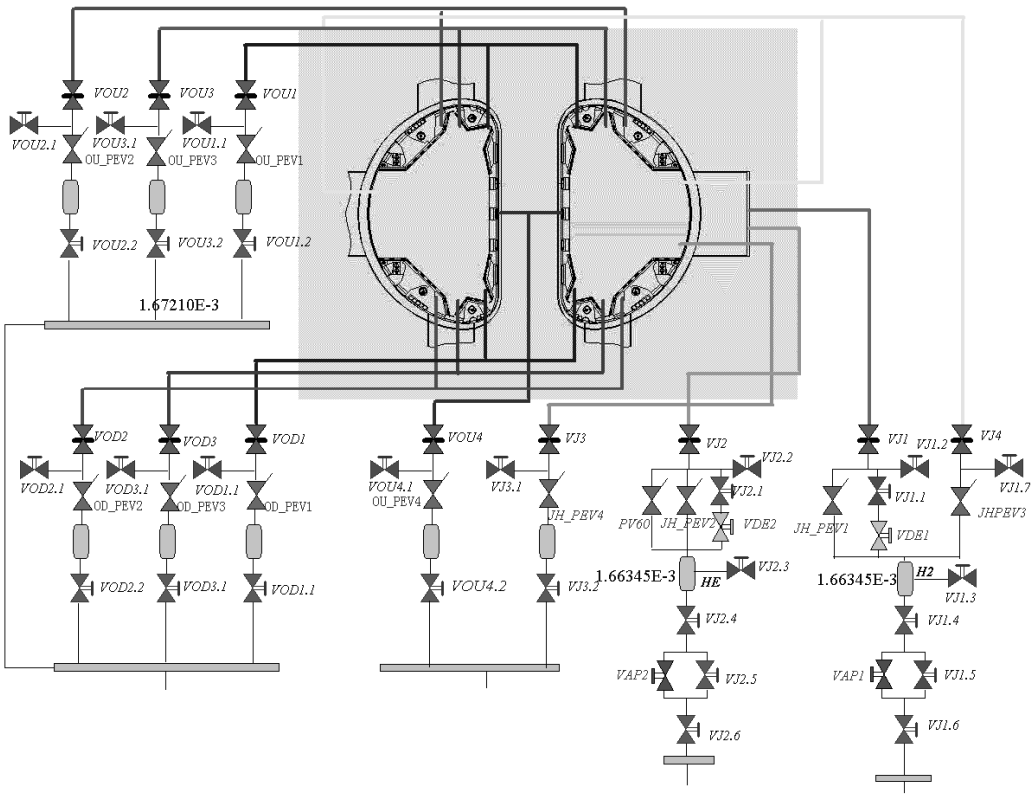

Fig.4. Gas injection system for EAST

The working gas for plasma fueling is hydrogen or deuterium. Helium, hydrogen, deuterium are main working gases for cleanings or wall conditioning. One electrical magnetic valve is utilized with the flow rate adjusted between 5×10^{-7} and 125 $Pa.m^3/s$ depending on discharge cleaning methods, GDC or ICRF cleanings. In some special experiments, other gases, such as oxygen, argon and nenium, could be supplied by this system, too.

2.4. Wall conditionings

To get plasma with low impurity level, it is very iportant to have a clean first wall. In the present campaign in 2008, the new full carbon wall was installed on EAST. Except for 2 movable limiters made of Molybdenum, all the plasma facing area is doped garphite with 50~100um SiC coating on copper alloy heat sinks, including the divertor area.

There are three sets of baking sub-systems for EAST, double shell and plasma facing components (PFC) hot air heating, windows port tube heating and PVV main pumping duct heating. Due to new heat sinks was mounted for PFCs, PFCs heating was changed to hot N_2 heating, which could pass the water cooling tubes in the copper alloy heat sinks, as shown in figure 5. Hot N_2 circulating inside the double shell between the PVV and main CVV bakes the plasma vessel walls. The heaters for windows tube and main pumping duct are eletronic resistence heaters, which could be switched off by centrol control during plasma discharges. Armored heaters are distributed uniformly on the surface of the pumping duct for PVV. Armored thermalcouplers are installed poloidally and toroidally on the PFC, port tubes and pumping duct. Due to lots of

valve and flange, maxium baking temperatuer for main pumping tube is 150°C. To meet the requirement of diagnostic system, the temperature of windows ports are limited lower than 120°C. PFCs could be baked to 350°C due to limit of the materials of PFCs and some diagnostic probes. To avoid the damage on the components in CVV, the vessel walls of PVV is limited under 150°C. During high parameters plasma operation, the heat sinks of PFCs required activited cooling by de-ionized water. Total water flow rate in PFCs is 111t/hr~167t/hr.

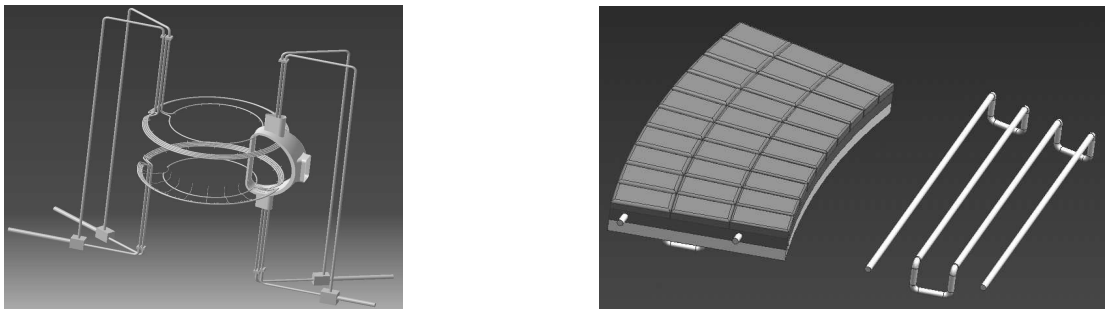

Fig.5. Hot N_2 circulating inside heat sinks and plasma vessel walls in EAST

On EAST, there are four stainless steel anodes, fixxed on the vessel wall of PVV, for glow discharge cleanings(GDC), as shown in figure 6 and 7. The maxium power for each anode is 15kW, and current is 15A. Voltage for gas discharge is about 1000V. During the cleanings, normal parameters are set with a current of 2A for each anode and working pressure is 0.5~10Pa. And normal working gases is He or D_2. The GDC system could be also used for boronization.

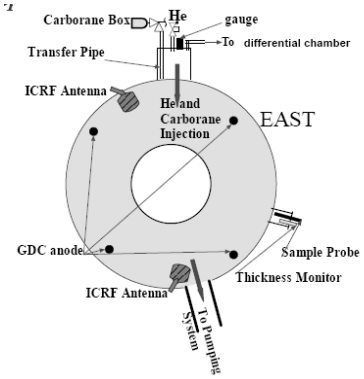

Fig.6. Set of wall conditionings system in EAST

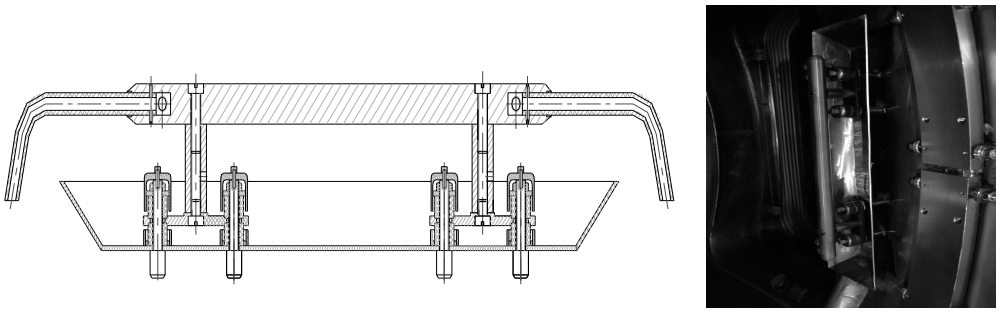

Fig.7. Structure of GDC anodes

The permanent presence of toriodal field in EAST will preclude GDC cleaning sometimes; therefore, ICR conditionings are envisioned for in-between pulse cleaning.

The primary advantage of ICRF cleanings/wall conditionings is that it could be applied with the existing of the toroidal magnetic field. The technique was successfully used on HT-7 in 1998 [8] and on EAST with fullic matel walls in 2007[9-10], and becomes one of the routine conditioning methods, especially for boronization and between discharges.

Two dedicated RF antenna was designed for ICRF wall conditioning, which located at low field side in EAST vessel, as shown in figure 6 and 8. The design are benificial for the coupling between ICRF plasma and antenna. The wave frequency of ICR is 30MHz; the wave power can easily be adjusted. The duty time of ICR wave is 0.3s on /1.5s off for cleanings. ICR cleanings/wall conditionings are performed in presence of permanent toroidal magnetic field (1~2T). The used RF power was in a range of 3~20kW(max.300kW, adjustable) and the working pressure was in a wide range from $4x10^{-3}$Pa to 10Pa.

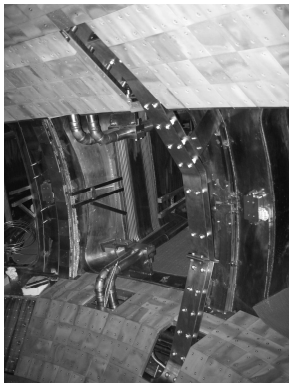

Fig.8 Dedicated ICRF antenna for wall conditionings in EAST

He-ICRF or D_2-ICRF cleanings are used for impurities and hydrogen removal. ICRF cleanings normally use to remove impurities at the early phase of plasma operation, after disruptive plasmas, before boronization and after oxidation experiments. It use to remove hydrogen specially at the interval of plasma discharges or after boronizations. Normally, during ICRF cleanings, four turbo-pump stations were used for particles exhaust. Removal rates of particles depended on power, working pressure, pumping speed and gas load on walls. D_2-ICRF cleanings seems much better than He-ICRF cleanings for the removal of impurities and hydrogen(Will be reported later).

In the HT-7 superconducting tokamak campaigns and EAST campaign with fullic metal walls, it was observed that boronization could suppress efficiently the high and low Z impurities in the plasma[8]. Same material, carborane ($C_2B_{10}H_{12}$) is used for EAST with fullic carbon walls in 2008. This kind of white powder has lower level of toxicity and higher stability than other boron compounds. It is heated during boronization, and the sublimation is led into the GDC or ICRF plasma through a high temperature tube. Residual gas analysis in the differential chamber and film thickness monitor are used for in-time monitoring of the process. Typic procedure of ICRF associated boronization includes three steps. Before boronization, the walls should be baked to avove 100^{o}C and ~1hr He-ICRF cleaning uses for wall cleanings; Then, 3~4hr $C_2B_{10}H_{12}$-ICRF boronization is carried out; After the boronization, 2~3hr He-ICRF cleaning would carried out for H removal. Main parameters for ICRF associated boronization are: ICRF Power is10-20kW, Wave duty time is adjustable, normally at 1s on/ 2s off, Toroidal magnetic field is set at 1~2 T, Total set pressure is 5×10^{-3}~1×10^{-2}Pa. In EAST, 10-15g $C_2B_{10}H_{12}$ use for one boronization.

2.5. Control and safeguard

The requirements for remote automation, distributed control and centralized management, high reliability and expansibility have been taken into account in the design of control system forvacuum system[5-7].

There are three levels of control in vacuum control system, as shown in figure 9. The bottom level control is performed on the local instruments manually; the medium level control is based on Siemens S7-400 PLC; the top level control is conducted on IPCs with communication through profi-bus net work. In addition remote handling and centralized monitoring could be realized by a remote control server.

The control system could achieve pumping and fueling of the whole vacuum system. Besides that, it also includes the data acquisition of the pressure and temperature.The details are on the monitoring of vacuum system states, including cooling water, power and compressed air,etc., safeguards of plasma chamber and cryostat chamber and vacuum equipments, choosing of control modes corresponding to the plasma discharge and wall conditioning.

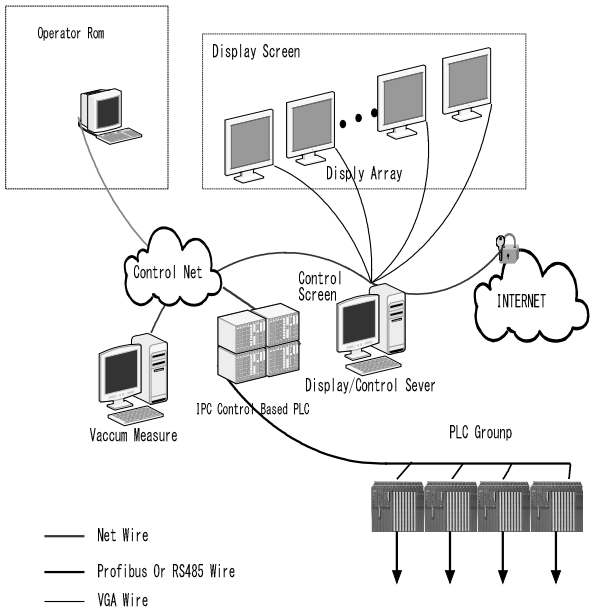

Fig.9. Control system for vacuum opertion and wall conditionings on EAST

Safeguard is crucial for the operation of a superconducting tokamak. The running risks are categorized into 3 levels. The primary one would potentially cause damage to the device. The medium one could potentially cause damage to the vacuum system. The mildest one would influence the experimental operation. The judgement is based on the monitoring of the whole and partial pressure, and the states of the vacuum system units. The alarms are shown on the vacuum control station, and two levels of alerts are sent to the central control station. The high risk alert requires the central controller to stop experiment and discharge current in all the coils, while the low risk alert requires that the experiment be terminated but toroidal field current be kept.

3. Vacuum system operation in 2008

3.1 Vacuum operation of PVV

After vacuum system upgraded, vacuum system was suceesfully operated in the 3rd campaign of EAST in 2008. It taked the rotary pumps about 4hrs to pump down to 1000Pa, when the roots could be put into use, and 1-2hrs before starting TMP. During pumping down, carefully leak detecking was done, specially for heat sinks of the new carbon PFCs.

After leak detecting, baking was conducted continuously and cryo-pumps were put into use. He-GDC cleanings were carried out when the partial pressure of water was $<1\times10^{-4}$ Pa. After long baking (200^{o}C, ~10days) and He-GDC cleanings(~110hrs.), the vacuum reached ~1×10^{-5}Pa. Most of the time, the temperature of PVV vessel walls and heat sinks was kept at 150~200^{o}C by hot N_2 heating. The temperature of windows port tubes was lower than 120^{o}C. For the pumping duct, the maximum temperature was kept lower than 110^{o}C. Before plasma operation, H_2 removal was about 5.85×10^{23} by 112.5hr. He-GDC.

During plama operation, lots of He-ICRF and D_2-ICRF cleanings(20min.~a few hrs.) were done for H and impurities removal at the interval of plasma discharges; During plasma operation, total H_2 removal was ~1.1×10^{23} by 2778min. He-ICRF and ~0.8×10^{23} by 780min. D_2-ICRF. During the campaign, inner liquid helium cryo-pump was also successfully tested. With the inner cryo-pump working, the base vacuum in PVV reached 7.6×10^{-6}Pa.

Depended on the missions of plasma operation, boronization will carried out during plasma operations. In this campaign, three ICRF associated boronization were carried out. During the boronization, ICRF would effectively dis-sossicaite and ionize the boron material. After boroniztaions, impurities, such O, were successfully suppressed. The boronizations were benificial for optimization of plasma start-up, ramp-up and shaping for single and double null configurations. It also extened the operational region and improvement plasma performance. However, lots hydrogen was remained on the films which lead high recycling during plasma dicharges. So, after boronization, it required enough cleaning by ICRF.

During this campaign, plasma fueling at different port was also tested, which benificial for plasma shaping and heat load reduction. Mostly EAST utilized frequency modulation mode to feedback control plasma density. Plasma with density higher than the Greenwald limit is obtained.

The successful operation of vacuum system and better aranged wall conditionings played an important role for the successful plamsma operation. In this campign, reliable plasma with limiter and divertor configurations(single/Double null) was sucessfully obtained. Plasma paramters were improved. Plasma heating power increased, eg, LHCD injection power reached 800kW and ICRF injection power reached 260kW. Normal Plasma density is $1\sim4\times10^{19}$/cm^3. Plasma current reached 0.6MA. Repeatable long plasmas over 20s were obtained with a plasma current of 250kA and that over 10s with a current of 400kA.

3.2 vacuum operation for CVV and CBV

For CVV main body, it taked a little longer period (e.g. about 5 hour) before starting the Roots, and 1-2 hours before the TMPs were started. The pumping for the current lead tanks and CVB taked much shorter time. After cooling down to the working temperature, the ultimate pressure of CVV and CVB could easily reached a few 10^{-5}Pa.

Leak detecting is essential for the success of the engineering commissioning, especially for such a whole superconducting device. The sealing for the CVV is mainly rubber. The most crucial leak is that of the coolant circuit inside CVV. Taking the toroidal field coil as an example, it consists of 16 cages, therefore, during the construction, it was designed that leakage for each cage

should not exceed $3\times10^{-8}Pam^3/s$, considering welding is needed to form a whole unit. An important part of the vacuum operation is to ensure that each cooling circuit meets the leak control requirements. It was fund that the biggest leak in the CVV is the outer thermal shield circuit with a leakage of $10^{-5}Pam^3/s$, which have no effect on the vacuum to a few $10^{-5}Pa$.

4. Summary

After the plasma facing walls was modificated to fullic carbon walls and vacuum system was upgraded to meet the requirment of particles exhaust. This paper have introduced the new statues of vacuum system, such as pumping, fueling and wall conditionings on EAST, and the vacuum operation and wall conditionings in 2008 campaign. New vacuum system and wall conditionings system are reliable for EAST operation. Specially, ICRF cleanings become routine wall conditionings for EAST; ICRF boronization is effective methodes to supress impurities and to improve plasma properities.

Acknowledgments

This work was funded by the National Nature Science Foundation of China under contract No.10705030. This work was partly supported by the JSPS-CAS Core-University Program on Plasma and Nuclear Fusion.

Reference

[1]Y.X.Wan,HT-7Team,HT-7UTeam, Nucl.Fusion 40(2000)1057

[2] Wan Y.X. *et al*, *Plasma Sci. Technol.* 8(2006) 253

[3] Y. Wan, Overview progress and future plan of EAST project, 21st IAEA FEC, OV/1-1, Chengdu, China, 16-21 October 2006

[4] Xiang Gao et al, Nucl. Fusion 47 (2007) 1353

[5]Y. Yang et.al., Vacuum operation of first divertor campaign on Experimental Advanced Superconducting Tokamak (EAST), 17th International Vacuum Cong ress, Stockholm July 2-6, 2007

[6]X.M.Gu ,etal.,Plasma Sci.Technol.2(2000)557

[7] L. Wang et al., Fusion Engineering and Design, 83(2008)295

[8] J. Li et al., Nucl. Fusion v.39/no.8 (1999) 973-978

[9]J.S Hu, et al., Fusion Engineering and Design 83 (2008) 689

[10]X.Gao, et.al., ICRF wall conditioning and plasma performance on EAST, 18th International Conference on Plasma Surface Interactions, Toledo, Spain, May 26-30, 2008

Material Properties of Tungsten Coated F82H Ferritic/Martensitic Steel as Plasma Facing Armor

Y. Yahiro[1], N. Yoshida[2], M. Mitsuhara[1], H. Nakashima[1], T. Hirai[3], M. Tokitani[4], K. Ezato[5], S. Suzuki[5], M. Akiba[5]

1 Interdisciplinary Graduate School of Engineering Sciences, Kyushu University, Kasuga, 816-8580 Japan
2 Research Institute for Applied Mechanics, Kyushu-u University, Kasuga, 816-8580 Japan
3 Forschungszentrum Juelich, Juelich, Germany
4 National Institute for Fusion Science, Toki, 509-5292 Japan
3 Japan Atomic Energy Agency, Tokai, 319-1184 Japan

E-mail of corresponding author: yoshida@riam.kyushu-u.ac.jp

Abstract

Two types of plasma spray tungsten coatings on ferritic/martensitic steel F82H made by vacuum plasma spray technique (VPS) and air plasma spray technique (APS) were examined in this study to evaluate the possibility as plasma-facing armor. The VPS-W/F82H showed superior properties. The porosity of the VPS-W coatings was about 1% and most of the pores were smaller than 1-2 μm and joining of W/F82H and W/W was fairly good. Thermal load tests indicated high potential of this coating as plasma-facing armor under thermal loading. In case of APS-W/F82H, however, porosity was 6% and thermal load properties were much worse than VPS-W/F82H. It is likely that surface oxidation during plasma spray process reduced joining properties.

Keywords: vacuum plasma splay coating, tungsten, F82H, plasma facing armor

1. Introduction

Tungsten (W) is promising plasma facing armor material for the future fusion devices. The advantage of W is the high melting point, low tritium inventory and low erosion rate under plasma loading [1, 2]. The main drawbacks of W are the high ductile to brittle transition temperature (DBTT, approximately 400°C) and difficulties in machining. A possible solution for the utilization of tungsten at plasma facing surfaces is the coating of the heat sink or structural material with a thin tungsten layer. As coating technologies, vacuum plasma spray (VPS) [3], physical vapor deposition (PVD) [4, 5] and chemical vapor deposition (CVD) [6], have been proposed and tested under high heat flux loading. As substrate materials for W coating, the following materials have been applied: copper or copper alloys foreseen in concern of water cooled system, graphite and/or CFC [7-10] for inertially cooled system and reduced activation ferritic steel [11]. In the present study, F82H ferritic/martensitic reduced activation steel, which is a leading structural material candidate for a fusion demonstration reactor, was selected as the substrate.

In this paper, characterization of thick plasma spray coatings of W on F82H steel and the evaluation of impacts of various heat treatments on the coating systems are presented.

2. Experimental Procedures

Reduced activation ferritic steel substrate with dimension of 20 mm×20 mm×2.5 mm and 50 mm×50 mm×5 mm were coated by vacuum plasma splaying technique (VPS) and also by air plasma splay (APS). The substrate material was F82H, (Fe-8Cr-2W) developed by JAEA. Its thermal expansion and thermal conductivity at 300K are $11.7 \times 10^{-6}\ K^{-1}$ and $0.82 W/cm^{-1}K^{-1}$, respectively. After roughing the surface of the substrate by blast treatment for better adhesion, APS and VPS were performed at TOCALO Co. Ltd. in Japan. The thickness of the coating layer in both cases is 1.0 mm. In order to suppress oxidation and change of the ferritic/martensitic structure during the spraying processes, bulk temperature of the substrate was kept below 150 °C and 600 °C for APS and VPS, respectively. The average size of the W powders for APS and VPS were 40 μm and 17 μm, respectively.

In order to examine metallurgically, microstructure of the coatings and the substrate were observed by means of scanning electron microscopy (SEM), orientation imaging microscopy (OIM) and transmission electron microscopy (TEM). OIM gives the 2-D information of the orientation of each crystalline grains and local strain. In order to obtain thin foil specimens of about 100 nm-thick for TEM observation, cross-sectional specimen preparation technique with a focused ion beam device (FIB) was used. Local hardness was measured by a nano-indenter.

Thermal response tests were carried out in the electron beam facility JUDITH at Forschungszentrum Juelich [12, 13] and ACT at NIFS.

3. Results

3.1 Structure

SEM micrographs in Fig.1 show surface morphology of VPS-W and APS-W, and the corresponding cross sectional structures. The surface of VPS-W has very fine rough structure. In addition, many spherical particles of about 20 μm or less, which probably have not melted perfectly during the plasma spray process, exist on the surface. Such very rough surface morphology indicates that the temperature of the melted particles was not high enough to form ideal pan cake-like depositions with smooth surface. On the other hand, the surface of the APS-W is smoother and the number of the un-melted particles is lower. These results indicate that the heating power of the plasma for VPS process was not high enough to form smooth surface. The cross-sectional SEM micrographs show that pores size is small in the VPS-W (less than 1-2 μm), in spite of the very rough surface. In case of APS-W, however, many pores larger than 10 μm remain. Reflecting the size of the pores, the porosity of VPS-W and APS-W estimated from the cross-sectional SEM micrographs were 1% and 6%, respectively. The low porosity of the VPS-W indicates that quite good thermo-mechanical properties would be expected.

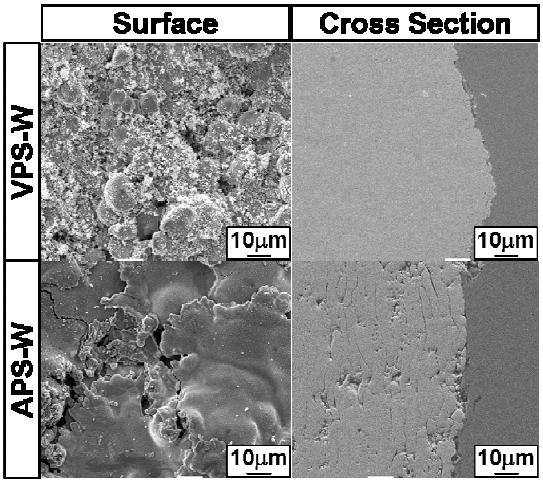

Fig.1 SEM micrographs showing surface morphology of VPS-W and APS-W, and the corresponding cross sectional structures.

In order to know the effects of the plasma spray on phase stability of the F82H, the cross sectional samples of VPS/F82H and APS/F82H were observed by means of OIM. Typical

inverse pole figure (IPF) images and misorientation maps at and near the interface of VPS-W/F82H and APS-W/F82H are shown in Fig.2. In both cases, distribution of the rotation angle between the neighboring grains estimated from the IPF images had peaks at 50º and 60º. This fact indicates that most of the crystalline grains are martensite. It means that the surface temperature was successfully suppressed not to exceed the phase transformation temperature from martensite to ferrite (770°C). The misorientation map of VPS-W/F82H, however, shows that residual strain exists in the vicinity of the interface of about 20μm. Micro-harness at this area measured by a nano-indenter was about two times higher than that of matrix.

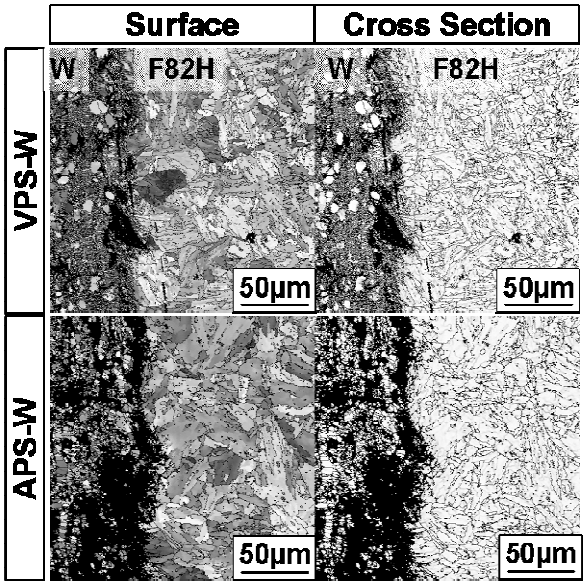

Fig.2 Typical inverse pole figure images and misorientation maps at and near the interface of VPS-W/F82H and APS-W/F82H.

Fig.2 also shows that re-solidified pan cake-like depositions of W have columnar structure. The size of the columnar crystals in VPS-W is much smaller than those of APS-W. Relatively large round-shaped grains must be un-melted W powders, which are also visible in Fig.1.

In order to know the details of the microstructure, very thin cross sectional TEM specimens were picked up by using FIB. Fig. 3 (a) shows a typical micrograph at the VPS-W/F82H interface. It is remarkable that no precipitations such as WC were formed at the interface and in the matrix. Excepting relatively large pores, joining properties looks rather good. Joining between the splashed pan cake-like depositions also looks good, though fine pores less than 0.5μm remains (see Fig.3 (b)). The columnar structure developed well where the two pan cake-like deposits join well, but not around large pores.

The experimental results mentioned above indicate that joining of W and F82H and also W and W in VPS-W/F82H is metallurgical good. Reduction of pores size less than 1μm is a key issue for the material improvement.

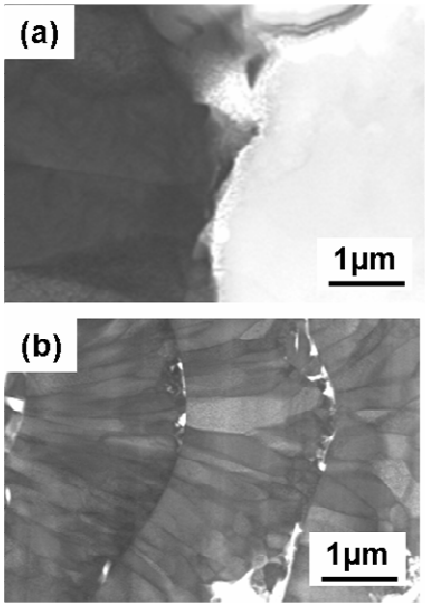

Fig.3 TEM micrograph at VPS-W. (a) Interface, (b) Tungsten layer.

3.2 Thermal response of the coatings

Thermal response tests were carried out in the electron beam facility JUDITH. Fairly homogenous distribution of heat deposition is realized by fast scanning of the electron beam. For the thermal response tests, moderate thermal impulses were applied for 1 ms. In this duration, the heat propagates in the range of characteristic heat propagation distance around 340 μm by assuming bulk W [14]. Note that the thermal diffusivity of W coating is smaller than bulk W, therefore, the distance is much shorter. This indicates that the thermal response tests reflect thermal

properties of W coating (1 mm thick) but not those of the interface and substrate.

Figure 4 shows surface temperature increases of APS-W, VPS-W coatings and a bulk W as a function of power density. The surface temperature of APS-W was significantly higher than the others. The temperature increase was fairly linier dependence as indicated in equation (1)

$$\Delta T = 2P \times t^{0.5} \times (\pi \times \lambda \times \rho \times c)^{-0.5} \quad \text{---------- (1)}$$

where P stands for power density [W/m^2], t for time [s], λ for thermal conductivity [W/m/K], ρ for density [kg/m^3], c for specific heat [J/kg/K]. Comparing surface temperatures at a power density, it is possible to evaluate the ratio of material constants (M = (λ·ρ·c)). Consequently, the material constant of APS-W and VPS-W were estimated to be 17 % and 58 % of the bulk W. It shows clearly that VPS-W had higher performance than APS-W coating. It is likely that the inferior material constant of APS-W coating was caused by the higher porosity and high impurity content. The quality of the coatings still needs to be improved.

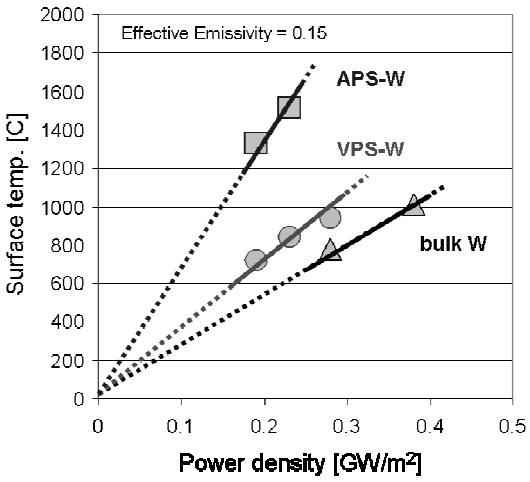

Fig.4 Surface temperature of APS-W, VPS-W coatings and a bulk W as a function of power density.

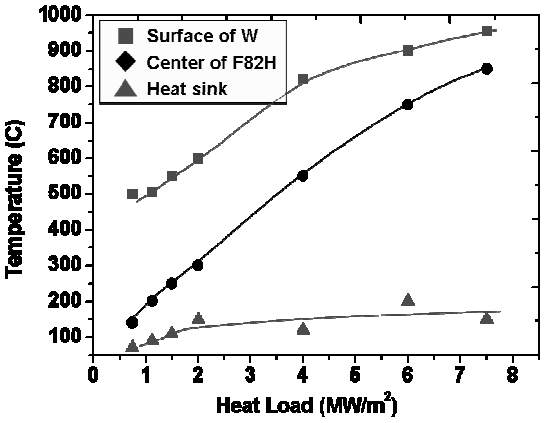

Fig.5 Saturated temperatures under pulse heat load for 20s.

3.3 Long pulse repetitive heat load test

Long pulse repetitive heat load test were performed by using ACT at NIFS. VPS-W/F82H samples (1mm-thick W/5mm thick-F82H) mechanically fixed on a water-cooled copper heat sink was exposed to electron beam for 20s. Heat load was increased stepwise from 0.75MW/m^2 to 7.5MW/m^2. At 2.25, 4.25 and 7.5MW/m^2, pulse heat load for 20s were repeated for 50, 16 and 16 times, respectively. Figure 5 shows the temperatures at the surface of W, center of the F82H substrate and Cu heat sink. Taking into account the temperature gradient in the samples depending on the heat conductivity and thickness, the temperature at the interface is estimated to exceed the martensitic transformation temperature (770^{o}C) above 4-4.5MW/m^2. Figure 6 shows the SEM micrographs of the W surface after cyclic heat load at 4.25MW/m^2 and 7.5MW/m^2. No cracking occurred at 4.25MW/m^2 but large perpendicular clacks are formed at 7.5MW/m^2. Cross sectional SEM observation indicates that cracks parallel to the interface are also formed in W near the

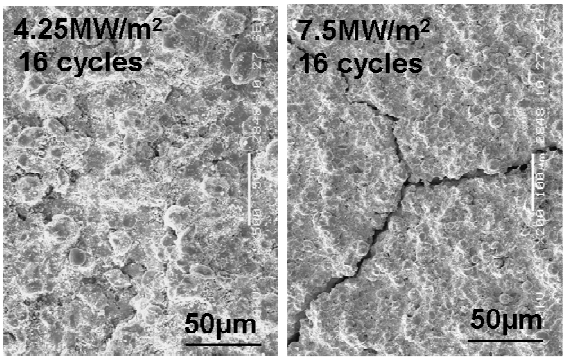

Fig.6 SEM micrographs of the W surface after cyclic heat load at 4.25MW/m^2 and 7.5MW/m^2

interface. No cracking occurred at the interface but a reaction layer was formed. F82H base also suffered strong influence of heating; the ferritic phase area expanded as expected from the temperature under the heat load. These experimental results indicate the present VPS-W/F82H can be used under the heat load at least up to 4MW/m^2 and has high potential as an armor material of the first wall.

4. Discussions

APS method is very attractive because the technique is rather simple and thus application is wider. However, as descried in 3.1 the porosity of APS-W/F82H is about 6%, which is one order higher than that of VPS-W/F82H. It is considered that this high porosity resulted in the weak heat load resistance as mentioned in 3.2 due to reduction of effective thermal conductivity. Plasma spray of melted W powders was performed by scanning the plasma gun on the substrate. It means that there was rather long time interval until the next scanning coming (about 1-2 s in the preset case). Therefore, the fresh surface of the deposited W will be oxidized quickly in air during the time interval. Once the remarkable oxidation occurred at the solid W surface, strong sticking of the melted droplets on the solid surface will become difficult and as a result large pores will be formed. It is considered that the application of APS technique will be limited for our purpose.

The preliminary thermal response test and repetitive long pulse heat load test described in 3.2 and 3.3 indicate that VPS-W/F82H has considerably good heat load resistance. The porosity of VPS-W/F82H is very low but it has still fine pores less than 1-2 μm as shown in the TEM micrographs of Fig.3. In order to improve heat load resistance, one should know the mechanism of the fine pores formation at first. Very fine columnar crystal structure in splashed pan cake-like depositions and very limited area with smooth surface comparing to the APS-W/F82H indicate that the temperature of the melted W powders was not high enough. Existence of un-melted round W crystals also indicated the insufficient heating power of plasma. If the temperature of the melted droplets of W is high enough, they can penetrate well into the fine holes and even shadows before re-solidification. It is expected that the porosity and adhesion strength can be improved by optimizing the powder side of W and plasma heating power.

5. Summary

Two types of plasma spray tungsten coatings on ferritic/martensitic steel F82H made by vacuum plasma spray technique (VPS) and air plasma spray technique (APS) were examined in this study to evaluate their possibility as a plasma-facing armor.

The porosity of the VPS-W coatings was about 0.6-1.0%. The cross sectional TEM observation showed that most of the pores were smaller than 1-2μm and joining condition of W/F82H and W/W was fairly good. No remarkable carbides and oxides were observed at the interface. Thermal response test and repetitive long pulse heat load test indicated high potential of this coating as plasma-facing armor under thermal loading. It is likely that the VPS-W/F82H examined in the present work showed good performance up to the heat load of 4MW/m2. For the reduction of fine pores usage of smaller W powders and/or increasing of power of plasma splay gun will be effective. In case of APS-W/F82H, porosity was 6% and heat load properties were much worse than VPS-W/F82H. It is likely that surface oxidation during plasma spray process deteriorated joining properties. Application of APS-W for a plasma-facing armor will be limited. Remarkably, both coatings created soft interlayer after

proper heat treatments probably due to high residual stress at the interfaces after the production. This indicates the potential function of the soft interlayer as stress relieve and possible high performance of such coating component under thermal loads.

Acknowledgements

This work was partly supported by the JSPS-CAS Core University Program in the field of Plasma and Nuclear Fusion.

References

[1] G. Federici, C.H. Skinner, J.N. Brooks, J.P. Coad, C. Grisolia, A.A. Haasz, et al., Nucl. Fusion 41 (2001) 1967.
[2] I. Smid, M. Akiba, G. Vieider, L. Ploechl, J. Nucl. Mater. 258–263 (1998) 1602.
[3] S.Deschka, C.Garcia-Rosales, W. Hohenauer, R.Duwe, E. Gauthier, J. Linke, M. Lochter, W. Mallener, L. Plochl, P. Rodhammer, A.Salito, J.Nucl. Mater. 233-237(1996) 645.
[4] H. Maier, ASDEX Upgrade team, J. Nucl. Mater. 335 (2004) 515.
[5] H. Maier, et al. J. Nucl. Mater. 363–365 (2007) 1246.
[6] T. Hirai et al. Fusion Engineering and Design 81 (2006) 175.
[7] K. Tokunaga, Y. Kubota, N. Noda, Y. Imamura, A. Kurumada, N. Yoshida, T. Sogabe, T. Kato, B. Schedler, Fusion Eng. and Design 81 (2006) 133.
[8] K. Tokunaga, R.P. Doerner, R. Seraydarian, N. Noda, N. Yoshida, T. Sogabe, T. Kato, B. Schedler, J. Nucl. Mater. 307-311(2002) 126.
[9] K. Tokunaga, N. Yoshida, Y. Kubota, N. Noda, Y. Imamura, A. Kurumada, T. Oku, T. Sogabe, T. Suzuki, T. Kato, L. Plöchl, J. Plasma Fusion Res. SERIES, 3 (2000) 260.
[10] K. Tokunaga, N. Yoshida, N. Noda, K. Kubota, S. Inagaki, R. Sakamoto, T. Sogabe, L. Ploechl, J. Nucl. Mater. 266-269(1999) 1224.
[11] H. Greuner, H. Bolt, B Boeswirth, S. Lindig, W. Kuehnlein, T. Huber, K. Sato, S. Suzuki, Fusion Eng. Design 75-79 (2005) 333.
[12] R. Duwe, W. Kuehnlein, H. Muenstermann, Proc. 18th Symposium on Fusion Thechnology (SOFT), Karlsruhe Germany, (1994) 355.
[13] T. Hirai, K. Ezato, P. Majerus, Materials Transactions, 46 (2005) 412- 424.
[14] T. Hirai, G. Pintsuk, Fusion Eng. and Design 82 (2007) 389–393.

Primary investigation of power exhaust capability of the belt limiter in HT-7

J. F. Ruan, J. L. Chen, J. G. Li, C. Y. Xie
Institute of Plasma Physics, Chinese Academy of Sciences, Hefei 230031, PR China
E-mail of corresponding author: jfruan@ipp.ac.cn

Abstract

In order to improve power exhaust capacity in longer pulse discharge, inner components including the belt limiters were upgraded in HT-7 vacuum vessel before the 2008 spring campaign. The longest discharge duration has reached from 306s to more than 399s, which proves that the change in the HT-7 device was very successful. The simulation and observation of the power deposition on the belt limiter has been carried out and these results have demonstrated that the power exhaust capacity of belt limiter can afford the long operation.

Keywords: Power exhaust, HT-7, belt limiter

1. Introduction

The increase in auxiliary heating power in present day machines has led to the improvement of plasma facing components (PFCs) to reduce the heat flux. Power exhaust strongly influences on their design. In-vessel integration of actively cooled plasma facing components (PFCs), which can protect vessel against heat and particle flux, are required by long and efficient plasma discharges in order to operate current tokamak at steady state [1, 2].

From the spring campaign of 2003, HT-7 was equipped with one high field side belt limiter with stainless steel heat sink. In the followed yeas, the longest discharge pulse has reached to 306 s. But in many plasma discharges which were longer than 30 s, the temperature at the belt limiter surface were over 1000℃ and the ends of the belt limiter suffered serious damage. Abundant impurities were induced by chemical sputter, therefore long pulse-length plasma discharges could not be sustained [3]. To enhance power extraction capacity and promote plasma duration, HT-7 was equipped with actively cooled belt limiter with CuCr heat sink in the spring campaign of 2008 (Fig. 1).

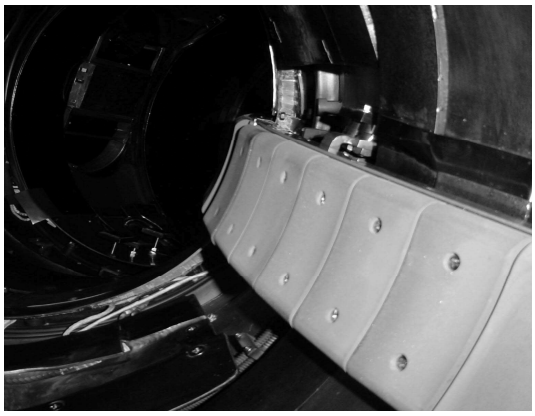

Fig. 1 The upgraded belt limiter at the high field side of HT-7.

2. Assessment of power deposition on the belt limiter

The ANSYS finite element code is used for the assessment of power deposition of on the surface of the belt limiter. Due to the symmetry, only the cross-section of the belt limiter is simulated. The conditions which were assumed are followed. The diameter of water tube is 10mm. The tube water velocity of 4 m/s and an average temperature of 37℃ was assumed. Based on the magnitude of heat flux deposited on the limiter surface of HT-7, the steady state heat flux of 2 MW/m^2 was loaded on the top surface of the belt limiter.

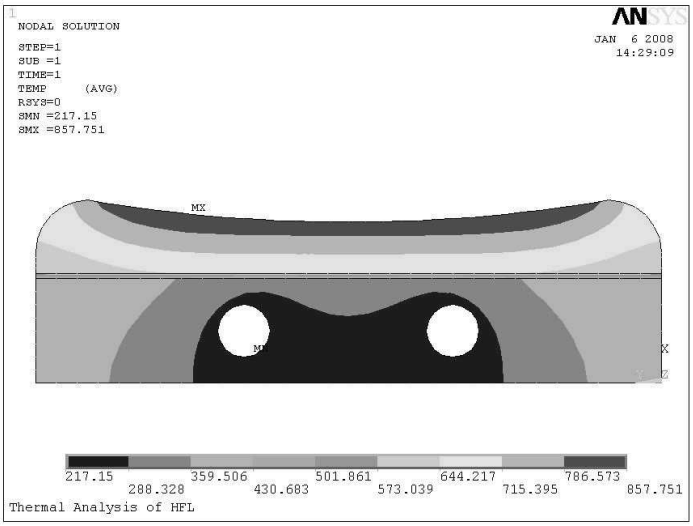

Fig. 2 The temperature profile of the belt limiter. It is from ANSYS finite element code.

Fig. 2 shows the result of the temperature profile. The maximum temperature is 857℃ which is acceptable for long duration discharges. This demonstrates that the power exhaust ability of belt limiter improves after upgraded with CuCr heat sink and can protect the surface from serious damage so that meet the need of long pulse discharges

3. Experimental results

Since the belt limiter upgraded for the long pulse discharges, the longest discharge of shot No. 100358 in this campaign is selected to evaluate the effect. Long duration discharges were performed using a double control: plasma current and position was controlled by the ohmic poloidal system, and central line averaged electron density was controlled by feedback control of deuterium gas injection using a pulsed piezo-electric valve. The longest discharge shot 100358 in Fig. 3, is more than 399s, which has demonstrates well the new PFC, power and particle injection and exhaust capabilities.

The maximum temperature on the surface of the belt limiter was not more than 200℃ (Fig. 4). The temperature of the place where the rise of the temperature was maximum before upgrade and existed hot spot, was not higher than 50℃ (Fig. 5). High performance belt limiters with copper alloy heat sinks and special structure design have played an important role to improve heat removal. By sharing the power deposited on a large area and increasing heat removal capability of PFCs, the

temperature was limited at low values so that impurity production was effectively suppressed.

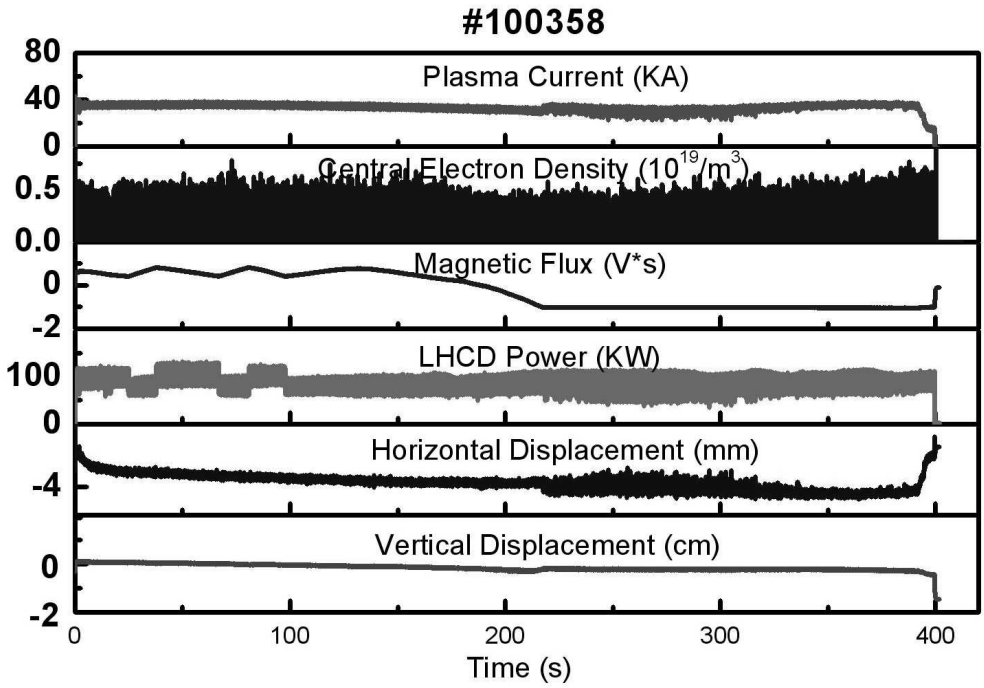

Fig. 3 The longest discharge of more than 399 s in the spring campaign of 2008.

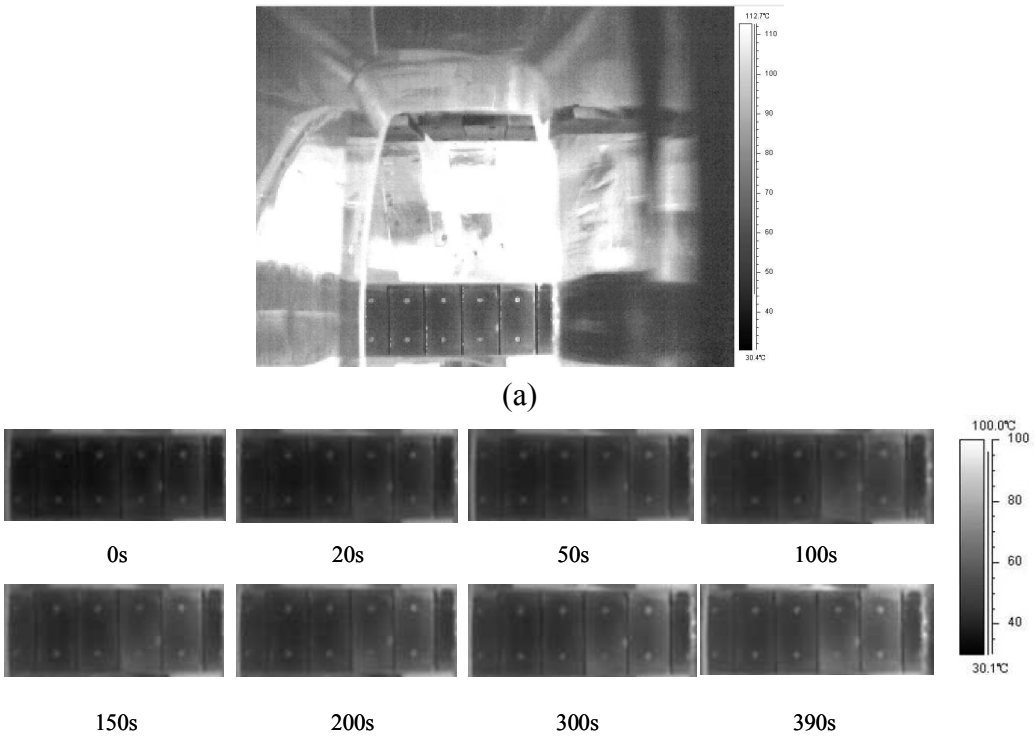

Fig. 4 Temperature profile of shot #100358 measured in IR-camera. (a)The temperature map at the end of the discharge. (b)Time evolution of the surface temperature of the belt limiter.

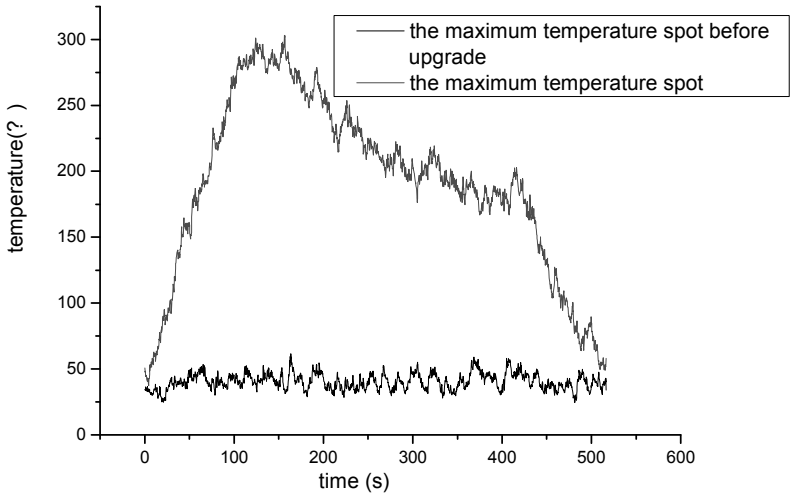

Fig. 5 Temperature measured by thermocouple.

4. Summary

To enhance power removal capacity, a new belt limiter at the high field of HT-7 was mounted in the spring campaign of 2008. By properly design, it can handle a heat load of 1-2 MW/m2 and pulse length of few hundred seconds. It was essential to improve high performance long pulse operation for the HT-7 superconducting tokamak. Long duration and high power plasmas were easily obtained with the upgraded limiter system.

Acknowledgements

The authors would like to thank H. W. Lu and Q. Li from Institute of Plasma Physics, Chinese Academy of Sciences for providing help and valuable discussion. This work was partly supported by the JSPS-CAS Core University Program in the field of Plasma and Nuclear Fusion.

References

[1] J. J. Cordier, Tore Supra Team, Fusion Eng. And Design, **61-62**(2002)71-80.
[2] G. Federici, C. H. Skinner, J. N. Brooks, et al., Nucl. Fusion, **41**(2001)1967-2137.
[3] J. S. Hu, J. G. Li, X. D. Zhang, et al., High Power Laser and Particle Beams, **16**(2004)597-602.

Deuterium Retention and Desorption Behavior of Tritium Breeder, Lithium Titanate After Deuterium Ion Irradiation

T. HINO, H.SHIBATA, Y. NOBUTA, Y. YAMAUCHI
Laboratory of Plasma Physics and Engineering, Hokkaido University, Kita-13, Nishi-8, Kita-ku, Sapporo, 060-8628 Japan
M. AKIBA, S. SUZUKI, H.TANIGAWA
Naka Fusion Institute, Japan Atomic Energy Agency, Naka-shi, Ibaraki-ken, 311-0193 Japan

Abstract

Lithium Titanate (Li_2TiO_3) pebbles were irradiated by deuterium ion (D^+, 1.7 keV) under different irradiation temperatures (RT, 473 K, 573 K, 673 K and 773 K), and the amount of retained deuterium and the desorption behavior were investigated by using a technique of thermal desorption spectroscopy (TDS). The amount of retained deuterium was almost the same with the irradiation temperature up to 473 K, while the amount decreased sharply with increase of irradiation temperature in the range higher than 473 K. The amount of retained deuterium at the irradiation temperature of 773 K became almost zero. This result suggests that the tritium produced in Li_2TiO_3 pebbles in the region with temperature higher than 773 K completely desorbs during the operation, although a small fraction of the tritium remains in the pebbles in the region with temperature lower than 773 K.

1. Introduction

Lithium Titanate (Li_2TiO_3) pebble is employed as the solid tritium breeding material in a test blanket module (TBM) of ITER [1]. As the solid breeder material, Li_2TiO_3 shows good chemical stability and tritium (T) release by thermal desorption [2,3]. In the fusion blanket, the pebbles are irradiated by fusion neutrons and then tritium is produced by nuclear reactions of ^{6}Li (n, α) T or ^{7}Li (n, n α) T in the pebbles. The temperature distribution of the solid breeding material in TBM has been estimated with taking account of nuclear heating to be in the range from 573 K to 1173 K [4]. Although it is desired for the tritium to be recovered completely in whole region of blanket during ITER operation, a small fraction of the tritium remains in low temperature region [5]. Therefore, in order to estimate the tritium inventory in Li_2TiO_3 pebbles in the blanket of ITER, the retention and desorption behavior of the tritium has to be investigated.

In the present study, the deuterium ion irradiation experiment was conducted for in Li_2TiO_3 pebbles to simulate the tritium retention and desorption behavior. The pebbles were irradiated by deuterium ions with energy of 1.7 keV at various irradiation temperatures (RT, 473 K, 573 K, 673 K, 773 K), and after that the retention and desorption behavior of retained deuterium was investigated by using a technique of thermal desorption spectroscopy (TDS). Based on the obtained results, the tritium inventory in the TBM during ITER operation was estimated.

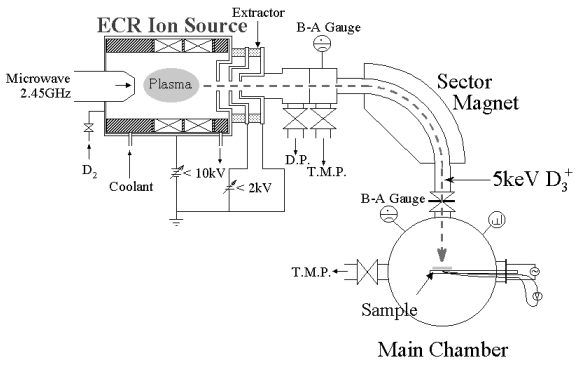

Fig.1 ECR ion source apparatus.

2. Experiments

18 Li_2TiO_3 pebbles (about 2 mmφ) [6] were used for the deuterium ion irradiation. These pebbles were heated at 973 K for an hour in a vacuum chamber to remove

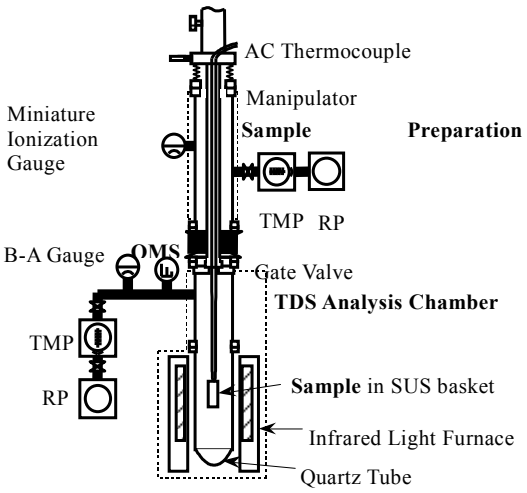

Fig. 2 TDS apparatus.

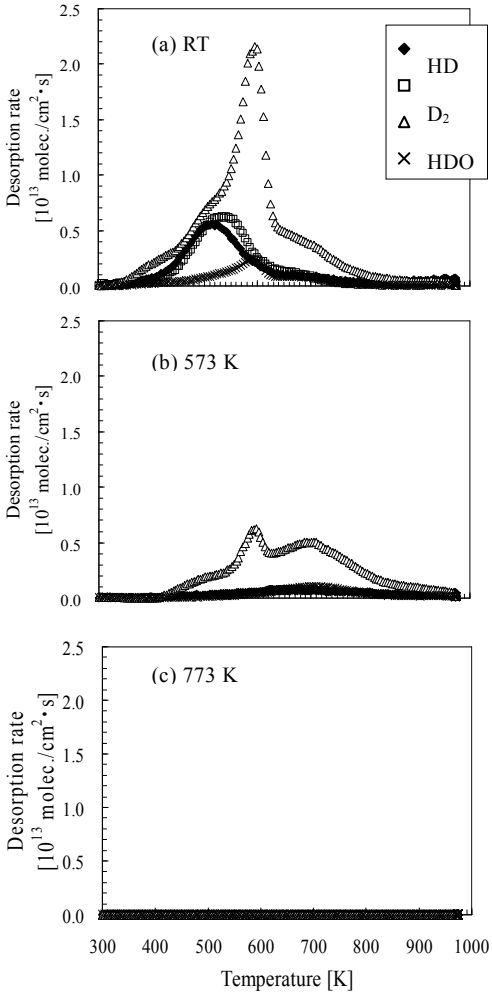

Fig.3 Thermal desorption spectra of gases containing deuterium for deuterium ion irradiated Li_2TiO_3 pebbles at the irradiation temperatures of (a)RT, (b)573 K and

impurities, such as hydroxides and carbon oxides [6]. After the heating, the pebbles were installed to a sample holder in an electron cyclotron resonance (ECR) ion source (Fig.1) and irradiated by deuterium ions. The sample holder made of Ta plate and Mo mesh was used to fix these pebbles and heat by indirect resistive heating. The irradiation temperature (surface temperature of the pebbles) was changed from RT to 773 K. The surface temperature was estimated from the temperature of the sample holder measured by a thermocouple. The temperature difference between the surface of the pebble and the sample holder was approximately 100 K - 200 K at each irradiation temperature. The deuterium ion energy was 1.7 keV, the fluence was 5×10^{18} D/cm^2 and the flux was approximately 9×10^{14} D/cm^2·s. After the ion irradiation, the pebbles were transferred to the TDS chamber (Fig.2). Then the sample was heated by an infrared light furnace from RT to 973 K with a heating rate of 10 K/min. At 973 K, the heating was conducted for an hour. The ultimate pressure before the TDS analysis was approximately 10^{-8} Pa.

3. Results

Figure 3 shows the thermal desorption spectra of gases containing the deuterium in the deuterium-irradiated Li_2TiO_3 pebbles with the irradiation temperatures of (a)RT, (b)573 K and (c)773 K. Deuterium retained in these pebbles desorbed in forms of HD, D_2, HDO and D_2O. In our previous study, the deuterium desorption behavior of the Li_2TiO_3 pebbles was similar with that of the Li film, therefore most of retained deuterium is trapped in forms of Li-D and Li-O-D [5]. Desorption rates of these gases decreased with increase of the irradiation temperature. At the irradiation temperature of 773 K, the retained deuterium completely desorbed during the irradiation. This result suggests that the tritium produced in Li_2TiO_3 pebbles at the temperature higher than 773 K completely desorbs during the ITER

operation.

Figure 4 shows the amounts of gases containing the deuterium and total amount of deuterium desorbed from the pebbles as a function of the irradiation temperature. In the cases of HD and D_2, the amounts of desorbed gases decreased with increase of the irradiation temperature. On the other hand, in the cases of HDO and D_2O, the amounts of desorbed gases increased with the irradiation temperature in the range lower than 473 K and then decreased in the range higher than 473 K. This difference in the irradiation temperature dependence of the desorption amount occurs due to the different desorption peak temperatures of these gases. The amount of deuterium desorbed in form of HDO was largest in these gases at every irradiation temperature. The total amount of retained deuterium was almost the same in the temperature range lower than 473 K, while the total amount decreased sharply with increase of the irradiation temperature in the range higher than 473 K.

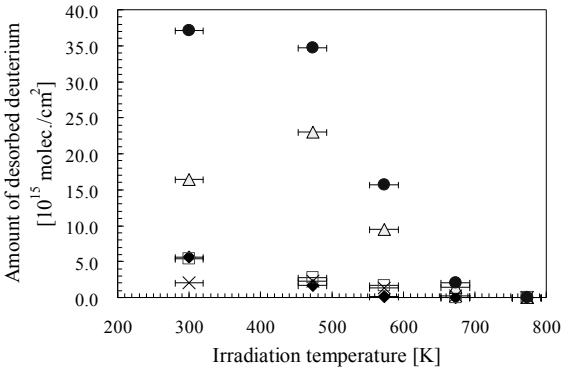

Fig.4 Amounts of gases containing deuterium desorbed from Li_2TiO_3 pebbles as a function

Figure 5 shows the amount of retained deuterium (total amount of retained deuterium). The dashed lines in Fig. 5 show the temperature range of Li_2TiO_3 breeder in TBM. The retained deuterium completely desorbes in the region with temperature higher than 773 K, while a small fraction of the deuterium is retained in the region with temperature lower than 773 K. In the TBM, the region with temperature lower than 773 K exists. The amount of retained tritium in this region determines the tritium inventory. Namely, the tritium is retained in the region with temperature of 573-773 K (shown as dot region in Fig.5).

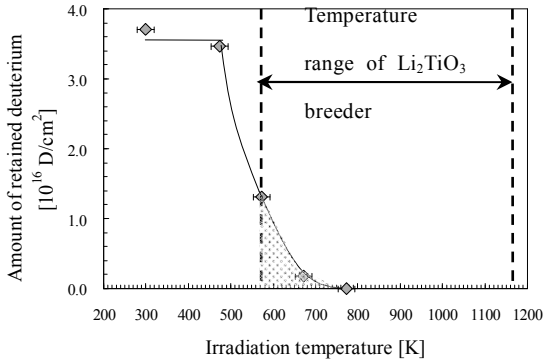

Fig. 5 Amounts of retained deuterium in Li_2TiO_3 pebbles as a function of irradiation temperature.

The amount of retained tritium in the TBM can be estimated using the present result. For Li_2TiO_3 pebbles, provided that the deuterium is trapped only by Li, the deuterium concentration in the atomic ratio of D/Li at RT is approximately 0.5 [5]. In the case of TMB, the amount of lithium is approximately 7 kg [8]. Lithium burn-up of Li_2TiO_3 pebbles during ITER operation is estimated as about 0.32 % [7], and thus the reduction of lithium in these pebbles by neutron irradiation is negligible. In this case, the maximum tritium inventory is estimated as 1.5 kg if the temperature in the TBM is RT. In addition, the ratio of the region with temperature lower than 773 K in TBM is estimated as ~0.1 [8]. From the results obtained in the present study, the amount of tritium retained in the region at 573-773 K could be estimated as approximately 2 % of the amount at RT. Under the assumption that the tritium trapped in the region above 773 K is completely desorbed during the ITER operation, the tritium inventory in the TBM during the operation becomes approximately 12 g. This estimation suggests that the tritium inventory of the TBM is only a few grams. The tritium inventory can be reduced if the region with temperature lower than 773 K is easily reduced by the design.

4. Conclusion

In the present study, Li_2TiO_3 pebbles was irradiated by deuterium ions under various deuterium ion irradiation temperatures (RT, 473 K, 573 K, 673 K, 773 K), and the retention and desorption behavior of deuterium was investigated using a technique of thermal desorption spectroscopy. The amount of retained deuterium for Li_2TiO_3 pebbles was almost the same in the irradiation temperature range lower than 473 K, while the amount decreased sharply with increase of the irradiation temperature in the range higher than 773 K. The amount of retained deuterium became approximately zero at 773 K. The temperature distribution of the solid breeding material in TBM is in the range from 573 K to 1173 K. The present results suggest that the tritium inventory of the blanket is only a few grams. If the region with temperature lower than 773 K is reduced by the design work, the tritium inventory furthermore decreases.

Acknowledgements

This work was supported by the Grant-in-Aid for Scientific Research from the Ministry of Education, Science, Sports and Culture in Japan, and partly supported by the JAEA Collaboration Research Program. This work was partly supported by the JSPS-CAS Core University Program in the field of Plasma and Nuclear Fusion.

References

[1]A. Ying *et al*., J. Nucl. Mater. **367-370,** 1281-1286, (2007).
[2]Japan Atomic Agency Report, JAERI-Review 2005-011, 2005
[3]N. Roux *et al*., J. Nucl. Mater. **233-237,** 1431-1435, (1996).
[4]S. Tanaka *et al*., J. Plasma Fusion Res. **81,** 434-450, (2005)
[5]T. Hino *et al*., ''Deuterium Retention and Desorption Behavior of Lithium Titanate'', 8th International Symposium on Fusion Nuclear Technology (ISFNT-8), Heidelberg, Germany, (2007).
[6]K. Tsuchiya *et al*., J. Nucl. Mater. **258-263,** 1985-1990, (1998).
[7]M. Enoeda, ''Development of blanket materials in JAEA'', 2nd roadmap meeting for development of fusion reactor, fast track cluster of Fusion Forum, Tokyo, (2006).
[8]T. Hino *et al*., ''Deuterium Retention and Desorption Behavior of Lithium Titanate'', Advanced Blanket Meeting at National Institute of Fusion science (NIFS), July 1, (2008).

Design of Performance Testing System of Superconducting Strand Sample

Qian Jing[1] Weng Peide[1] Luo Jiarong[2] Wu Yu[1]
1 Institute of Plasma Physics, Chinese Academy of Sciences, Hefei, 230031, China
2 Department of Modern Physics, Shanghai Donghua University, Shanghai
E-mail of corresponding author: jing@ipp.ac.cn

Abstract:

Critical current is an important property of superconducting magnets, as well as the effect of temperature and magnetic field on the superconducting properties should be studied. The superconducting strand properties have close link with the performance of the coils in operation.

In this paper a set of automatic testing system based on PC is introduced, which is designed for critical performance testing of ITER superconducting Nb_3Sn strand samples. To measure critical current of superconducting strand, the background field is supplied by a magnet which is a high field superconducting magnet designed to produce fields up to 16 Tesla, and the direction of the magnetic field is vertical to the sample. Temperature in the testing dewar is automatically adjusted by a PID controller. And the temperature of strand sample can be controlled by regulating the vacuum valve.

To meet the testing criteria the testing system is developed to acquire real-time and high accuracy data. Sensors with high accuracy and anti-magnetic capacity are selected and installed cautiously. Signal lines are wired normatively. Keithley programmable meters, communication cards and data acquisition card with good performance are included in hardware system. The software is programmed with Visual C++ 6.0 computer language, meanwhile, the Microsoft Access database and SCPI (Standard Command for Programmable Instrument) language are integrated in the software. Several methods have been used in order to show lab assistants experimental process clearly and timely.

How to operate right and exclude complicated field noise is listed and error in experimental data is also calculated accurately. Measurement precision lower than 1uV is obtained despite kinds of noise interference. It proves to be a reliable system to meet the demands of ITER through experiments.

Keywords: Critical Current，Automatic test, Error sources

1. Introduction

Performance testing of Nb_3Sn and NbTi superconducting sample is in progress at the institute for ITER Project. Critical current is not only one of the main parameters which characterize performance of

superconducting materials in applied engineering technology, but one of important parameters tokened superconductivity. As for cryogenic superconductors critical current is a function of temperature and magnetic field.

Methods to measure critical current are mature. Direct current four-lane law is used in the test of ITER superconducting strand sample. The direction of the background magnetic field is vertical to the sample

and the value of magnetic intensity is varied. Current through the sample rises slowly from 0 until it is quenched. Standard criterion of superconductor quenching is 0.1 μ V/cm electric field. So the voltage Vs between the 50 cm length's sample is about 5uV with corresponding critical current. The influence of self field caused by the sample is small enough to be ignored on the critical current.

The testing equipments of ITER superconducting strand sample mainly involves:

A superconducting solenoid magnet can produce testing background fields up to 16 Tesla, whose bore diameter is Φ70 mm and which is 355mm in high.

An experimental liquid helium Dewar device with changeable temperature is 1400mm in high and 650mm of bore diameter.

A PID temperature controller is used to control temperature in the Dewar and keep temperature constant when measuring voltage and current.

Sample poles; New-style superconducting current lead and its bracket. Quench protecting device;

A DC constant current source can output 600A with power of 3KW. Hall current sensor;

And a set of self-development automatic testing system etc.

Fig 1 indicates the automatic testing system principle figure.

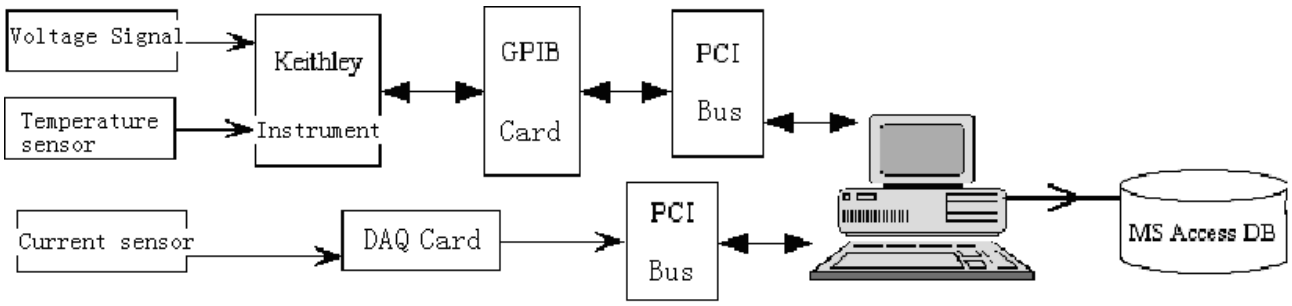

Fig 1 Automatic Testing System Principle Figure

2. Experiments

To achieve high repeatability for superconducting strand performance test, testing job should be carried out by PC. There are four main physical parameters to be gathered and stored. Temperature measuring precision have to be no less than 10mK, current measuring precision no less than 1A, voltage measuring precision no less than 10nV. Meanwhile data acquisition frequency is no less than 10Hz. All the real time data should be shown directly in order that lab assistants can monitor the progress.

According to testing requirements, hardware is selected carefully. Cernox1050 has high capacity of sensitivity, repeatability and stability under cryogenic and magnetic conditions, which is selected as the temperature sensor in the testing. Calibration precision is about 1mK in the range of 3.5K and 300K. Keithley2700 is a $6\frac{1}{2}$ digital multimeter which can be controlled by PC through GPIB. When its DC voltage input range is 100mV, measurement precision can reach 0.1uV. Then temperature measurement precision is 0.1mK in liquid Helium temperature zone and 10mK in liquid Nitrogen temperature zone. With 16-bit general purpose analog input channels the ADLINK PCI-9114HG data acquisition card has sensitivity of 15uV/V. Current resolution is no more than 30 mA.

Keithley2182 is a $7\frac{1}{2}$ digital nanometer with good performance. It can distinguish 1nV when its input voltage range is 10mV. Voltage between 50 cm long superconducting strand sample is gathered with Keithley2182. Industrial computers control the automatic system by GPIB and Keithley instruments. In addition experimental data are stored and shown in the PCs.

Testing program is designed with modularized thinking. Program module diagram and data flow chart is as figure 2. As the sampling rate is 14Hz, automatic testing circle is realized by the usage of window operation system timer. The method can satisfy the testing requirements and simplify program design.

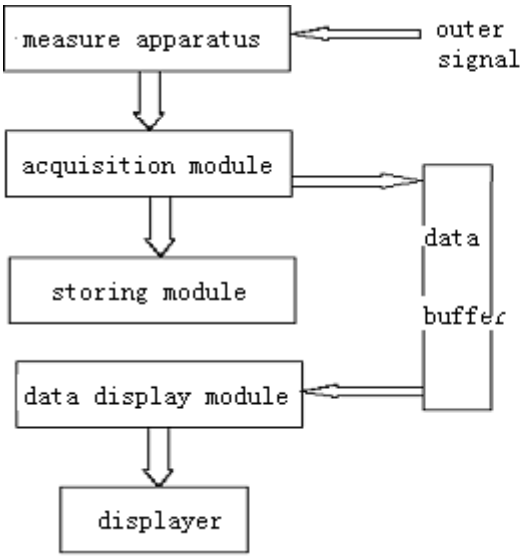

Fig 2 Program Modual Figure

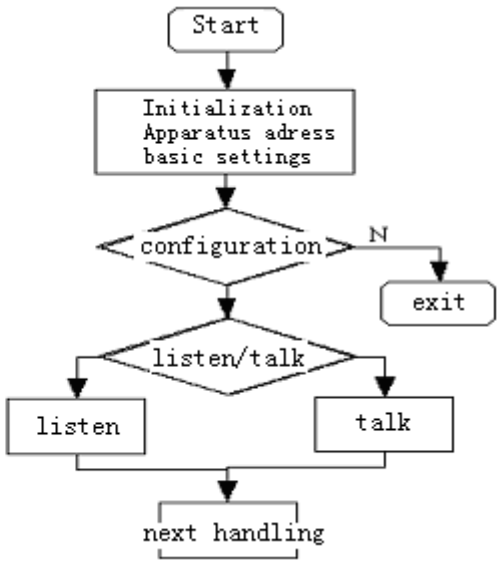

Fig 3 Control Flow Chart

Industrial computer operating system is Win2K. Testing software is programmed in Visual C++6.0 to gather useful signals, display and save data. SCPI commands are called in VC++6.0 to control functions of Keithley instruments through GPIB communication card. SCPI(Standard Command for Program Instrument) built on IEEE-488. 2 standard define a group of normal commands for instruments supporting SCPI. Thus efficiency of

program design and development is greatly improved with SCPI. For example, following two commands are enough to make instrument measure DC voltage signal and adjust measure range automatically.

"sens:FUNCtion 'VOLTage:DC"

":sens:volt:rang:auto on"

Interface program coded with IEEE-488 library functions can monitor Keithley instruments remotely. Control flow chart is as shown in figure 3. Frequently used interface functions are as follows:

initialize(addr, level);

send(addr, s, status);

Data gathered in every test are stored timely in MS ACCESS2K database for the purpose of off-line analysis. Each table title is named by starting time of the test. There are several main data fields in the table: ID of numeric type, current acquisition time, and parameters of text type including current through sample, voltage of 50cm long strand , temperatures in the upper and lower parts of the sample. In the program curve and table forms are adopted for a friendly human-machine interface to express experimental data.

3. Results

Figure 4 is the graph painted with experimental data. Physical lab assistants can get other critical properties of superconducting wire such as critical current density, n value with experimental data.

Proceedings below are considered in the experiments to assure accuracy of the data.

1. Devices should be warmed up at least three hours before experiment.

2. Remove background noise by software;

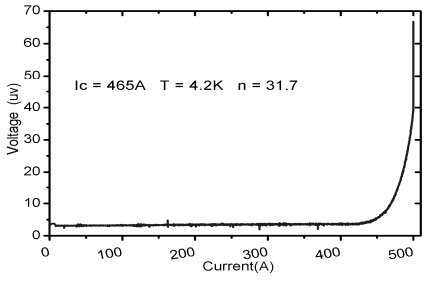

Fig 4 Experimental Data Curve

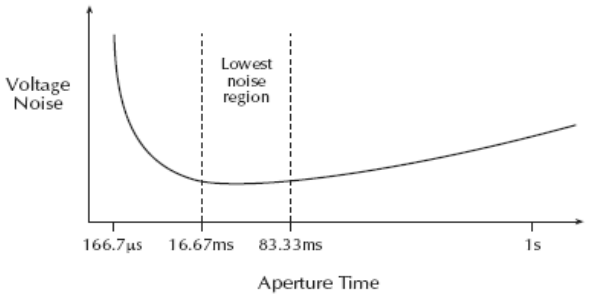

Fig 5 Speed vs. noise characteristics

3. There exists certain restriction between measure precision and speed of keithley instrument, as is shown in figure 5. Integrated situations should be considered when to select most appropriate NPLC value and whether to use analog filter function or digital filter function.

4. All the devices must have fine capability of anti electromagnetic interference under electromagnetic noise circumstance. Twisted pair in smallest torque and shielded twisted pair with metal net are used as measuring signal lines.

5. Installation of Cernox sensors is of most importance in the test. Wrong installation will lead to big errors between the measuring value and real value. And it will ruin the test if temperatures of upper and lower parts of

the sample does not accord with each other.

In the design process of the testing experiment reasonable testing principle and methods are adopted. In the experiment process, tenets of cryogenic physics are followed. The main error sources lies in:

1. digital voltage meter measuring voltage of the sample
2. devices to measure current through the sample, including accuracy and stability of current source, current sensor and data acquisition card.

According to error sources listed above, steps to reduce error are as follows:

Calibrate instruments such as keithley digital meter, data acquisition card and constant current timely. Besides kinds of anti-interference measurements filter components are needed to filter out impurities in useful signals.

4. Summary

In the present performance experiments of superconducting strand sample, measure precision is 3% of critical current. The test system can meet the criteria of ITER Project. In conclusion the automatic system is an important support and improves the efficiency of the experiments.

Acknowledgements

The authors would like to acknowledge all the people, who have contributed to the experiments for their effort and encouragement. This work was partly supported by the JSPS-CAS Core University Program in the field of Plasma and Nuclear Fusion.

References

[1] Chen Zhuomin, Qian Jing, and etc. Technical diagnosis system for superconducting Tokamak EAST, Cryogenics and Superconductivity, 35(2006)1-4

[2] Model 2700 Multimeters/Switch System User's Manual Keithley Instruments, Inc.

[3] Model 2182/2182A Nanovoltmeter User's Manual(Rev.A / June 2004) Keithley Instruments, Inc.

[4] IEEE Std 488. 221992. IEEE Standard codes , Formats , Protocols and common commands for Use with IEEE std 488. 1 -19875 Jace Curti. National instruments, http://www.eetchina.com, 2002-12

Hydrogen isotope behavior in damaged tungsten by high energy ion beam

M. Fukumoto[1], Y. Ueda[1], Y. Ohtsuka[1], M. Taniguchi[2], T. Inoue[2], K. Sakamoto[2],
J. Yagyu[2], T. Arai[2], I. Takagi[3], and N. Yoshida[4]

1 Graduate School of Engineering, Osaka University, Osaka, Japan
2 Japan Atomic Energy Agency, Ibaraki, Japan
3 Department of Nuclear Engineering, Kyoto University, , Kyoto, Japan
4 Interdisciplinary Graduate School of Engineering Science, Kyushu University, Fukuoka, Japan
E-mail of corresponding author: yueda@eei.eng.osaka-u.ac.jp (Y. Ueda)

Abstract

Effects of radiation damage on deuterium trapping in tungsten were investigated using SIMS/NRA and TDS techniques. Radiation damage of ~4.8 dpa was produced by 300 keV hydrogen ions, then deuterium ions were implanted at 473 K to fluences of (0.5–8.0) × 10^{24} D^+/m^2. Deuterium concentration at ~0.1 μm deep became saturated even at the lowest fluences (~5.0 × 10^{23} D^+/m^2), while the D retention at ~1.0 μm deep did not become saturated even at the highest fluences of ~8.0 × 10^{24} D^+/m^2. TDS spectra suggested that the implanted D was trapped at the radiation-induced defects which were related to the desorption peaks at ~770 and ~920 K

Keywords: Tungsten, Radiation damage, Deuterium retention, Trapping site, ITER

1. Introduction

Tungsten-based materials are leading candidates for next generation fusion devices. The advantages of tungsten are its natures of high melting temperature and low sputtering yield by fuel particles. In ITER, tungsten will be used at the baffle plates and the domes of diverter regions. Extensive studies have been made on the behavior of hydrogen isotopes in various tungsten materials[1]. In DT fusion reactors radiation induced defects are produced in tungsten due to the 14 MeV neutron bombardment. Therefore, it is important to study the tritium behavior in neutron-damaged tungsten.

The purpose of this work is to investigate the deuterium behavior such as retention and depth distributions in tungsten damaged by high-energy ions. Deuterium depth distributions of the damaged samples were measured with SIMS (Secondary Ion Mass Spectrometry) and NRA (Nuclear Reaction Analysis). Deuterium retention was observed by TDS. Experimental results were compared with those of the TMAP7 simulations [2].

2. Experimental

The polycrystalline W sheets, 1 mm thick and 99.99 at% pure (A.L.M.T.Corp.), were used. These were powder metallurgy and hot rolled products. In the manufacturing process, the W sheets were annealed at 1173 K for 0.5 h in a hydrogen atmosphere to relieve internal stresses. Tungsten samples, ~10 × 10 mm^2, were mechanically polished less than ~0.1 μm roughness.

Radiation damage was produced using a 1 MeV accelerator MTF [3]. Negative ions of 300 keV H^- were used for damage creation. The sample temperature was kept below 473 K in order to simulate wall conditions in ITER except for high heat flux regions. Following damage creation, D^+ implantation was performed using an ion beam irradiation device HiFIT [4]. Incident ion spices were D^+, D_2^+, and D_3^+ with the energies of 1.0 keV. The deuterium atom species ratios were 50 %, 30 %, and 20 % for 0.3 keV, 0.5 keV, and 1.0 keV D, respectively. Typical flux densities were ~1.5 × 10^{20} D^+/m^2s. Irradiated fluence was from 0.5 × 10^{24} to 8.0 × 10^{24} D^+/m^2. Sample temperature was kept at 473 K, which was measured by a thermocouple.

SIMS analysis was performed to measure deuterium depth profiles before TDS. The SIMS analysis did not significantly affect the subsequent TDS measurement since the size of sputtered spot (~0.1 mm^2) was much smaller than the D implanted area (~19.6 mm^2). NRA (Nuclear Reaction Analysis) measurement was used to absolutely calibrate the SIMS signal. For TDS measurements, the samples were heated from 300 to 1100K at a heating rate of ~1 K/s and released D^2 was monitored using a quadruple mass spectrometer (QMS). The QMS signals were calibrated by a standard He leak bottle by collecting relative ionization efficiency before each TDS measurement.

3. Results and Discussions

In the case of the damaged samples, deuterium concentration was higher than that of the undamaged sample within the damaged zone. The fluence dependence of D distributions for the ~4.8 dpa damaged samples at 473 K is shown in Fig. 1. The fluence used in the TRIM code simulations [5] was ~1.5 × 10^{22} H^-/m^2. For the fluences of more than 5.0 × 10^{23} D^+/m^2, D concentration near the sample surface (~0.1 μm in depth) became saturated as ~0.9 × 10^{27} D/m^3. On the other hand, no saturation occurred even at the fluence of 8.0 × 10^{24} D^+/m^2 around the depth of 1 μm. If the D concentrations were equal to

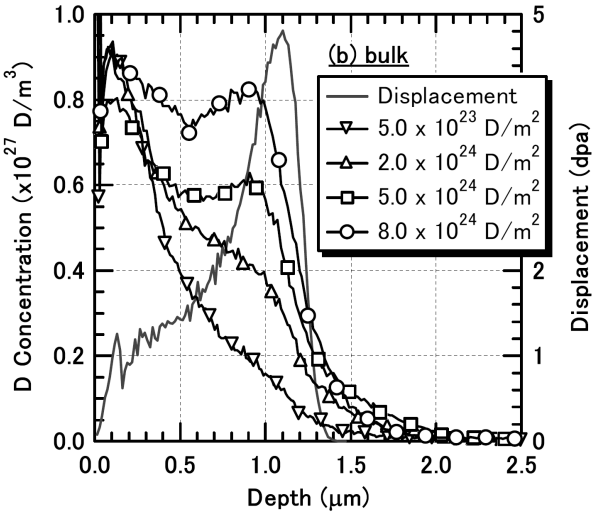

Fig. 1. SIMS depth profiles for ~4.8 dpa damaged samples as a function of incident fluence. Samples were irradiated with 1 keV deuterium ions at 473 K.

the trap densities at the ~0.1 μm in depth, the total trap densities are estimated to be ~0.014 traps/W for the radiation damage ~1.0 dpa and the implant temperature 473 K.

Thermal desorption spectra were obtained for the ~4.8 dpa damaged samples in the fluence of 0.5-8.0 × 10^{24} D^+/m^2 at 473 K. For comparison, one undamaged sample irradiated to 5.0 × 10^{24} D^+/m^2 at 473 K was also observed. Figure 2 shows the TDS spectra for the ~4.8 dpa samples with the fluences of 5.0 × 10^{24} D^+/m^2. It was found that this TDS spectra consisted of the three Gaussian peaks with the peak positions of ~770 K, ~860 K, and ~920 K. In this paper, these peaks are named with Peak 1, Peak 2, and Peak 3, respectively.

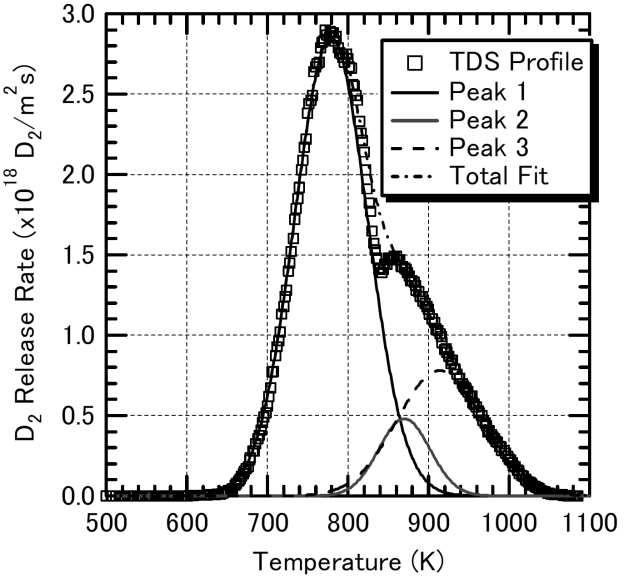

Fig. 2. TDS spectra obtained from the ~4.8 dpa (~1.5 x 10^{22} H^-/m^2) damaged samples irradiated to 5.0 x 10^{24} D^+/m^2 at 473 K.

The fluence dependence of D retention for the three peaks is shown in Fig. 3. For the damaged samples with the fluences of 5.0 × 10^{24} D^+/m^2, the D retention in the Peak 1 was about one order of magnitude larger than that of the undamaged sample. Furthermore, the D retention in the Peak 1 was increased with the D fluences. The D retention in the Peak 2 was almost constant regardless of the fluences. The D retention in the Peak 3 was only observed from the damaged samples and was also increased with the D fluences. Therefore, it is suggested from Fig. 4 that implanted D would be trapped at the radiation induced defects which related to the desorption peak at ~770 K (Peak 1). In addition, another radiation induced trap with the desorption peak at ~920 K (Peak 3) was also observed.

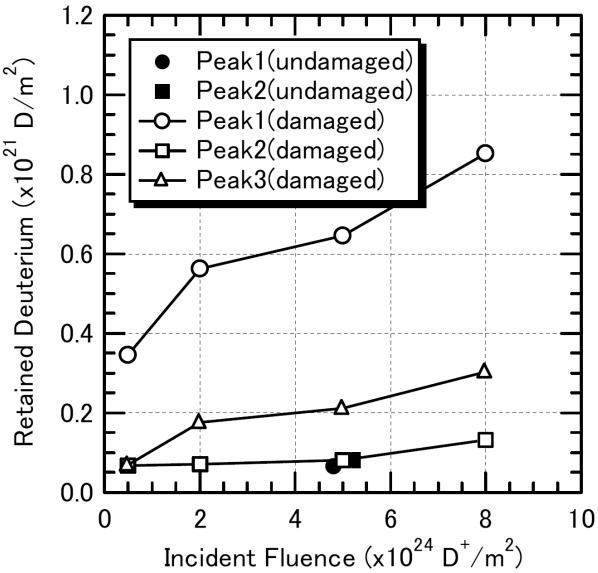

Fig. 3 D retention of each desorption peak as a function of incident fluence obtained from ~4.8 dpa (~1.5 x 10^{22} H^-/m^2) damaged samples. All samples were irradiated with the 1 keV deuterium ions at 473 K.

Poon et al. have reported that TDS profiles obtained from single crystal tungsten irradiated at 300 K show desorption peaks at 520 and 642 K [19]. These peaks are considered to be due to desorption of trapped D at single vacancies. The peak temperature of

the Peak 1 (~770 K) was higher than the results obtained by Poon et al. [19]. Therefore, it can be considered that the Peak 1 would not be related to single vacancies. Deuterium desorption spectra of 10 keV H^+ damaged W exposed with 100 eV D plasma at 500 K was obtained by Arkhipov et al. [12]. They reported that the D desorption around 750-800 K was due to vacancy clusters formed by the 10 keV H^+ pre-irradiation. The peak temperature of the Peak 3 (~920 K) was similar to that observed by Poon et al. (~900 K) [19] which are considered to be due to desorption from voids.

4. Summary

SIMS analysis showed that D retention in the damaged sample was increased with the deuterium fluences within the radiation-damaged zone. Quantitative analysis using the SIMS/NRA technique showed that D concentration became saturated with ~0.9×10^{27} D/m^3 for the ~1.0 dpa damaged region (~0.1 μm in depth) at the fluences of less than~5.0×10^{23} D^+/m^2. On the other hand, D concentration at the ~1.0 μm deep did not become saturated even at the fluences of ~8.0×10^{24} D^+/m^2. TDS spectra obtained from the ~4.8 dap damaged samples had three desorption peaks at ~770 K, ~860 K, and ~920 K. D retention associated with the ~770 K peak was increased with the D^+ fluences, while that with the ~860 K peak was constant for the all fluences. The ~920 K peak appeared only for the damaged samples and was also increased with the D^+ fluences.

Acknowledgements

This work was partly supported by the JSPS-CAS Core University Program in the field of Plasma and Nuclear Fusion.

References

[1] R. Causey, J. Nucl. Mater. 300 (2002) 91–117.

[2] G.R. Longhurst, TMAP7: Tritium Migration Analysis Program, User Manual, Idaho National Laboratory, INEEL/EXT-04-02352 (2004).

[3] T. Inoue, M. Taniguchi, T. Morishita, M. Dairaku, M. Hanada,T. Imai, M. Kashiwagi, K. Sakamoto, T. Seki, K. Watanabe, Nucl. Fusion 45 (2005) 790.

[4] Y. Ueda, T. Shimada, M. Nishikawa, Nucl. Fusion 44 (2004) 62.

[5] J.F. Ziegler, J.P. Biersack, and U. Littmark, The Stopping and Range of Ions in Solids (Pergamon, New York, 1985).

Mitigation of current quench by runaway electrons in LHCD discharges in the HT-7 Tokamak

H. W. Lu, L. Q. Hu, S. Y. Lin, G. Q. Zhong, and HT-7 team
Institute of Plasma Physics, China Academy of Sciences, Hefei 230030, P.R. China
E-mail of corresponding author: luhw@ipp.ac.cn

Abstract

Production of runaway electrons during a major disruption has been observed in HT-7 Tokamak. The runaway current plateaus, which can carry part of the pre-disruptive current, are observed in lower-hybrid current drive (LHCD) limiter discharges. It is found that the runaway current can mitigate the disruptions effectively. Detailed observations are presented on the runaway electrons generated following disruptions in the HT-7 tokamak with carbon limited discharges. The results indicate that the magnetic oscillations play an important role in the activity of runaway electrons in disruption.

Keywords: runaway electron, disruption, LHCD, magnetic oscillations

1. Introduction

One of the important problems of a tokamak fusion reactor is the possible damage caused by disruption generated runaway electrons [1], and the plasma facing components (PFC) would be damaged if the localized and intense irradiation of runaway electrons occurs [2]. The high electric fields induced during the current quench phase of a tokamak disruption can generate a large number of runaway electrons with energies as high as several tens of MeV [3]. Intense runaway electrons with high energies of several tens of MeV generated at a major disruption would significantly reduce the lifetime of the first wall. Plasma disruptions in a large tokamak such as ITER are one of the most serious issues for the design of the plasma-facing components, blanket and vacuum vessel [4]. In consequence, there is a great concern about the damage that these energetic runaway electrons might cause if they impact on the first wall structures, which might be critical for larger devices such as the ITER tokamak [5], and it is necessary to mitigate and avoid the current quench artificially. In spite of the fact that considerable progress has been made in recent experiments in the design and testing of the mitigation techniques based on massive gas jets and pellet injection (see[6,7]) the problem of runaway suppression is still considered to be one of the primary task for a reliable tokamak operation[8].

On the other hand, the post-disruption current plateau created by runaway electrons (I_{RE}) can mitigate the disruption effects. Experiments in many tokamaks such as JET [9], JT-60U [10], FTU [5], and TEXTOR [3], have testified the fact. This fact suggests that runaway electrons can be used to mitigate or avoid the current quench when the safe and reliable control of runaway electrons is available [2]. Standing on such a point of view, the experiment for avoiding the current quench by runaway electrons has been carried out. With the aid of the electron cyclotron emission (ECE), vertical multi-channel CdTe detectors (HXV), runaway electron diagnostics (RA), runaway

electrons have been detected at the very beginning of disruptions in the HT-7 tokamak. Detailed observations are presented on runaway electrons generated following disruptions in the HT-7 tokamak with carbon limited discharges.

2. Experimental set-up

The electron cyclotron emission (ECE), hard X-ray (HXR) emission and fast electron bremsstrahlung (FEB) have been used as the main tool to investigate the behavior of runaway electrons. There are 15 channels of heterodyne radiometer for ECE measurement in the HT-7 tokamak. It measures the ECE in the frequency range 95–124 GHz. Formation of nonthermal electrons during LHCD phase results in substantial enhancement of the downshifted ECE. The acceleration of fast electrons into energetic runaways will reduce the ECE signal since its downshifted frequency is out of the measuring frequency range. Thus, the ECE signal provides considerable information about the evolution of fast electron population and low energy runaway population [11]. The hard X-ray emission in the energy of 1.0-10.0MeV was detected by the NaI(TL) scintillator detectors arranged tangentially on the equatorial plane. It provides the considerable information on the HXR emission resulting from the thick target bremmstralung when runaway electrons are lost from the plasma and impinge on the vessel walls or plasma facing components. It provides information on loss and the energy content of the runaway electrons. It can only measure those runaway electrons that are no longer confined. The fast electron bremsstrahlung (FEB) in the energy of 30-250kev was measured by the vertical CdTe detector array arranged inside of the vessel. It provides considerable information on the LHW power deposition profile and the spatial and velocity distribution of the electrons accelerated via Landau damping by LHW [12]. Based on the above diagnostics systems, Phenomena of runaway electrons during disruptions of discharges in the HT-7 tokamak were presented as the following.

3. Current quench without runaway electrons

A typical LHCD discharge is shown in figure 1. The plasma current was 150kA, the line-averaged density $n_e=0.8\times10^{19}m^{-3}$; 200kW LH power was launched into the plasma from 0.244s to 0.318s. Strong MHD activity was observed from t=0.312s on. After the ECE signal drop the plasma current I_p dropped and the loop voltage V_{loop} increase took place also at about t=0.312s. Negative voltage spike and a small temporary increase of I_p were observed at the moment of disruption. At this moment huge visual bremsstrahlung emission bursts showed the impurities increase. So Z_{eff} increased because of the amount of impurities produced by the collision between electrons and PFC (plasma facing component). But very large magnetic perturbations lead to enhanced losses of fast particles and limit the energy and total amount of runaway electrons. So at the first moment of magnetic oscillations bursts, most of the runaway electrons lost from the background plasma and hit on PFC, and then the number of electrons inside of the plasma was reduced rapidly. So the current quenched rapidly after the disruption.

The time evolution of tangential hard X-ray emission in several energy ranges is

shown in figure 2. We can also see from figure 2 that the counts of hard X-ray emission in almost every energy ranges were negligible after the disruption. And the counts of high energy hard X-ray emission decayed even before the disruption.

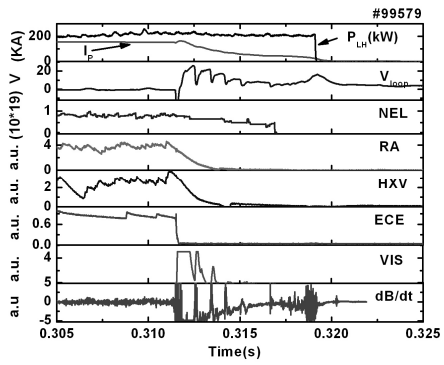

Fig.1 Time evolution of several plasma parameters during the disruption in the discharge No 99579.

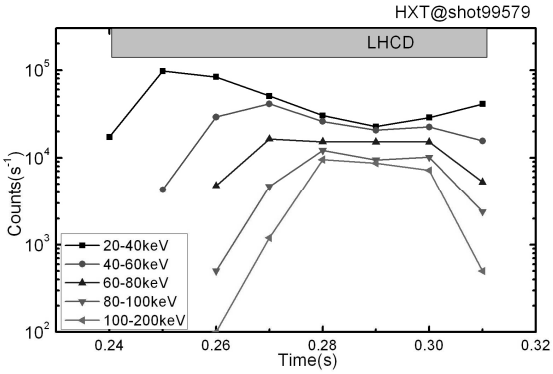

Fig.2 Time slice of tangential hard X-ray emission intensity (HXT) in several energy intervals for discharge No 99579.

4. Mitigation of current quench by runaway electrons

Fig.3. shows one of the dedicated discharges No 90821 which produced a long runaway electrons tail after the disruption. Diffusion losses at these toroidal field and plasma current (2T and 130kA, respectively) do not seem to play a significant role in the removal of electrons from the runaway electron beam inside the background plasma. From figure 3 we can see that the disruption happened at 1.067s. Magnetic oscillations bursts only at the moment of disruptions, and it disappeared immediately when the disruption finished. So after the ECE signal dropped ramp-up was present because of the acceleration of low hybrid wave to electrons. The HXV signal and RA signal increased progressively after the magnetic oscillations bursts.

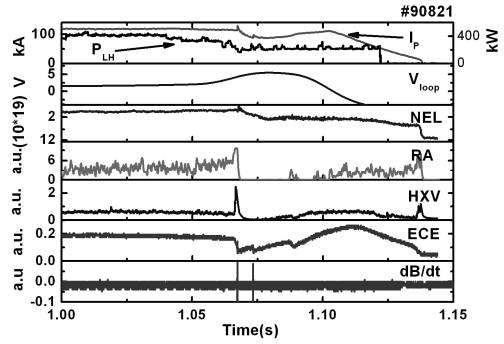

Fig.3 Time evolution of several plasma parameters during the disruption in the discharge No 90821.

We can also see from figure 4 and figure 5 that the counts of every energy ranges of HXT and HXV were reduced at the moment of disruption, but built up as soon as the magnetic oscillations disappeared. The reason is that after the happening of disruption, the magnetic oscillations disappeared rapidly, and large number of electrons still remained inside of the background plasma; and also, the low hybrid wave can accelerate the electrons effectively. So the runaway electrons rebuilt up again after the happening of disruption. And the plasma current decays slower than the shot 99579 with the aid of runaway electrons. The runaway electron current can replace the plasma current with a small I_p drop at the moment of disruption by application of LHCD.

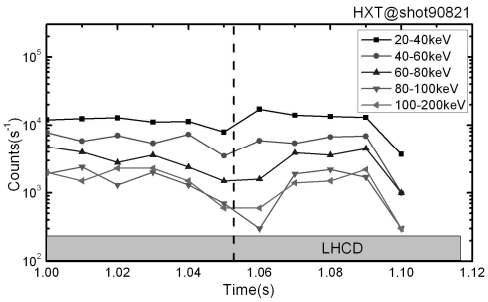

Fig.4 Time slice of tangential hard X-ray emission intensity (HXT) in several energy intervals for discharge No 90821.

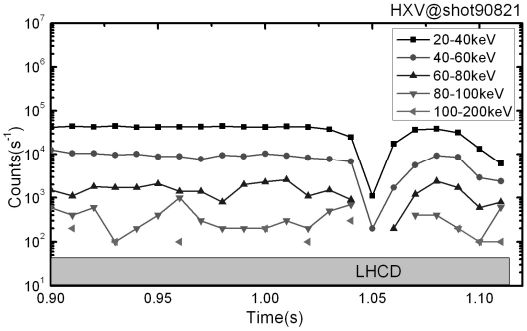

Fig.5 Time slice of vertical hard X-ray emission intensity (HXV) in several energy intervals for discharge No 90821.

5. Conclusions

In this article, we summarize runaway electron behaviors in the disruptions of LHCD discharges in HT-7 tokamak. It is found that the runaway electrons in LHCD plasmas can mitigate the current quench effectively. But it depends on the degree of magnetic oscillations after the disruptions. In the circumstance of hard magnetic oscillations, the runaway electrons lost from the background plasmas and hit on PFC, and then the number of electrons inside of the plasma was reduced rapidly. So the current quenched rapidly after the disruption. But if magnetic oscillations bursts only at the moment of disruptions, and it disappeared immediately when the disruption finished, the runaway electrons will rebuilt up again after the happening of disruption. So the runaway electrons can mitigate the current quench of LHCD plasmas.

Acknowledgements

This work has been supported by the National Nature Science Foundation of China, No.10675124, and partially supported by JSPS-CAS Core -University Program in the field of "Plasma and Nuclear Fusion".

References

[1] R.Jaspers, I.M.Pankratov, K.H.Finken, et al, study of disruption generated runaway electrons in TEXTOR-94

[2] Y.Kawano, T. Nakano, A. Isayama, et al, 32nd EPS Conference on Plasma Phys. Tarragona, 27 June - 1 July 2005 ECA Vol.29C, P-2.068 (2005)

[3] R. Jaspers et al., Nucl. Fusion **36**, 367 (1996).

[4] R. Yoshino, 2000 Nuclear Fusion **40**, 1293.

[5] J. R. Martı´n-Solı´s, B. Esposito, R. Sa´nchez, et al., PRL **97**,165002 (2006)

[6] ITER Physics Expert Group on Disruptions, Plasma Control and MHD, ITER Physics Basis 1999 Nucl. Fusion **39** 2251

[7] Plyusnin V V et al 2006 Nucl. Fusion **46** 277

[8] P V Savrukhin, Plasma Phys. Control. Fusion **48** (2006) B201–B210

[9]R.D.Gill, B.Alper, M.de Baar, et al, 2002 Nucl. Fusion **42** 1039

[10]R.Yoshino, S.Tokuda, Y. Kawano, et al, 1999 Nucl. Fusion **39** 151

[11]Z Y Chen et al Plasma Phys. Control. Fusion **50** (2008)015001 (10pp)

[12] Brusati M et al 1994 Nucl. Fusion **34** 23

Tritium Treatment in the Exhaust Gas on LHD Deuterium Experiments

K. Nishimura, Y. Asakura, M. Tanaka and T. Kawano

National Institute for Fusion Science, Toki-shi, Gifu-ken 509-5292, Japan

E-mail of corresponding author : nishimura.kiyohiko@LHD.nifs.ac.jp

Abstract

Present experiments in LHD are carried out using hydrogen or helium gas, and obtained the remarkable parameters. Now we are proposing next experimental campaign using deuterium gas. However, deuterium experiments are accompanied by the production of neutron and tritium. We must reduce the tritium release amount in the environment less than 3.7 GBq (0.1 Ci) in a year according to the local engagement. To ensure this regulation, two type of tritium removing systems are planed for installation. One is combination of a catalytic oxidation and a molecular sieve for vacuum pumping gas. The other is combination of a catalytic oxidation and a membrane dehumidifier, which has been developed in NIFS, for large amount of vacuum vessel purge gas treatment system. In addition to these, a high sensitivity tritium gas detector for online tritium monitor has been developed using a proton-conducting ceramic (or oxide) as a hydrogen isotope pump. The pumped tritium is condensed until the detectable concentration with a monitoring interval. This report describes two tritium removing systems and a high sensitive tritium monitor.

1. Introduction

The Large Helical Device (LHD) [1-4] is the largest superconducting heliotron type device with continuous helical coils (poloidal multi-polarity l=2 and toroidal field periods m=10) and three pairs of poloidal coils. Its major and minor radii of the plasma are 3.5-3.9 m and 0.6-0.65 m, respectively. The maximum magnetic field strength is about 3 T at the magnetic axis. The LHD project is aimed at exploring the feasibility of helical plasmas for fusion applications. In particular, it aims to demonstrate the steady-state currentless plasmas confined in the helical fields generated by super-conducting coils.

Present experiments are carried out using hydrogen or helium gases and achieved plasma parameters are T_e = 10 keV with $\langle n_e \rangle = 5 \times 10^{18} m^{-3}$, T_i = 13.5 keV with $\langle n_e \rangle = 3 \times 10^{18} m^{-3}$, $\langle \beta \rangle$ = 5.0 % at 0.425 T, 3268 sec. duration with 490 kW heating input, and fusion triple product = 4.4×10^{19} keVm^{-3}s. Now we are proposing next experimental campaign using deuterium gas. It is expected to improve plasma performance by a factor of 1.5-2 compare with hydrogen experiments. However, deuterium experiments are accompanied by the production of neutron and tritium. We must reduce the tritium release amount in the environment less than

3.7 GBq (0.1 Ci) in a year according to the local engagement.

To ensure this reduction, two type of tritium removing systems are planed for installation. One is combination of a catalytic oxidation and a molecular sieve for vacuum pumping gas. The other is combination of a catalytic oxidation and a membrane dehumidifier, which has been developed in NIFS, for large amount of vacuum vessel purge gas treatment system. In addition to these, a high sensitivity tritium gas detector for online tritium monitor has been developed. This tritium monitor can detect the tritium concentration of $5x10^{-4}$ Bq/cm^3. To realize such high sensitivity, a proton-conducting ceramic (or oxide) is used as a hydrogen isotope pump. The pumped tritium is condensed until the detectable concentration with a monitoring interval (~10 min.).

2. Tritium Removing Systems

In the LHD, two types of tritium removing systems are planed for installation. One is used to remove tritium generated during the plasma experiments from vacuum pumping gas (the Pumping-Gas Treatment System). The other is used to enable inspection and maintenance of the LHD vacuum vessel (the Purge-Gas Treatment System) [5].

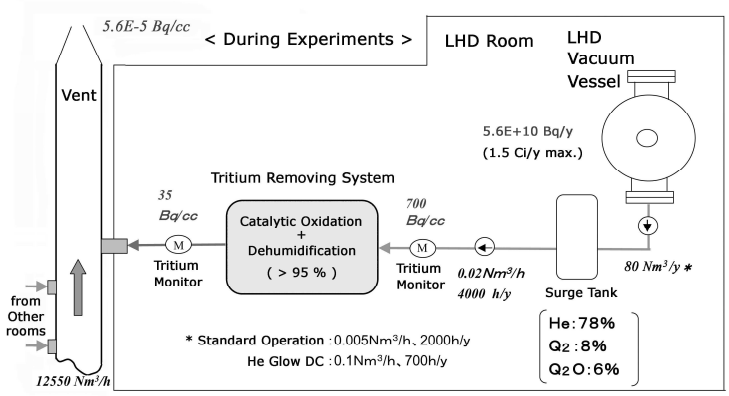

Fig. 1. Conceptual design of the Pumping-Gas Treatment System.

The Pumping-Gas Treatment System uses a conventional combination of a catalytic oxidation and a molecular sieve. Gas with small amount of tritium is oxidize and absorbed by a molecular sieve. When the amount of absorbed water in the molecular sieve is less than 10 %, a dew point

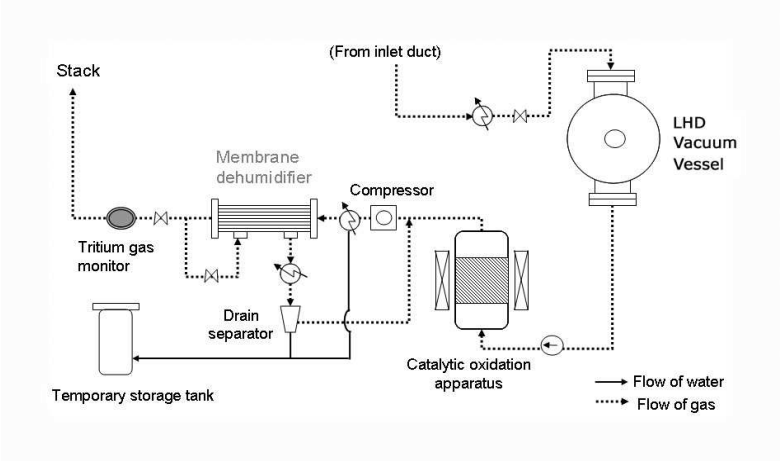

Fig. 2. Conceptual design of the Purge-Gas Treatment System.

lower than -60 °C is readily achieved at room temperature. Conceptual design of the Pumping-Gas Treatment System is shown in Fig. 1.

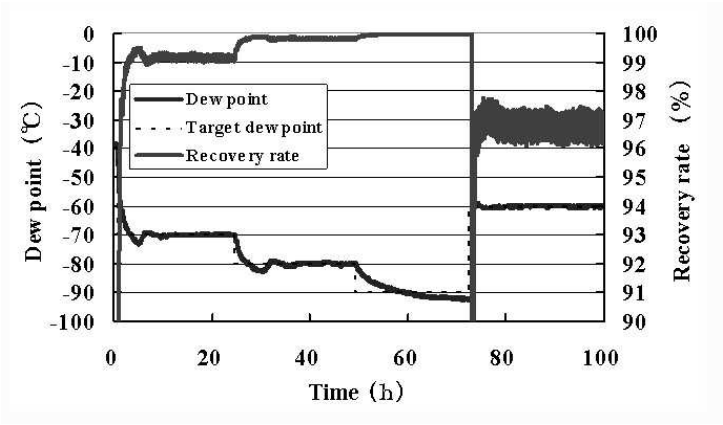

Fig. 3. PID control characteristics.

The Purge-Gas Treatment System uses a combination of a catalytic oxidation and a membrane dehumidifier. If a dew point of polymer membrane dehumidifier is lower than -60 °C, the tritium removing system can be reduced in size and more stable dehumidifying performance can be expected. Since the amount of the purge gas is very large, we are planning to apply a polymer membrane dehumidifier to the Purge-Gas Treatment System. The applied configuration and process flow of the system are shown in Fig. 2. Figure 3 shows the control characteristics of the dew point. The PID control method is applied for the gas flow control. More than 95 % of tritium is recovered (removed from inlet gas).

3. High sensitivity tritium gas detector

High sensitivity tritium gas detector, which can detect the tritium concentration of $5x10^{-4}$ Bq/cm^3, has been developed to ensure the local engagement. To realize such high sensitivity, a proton-conducting ceramic (or oxide) is used as a hydrogen isotope pump. And the pumped tritium is condensed until the detectable concentration within a monitoring interval (~10 min) by a closed loop system. Figure 4 shows a schematic draw of a prototype testing module of hydrogen pump. The evaluation of the performance of this unit is carried out using Ar gas with water vapor. The hydrogen extraction rate reached to 1.8 cm^3/min at 500 mA and 973 K. Figure 5 shows the time evolution of the hydrogen concentration rate

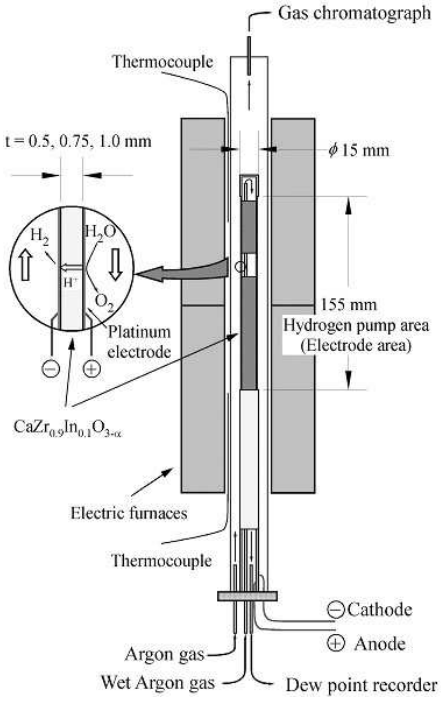

Fig. 4. Schematic draw of a hydrogen pump.

in the closed loop at 973 K. The maximum concentration rate at 625 mA reached abut 5 times higher than that of water vapor in the anode compartment for 50 minutes. It is possible to realize a high sensitivity tritium monitor by the combination of this hydrogen pump and a pulse-shaping analyzer [6].

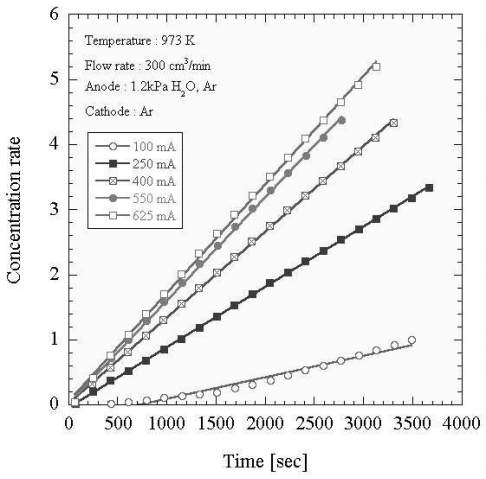

Fig. 5. Time evolution of hydrogen concentration rate.

4. Summary

In order to reduce the tritium release in the environment, two type of tritium removing systems are designed. One is a standard combination of a catalytic oxidation and a molecular sieve for vacuum pumping gas. The other is combination of a catalytic oxidation and a membrane dehumidifier, which has been developed in NIFS, for large amount of vacuum vessel purge gas treatment system. By using membrane dehumidifier, system becomes compact and, as a result, radioactive waste becomes small. In order to compensate the time delay in membrane system, the PID control and hybrid system, which is combination of membrane dehumidifier and an absorbent column, are effective. A high sensitivity tritium gas detector for online tritium monitor has been developed. High sensitivity of $5x10^{-4}$ Bq/cm^3 is realized by a proton-conducting ceramic (or oxide) as a hydrogen isotope pump and a loop system to condense tritium until the detectable concentration. The hydrogen extraction rate of this pump reached to 1.8 cm^3/min at 0.5 A and 973 K. The concentration rate of hydrogen by the loop system reached about 5 times higher than that of water vapor in the anode compartment for 50 minutes.

Acknowledgements

This work was partly supported by the JSPS-CAS Core University Program in the field of Plasma and Nuclear Fusion.

References

[1] A. Iiyoshi, M. Fujiwara, O. Motojima, N. Ohyabu and K. Yamazaki, Fusion Technology, **17**(1990), p169.

[2] O. Motojima, K. Akaishi, M. Asao, K. Fujii *et al*., in Plasma Phys. and Contr. Nucl. Fus. Res. 1990 (Proc. 13th Int. Conf. Washington DC, 1990), Vol.**3**, IAEA, Vienna (1990), p513.

[3] A. Iiyoshi, A. Komori, A. Ejiri, M. Emoto *et al*., Nucl. Fusion, **39** (1999), p245.
[4] M. Fujiwara, H. Yamada, A. Ejiri, M. Emoto *et al*., Nucl. Fusion, **39** (1999), p1659.
[5] Y. Asakura, T. Sugiyama, T. Kawano et al., J. Nucl. Sci. Technol., **41** (2004), p863.
[6] T. Kawano et al., in Tritium Sci. and Technol. 2007 (Proc. 8th Int. Conf., Rochester, 2007).

ERO modelling of hydrocarbon transport and light emission and comparison with gas inlet injection experiments at TEXTOR

R. Ding[1,2], D. Borodin[2], A. Kirschner[2], J. Chen[1], S. Brezinsek[2], V. Philipps[2] and J. Li[1]

1 Institute of Plasma Physics, Chinese Academy of Sciences, P.O. Box 1126, Hefei, Anhui 230031, P.R.China

2 Institut für Energieforschung – Plasmaphysik, Forschungszentrum Jülich, Association EURATOM-FZJ, Trilateral Euergio Cluster, D-52425 Jülich, Germany

E-mail of corresponding author: rding@ipp.ac.cn

Abstract

Modelling with the 3D Monte Carlo code ERO has been done for hydrocarbon transport and resulting light emission. To model the transport of higher hydrocarbon molecules, the whole set of molecular data for reaction chains of C_2H_x species (rate coefficients Janev and Reiter) has been implemented into the ERO code in addition to already existing methane family reactions. Benchmarking experiments at TEXTOR have been performed in which different hydrocarbon molecules (CD_4, C_2D_4, and C_2D_6) were injected into the edge plasma. Light emission of characteristic bands of C_2, CD and lines of CII were observed with CCD cameras. Accordant ERO simulations are compared with the experiment. The modelled penetration depths of CD, C_2 and CII are in good agreement with the experiment. Discrepancies in the inverse photon efficiency (D/XB values) between modelling and experiments occur especially for CD emission and are contributed to uncertainties in the excitation rates.

Keywords: ERO code, hydrocarbon transport, light emission, inverse photon efficiency D/XB, TEXTOR

1. Introduction

Chemical erosion of carbon-based materials by formation of hydrocarbon molecules has a significant influence life time of these materials and on tritium retention, which are limiting factors for the availability of ITER. Measurement of chemical erosion yield in fusion experiments is mainly based on spectroscopic observation of CD A-X band and C_2 d-a emission [1]. The respective inverse photon efficiency D/XB (decay per excitation) is used to convert photon flux into particle flux. The C_2 molecule appears as decay product of higher hydrocarbons e.g. ethane, whereas the flux of CD represents the total hydrocarbon influx into the plasma. However, light emission includes atomic/molecular physics and hydrocarbon transport in the edge plasma of fusion experiments. The transport is influenced by plasma parameters, geometry, surface conditions, etc.

Benchmarking experiments were carried out at TEXTOR in which a known amount of various hydrocarbon molecules (CD_4, C_2D_4, and C_2D_6) was injected into the H plasma near the last closed flux surface (LCFS) through a gas inlet [2]. The cylindrically shaped gas inlets with an inner radius of 4 mm and an outer radius of 5 mm was positioned in the scrape-off layer (SOL) 15 mm outside the LCFS. The small surface on the top of the inlet reduces the surface effects (recycling of hydrocarbons) on light emission. 2D image images of light emission from top and from side were recorded with intensified CCD cameras equipped with interference filters (Fig.1). The D/XB values are defined as the ratio of hydrocarbon influx and intensity of emission from CD or C_2. For CD_4, the D/XB values are given by $\left[\frac{D}{XB}\right]_{A-X}^{CD_x \to CD} = \frac{\Gamma_{CD_x}}{\phi_{A-X}^{CD_x \to CD}}$, where Γ is the CD_4 flux and ϕ the photon flux of CD light.

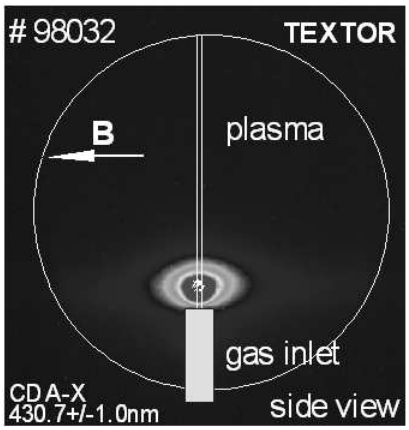

Fig. 1. 2D pattern of CD light emission from side view during CD_4 injection in TEXTOR.

2. The ERO code

The 3D Monte Carlo code ERO based on the test particle approximation simulates the plasma-wall interaction and the transport of impurity particles in a given background plasma [3]. Modelling of hydrocarbon transport requires a large set of atomic and molecular data. In addition to methane, in the meanwhile also the reaction system for ethane has been implemented into ERO using Janev/Reiter database [4] for the rate coefficients. There are now altogether 314 reactions. Light emission is calculated in ERO using effective photon emission rate coefficients. These emission coefficients are given by [5] for CD Gerö band and C_2 Swan band and by the ADAS database [6] for CII.

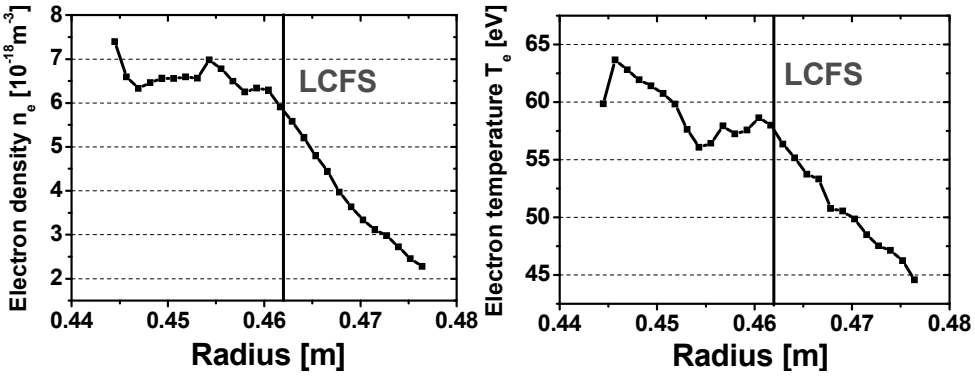

Fig. 2. Edge plasma profiles of electron density n_e (left) and temperature T_e (right) from helium beam diagnostic in TEXTOR.

The modelling geometry used is a cylinder of 4 mm radius. The hydrocarbon molecules are launched from the top of this cylinder with a cosine distribution. Electron density and temperature in the plasma boundary of TEXTOR, Fig. 2, are measured with a helium atomic beam diagnostic [7]. The gas inlet position is given as radial distance between inlet top and LCFS.

3. ERO Modelling in comparison with the experiments

First, the methane (CD_4) injection experiment at TEXTOR has been modelled. One important input parameter for the modelling is the effective sticking coefficient for hydrocarbons hitting a surface S_{eff}. Two extreme cases, $S_{eff} = 1$ and $S_{eff,}$ have been studied. With radial distance of the gas inlet to the LCFS of 15 mm (as in the experiment), the modelled D/XB value for CD in full sticking case is 157, which is much higher than the value of 80 with zero sticking and also than the experimental value 36. With $S_{eff} = 1$, about 66% of injected hydrocarbon radicals are deposited on the inlet surface. More than 90% of deposited hydrocarbon species are deposited before they are dissociated to CD radical, which results in reduced CD density and thus CD light emission compared to the assumption of $S_{eff} = 0$. When radial distance to LCFS is increased to 25 mm, the D/XB values are reduced to 96 with $S_{eff} = 1$ and 71 with $S_{eff} = 0$. In general, the D/XB values decrease with increasing radial distance to the LCFS. The local plasma temperature and density near the inlet are lower when the gas inlet is farther away from the LCFS. With smaller electron temperature and density, the density of CD (and thus CD light) is larger due to smaller dissociation and ionization rates, which results in smaller D/XB values. Also, with increased distance between gas inlet and LCFS, the hydrocarbon radicals can move deeper into the plasma to larger distances from the inlet top, which finally leads to reduced loss of hydrocarbons caused by sticking. Thus, the surface effect on D/XB becomes less important when the radial distance to the LCFS becomes larger. No significant surface exists on the top of the gas inlet in experiment. Therefore, the assumption $S_{eff} = 0$ is more reasonable for our calculation.

Another important parameter is the sheath electric field, which is directed perpendicular to the surface. Due to the specific geometry of the gas inlet, an exact calculation of the sheath field is complicated. Therefore, two extreme cases with and without sheath field are studied ("E_{sheath} = on" and "E_{sheath} =0"). Within the "E_{sheath} = on" case, the inlet top is considered as a disk surface. The sheath field is assumed to be zero within "E_{sheath} = 0" case. Assuming zero sticking for hydrocarbons, the simulated D/XB value of 65 with "E_{sheath} = 0" is slightly lower than the value of 80 for the "E_{sheath} = on" case, and thus is nearer to the experimental value of 36. Also, the penetration depth of CD of about 11 mm with "E_{sheath} = 0" is very similar to the experimental value, while the penetration depth of 16 mm in the "E_{sheath} = on" case is significantly higher. The sheath electric field induces increased recycling on the "non-existing" surface on top of the gas inlet and should be neglected in the modelling.

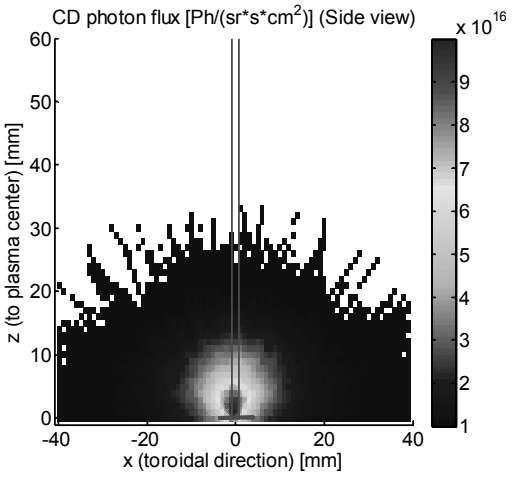

Fig. 3. Modelled 2D light emission of CD resulting from CD_4 injection.

Fig. 3 shows the 2D pattern of CD light emission from simulation (assuming zero sticking for hydrocarbons and "E_{sheath} = 0"). The radial profiles along the

central axis (indicated in Fig.3) of CD and CII emission are in good agreement with the experiment (Fig. 4).

Injection experiments of C_2D_4 and C_2D_6 have been carried out with the same conditions as the CD_4 injection experiment. D/XB values for CD and C_2 from experiments and modelling assuming $S_{eff} = 0$ and "$E_{sheath} = 0$" are given in table 1. The D/XB values for C_2 from simulation and experiments are very similar. Modelled D/XB values for CD are always larger than measured ones. This indicates uncertainties of the excitation rate coefficients of the CD band. The observed penetration depths for C_2 and CII resulting from C_2D_4 injection are in good agreement with the modeling (Fig. 5).

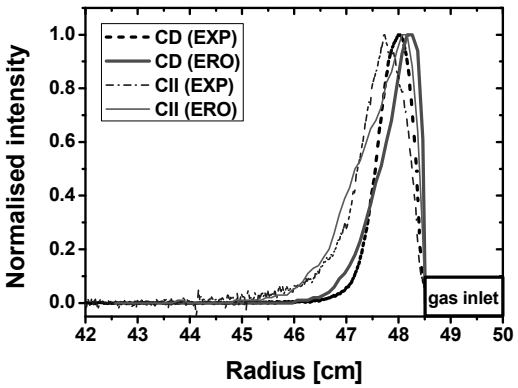

Fig. 4. Radial light emission profiles of CD and CII from CD_4 injection: experiment (EXP) vs. modeling (ERO).

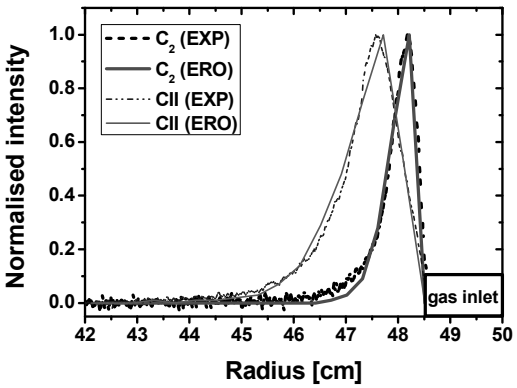

Fig. 5. Radial light emission profiles of C_2 and CII from C_2D_4 injection: experiment (EXP) vs. modeling (ERO).

4. Summary

The good agreement of modelling results with experimental data proves the reasonability of ERO calculation and hydrocarbon reaction database. The assumptions of sticking coefficient zero and no sheath electric field lead to best agreement with the experiments. The discrepancies of D/XB values for CD from modelling and experiments indicate uncertainties of the emission rate coefficients.

Injected species	D/XB (CD A-X band)		D/XB (C_2 d-a band)	
	Experiment	ERO	Experiment	ERO
C_2D_4	31	80	48	45
C_2D_6	27	76	65	62

Table 1. Modelled and measured D/XB values for CD A-X band and C_2 d-a.

Acknowledgements

The authors gratefully acknowledge support by a "Helmholtz-CSC Fellowship". This work was partly supported by the JSPS-CAS Core University Program in the field of Plasma and Nuclear Fusion.

References

[1] S. Brezinsek, A. Pospieszczyk, et al., Phys. Scr., **111**(2004)42-48.

[2] S. Brezinsek, A. Pospieszczyk, et al., J. Nucl. Mater., **363-365**(2007)1119-1128.

[3] A. Kirschner, V. Philipps, et al., Nucl. Fusion, **40**(2000)989-1001.

[4] R. Janev and D. Reiter (2003) Report Jül-4005, Forschungszentrum Jülich.

[5] U. Fantz, S. Meir, et al., J. Nucl. Mater., **337-339**(2005)1087-1091
[6] http://www.adas.ac.uk
[7] O. Schmitz, I. Beigman, et al., Plasma Phys. Control. Fusion, **50**(2008)115004

Wall Conditionings Using He, Ne and Ar Gases

Y. Yamauchi, K. Takeda, Y. Higashi, Y. Nobuta, T. Hino
Laboratory of Plasma Physics and Engineering, Hokkaido University, Sapporo, 060-8628 Japan
E-mail of corresponding author: yamauchi@qe.eng.hokudai.ac.jp

Abstract

Glow discharge experiments using helium, neon and argon gases were conducted for the stainless steel which has already retained hydrogen, and then the amount of desorbed hydrogen and retained discharge gases was evaluated. In addition, the effect of neon or argon glow discharge on the removal of helium retained in the stainless steel was also evaluated. The removal ratio of retained hydrogen by the neon glow discharge cleaning with 2hr was 47%, which was 1.3 times larger than that by an argon glow discharge, and a half of that by a helium glow discharge. In the case of the neon glow discharge to the stainless steel which has already retained helium, the removal ratio of retained helium was 51%, which was 4 times larger than that by the argon glow discharge. The amount of retained neon was an order of magnitude smaller than that of retained helium in the stainless steel.

Keywords: Wall conditioning, Glow discharge cleaning, Gas retention, Stainless steel

1. Introduction

Hydrogen isotope retention in plasma facing material is one of important issues concerning with the safety and the density control of fusion reactor [1]. Helium glow discharge cleaning has been widely employed in order to remove the hydrogen isotope and the surface impurities from the first wall [2, 3]. The large helium desorption from the first wall, however, was observed during the main discharge after the helium discharge cleaning in the Large Helical Device (LHD) [4], resulting in the deterioration of the plasma confinement. So, the alternative or additional conditioning method might be necessary for the reduction of hydrogen isotope and/or helium retention. The neon or argon glow discharge might be attractive cleaning method for the removal of retained hydrogen isotope and/or helium. In the present study, glow discharge experiments using helium, neon and argon were conducted for the stainless steel which has already retained hydrogen or helium, and then the amount of desorbed hydrogen or helium and retained discharge gas was evaluated by residual gas analysis.

2. Experiments

The glow discharge device used in the present study has been described in the previous

literature [5]. The cylindrical liner made of 316L SS, which was the same material of plasma-facing wall in LHD, was installed in the device. Introducing a constant flow of discharge gas using mass flow controllers, the glow discharges were conducted between a copper anode and the liner at room temperature. The discharge pressure was 8 Pa. The discharge duration was 2 hrs. The discharge voltage was 200-300 V. During the discharge, the desorbed or retained amount of gases for the liner was quantitatively measured by a residual gas analysis using a quadrupole mass spectrometer. The desorbed or retained amount was obtained from the pressure decrease or increase during the discharge. These amounts were normalized by the surface area of the liner (7700 cm^2).

In order to evaluate the hydrogen removal by glow discharge, helium, argon or neon glow discharge was conducted to the liner in which hydrogen have been already retained by the hydrogen glow discharge. In addition, in order to evaluate the effect of glow discharge on the reduction of helium retained in the liner, the argon or neon glow discharge was also conducted to the liner in which helium have been already retained by the helium glow discharge.

3. Results

3.1 Reduction of hydrogen retention by glow discharge cleaning

Before the glow discharge cleaning, the hydrogen glow discharge was conducted in order to retain the hydrogen in the liner. The amount of retained hydrogen by the hydrogen discharge was estimated as 5.2×10^{16} H/cm^2 by the residual gas analysis. Fig. 1 shows the time evolution of hydrogen and neon partial pressure during the neon glow discharge after the hydrogen glow discharge. The ion current density was 1.5×10^{-5} A/cm^2. Large desorption of hydrogen from the liner in addition to the neon retention was observed at the initial period of the glow discharge. The hydrogen desorption rate was almost constant above 2000 s in the discharge time. The amount of desorbed hydrogen during the neon glow discharge was 2.4×10^{16} H/cm^2, which corresponded to 47% of the amount of retained hydrogen before the neon glow discharge.

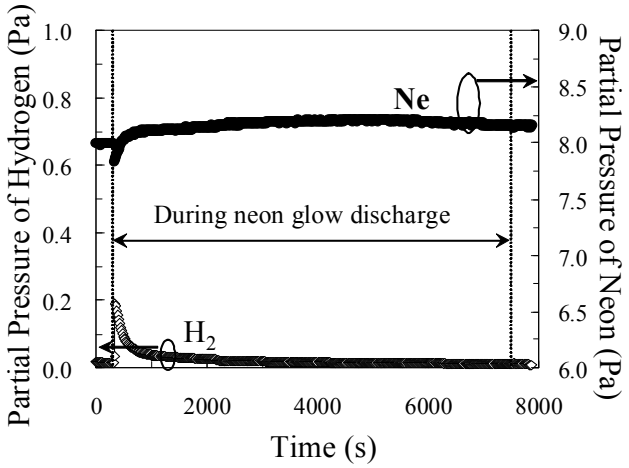

Fig.1 Typical time evolution of hydrogen and neon partial pressure during neon glow discharge cleaning after hydrogen glow discharge.

Ion current density dependence of fraction of removed hydrogen is shown in Fig. 2. It was found that the discharge using helium gas was the most effective for the reduction of hydrogen. In the case of

the neon discharge with 2hr, maximum fraction of removed hydrogen was 1.3 times larger than that by the argon discharge, and a half of that by the helium discharge in the present study. Large fraction of removed hydrogen in the case of helium discharge was owing to large energy transfer and little sputtering. In the case of argon discharge, it is speculated that significant sputtering occurred and then a thick re-deposited layer was formed on the SS liner. The re-deposited layer may result in small fraction of removed hydrogen in the case of the argon discharge.

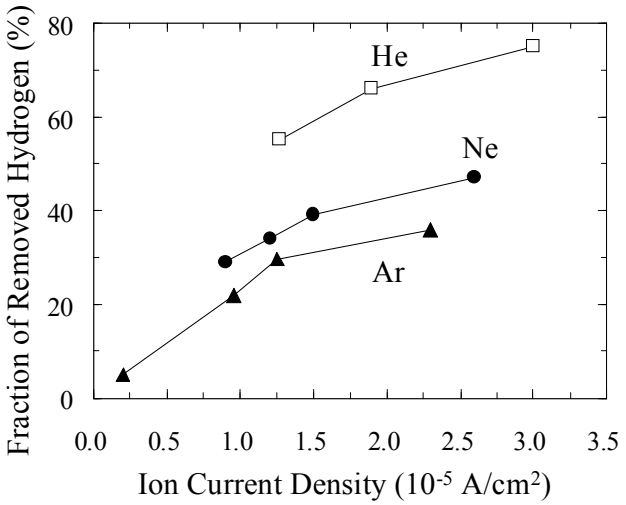

Fig.2 Ion current density dependences of fraction of removed hydrogen by helium, neon and argon glow discharge after hydrogen discharge.

Ion current density dependence for amounts of retained discharge gases is shown in Fig. 3. Large gas retention was observed in the case of the helium discharge. The amount of retained neon was an order of magnitude smaller than that of retained helium, and an order of magnitude larger than that of retained argon for the stainless steel. The large helium retention might be owing to the easy formation of the blister because of its deep projected range. Both the fraction of removed hydrogen and amounts of retained gases increased with the ion current density.

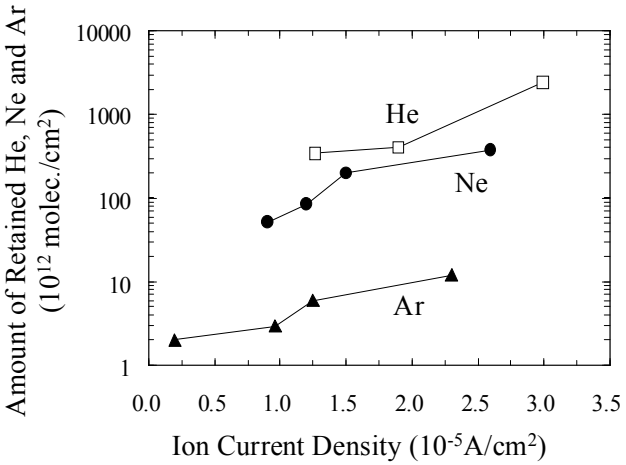

Fig.3 Ion current density dependences of retained amount of discharge gases by helium, neon and argon glow discharge after hydrogen discharge.

3.2 Reduction of helium retention by glow discharge cleaning

The amount of retained helium after the helium glow discharge was estimated as 2.1×10^{14} He/cm^2. Fig. 4 shows time evolution of helium and neon partial pressure during the neon glow discharge after the helium glow discharge. Helium desorption with relatively long period was observed during the neon glow discharge. This long desorption behavior might be owing to the small diffusion coefficient of helium atom, compared with that of hydrogen atom. The amount of desorbed helium was 1.1×10^{14} He/cm^2, which corresponded to 51% of the amount of retained

helium before the neon glow discharge.

4. Summary

In order to examine the effect of neon glow discharge cleaning on hydrogen or helium removal, neon glow discharge was conducted for the stainless steel after the exposure to hydrogen or helium glow discharge. The removal ratio of retained hydrogen by the neon discharge with 2hr was 1.3 times larger than that by the argon discharge, and a half of that by the helium discharge. In the case of the neon discharge following the helium discharge, the removal ratio of retained helium was 4 times larger than that by the argon discharge. The amount of retained neon was an order of magnitude smaller than that of retained helium in the stainless steel. The effect on hydrogen or helium removal and the retention of discharge gas species is associated with the sputtering of the liner followed by the re-deposition and projected range of ion. These results indicate that the neon glow discharge is more attractive than the argon glow discharge for the reduction of hydrogen isotope retention, although the neon retention in the stainless steel is not negligible.

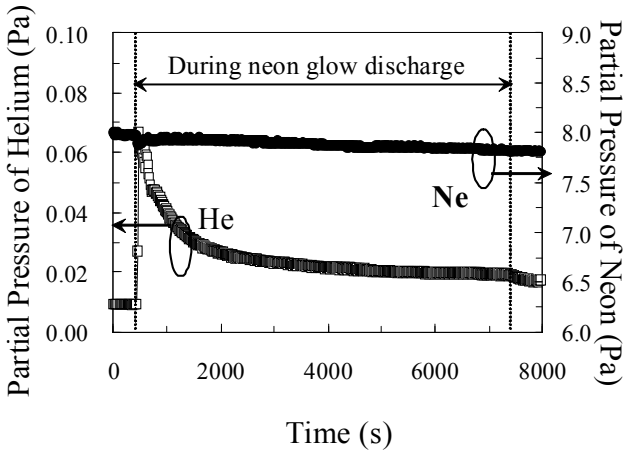

Fig.4 Typical time evolution of helium and neon partial pressure during neon glow discharge cleaning after helium glow discharge.

Acknowledgements

This work was partly supported by the JSPS-CAS Core University Program in the field of Plasma and Nuclear Fusion.

References

[1] For example, H. Yoshida, Y. Yamauchi, Y. Hirohata, T. Arai, S. Suzuki, M. Akiba, N. Miya, T. Hino, J. Nucl. Mater. 337-339 (2005) 604.

[2] For example, K. Nishimura, N. Ashikawa, S. Masuzaki, J. Miyazawa, A. Sagara, M. Goto, B.J. Peterson, A. Komori, N. Noda, K. Ida, O. Kaneko, K. Kawahata, T. Kobuchi, S. Kubo, S. Morita, M. Osakabe, S. Sakakibara, R. Sakamoto, K. Sato, T. Shimozuma, Y. Takeiri, K. Tanaka, O. Motojima and LHD Experimental Group, J. Nucl. Mater. 337-339 (2005) 431.

[3] H. Nakamura, S. Higashijima, K. Isobe, A. Kaminaga, T. Horikawa, H. Kubo, N. Miya, M. Nishi, S. Konishi, T. Tanabe, Fusion Eng. Des. 70 (2004), 163.

[4] H. Suzuki, N. Ohyabu, A. Komori, T. Morisaki, S. Masuzaki, J. Miyazawa, R. Sakamoto, M.

Shoji, M. Goto, S. Morita, Y. Kubota, O. Motojima and The LHD Experimental Group, J. Nucl. Mater. 313-316 (2003) 297.

[5] T. Hino, Y. Higashi, Y. Yamauchi, A. Komori, K. Nishimura, N. Ashikawa, Vacuum 83(2008), 493.

Design of a 45 kA superconducting transformer for testing correction coil conductor short sample

Yi Shi[1] and Yu Wu[2]
1 Institute of Plasma Physics, the Chinese Academy of Sciences, Hefei, 230031, China
2 Institute of Plasma Physics, the Chinese Academy of Sciences, Hefei, 230031, China
E-mail of corresponding author: shiyi@ipp.ac.cn

Abstract

ITER CC will be manufactured in China. The CC conductor short sample will be tested to assess the performance before coils manufacturing and winding. A test facility will be set up at the Institute of Plasma Physics, the Chinese Academy of Sciences in China. This test facility was constructed to superconductor studies: short sample tests, stability studies, losses studies, etc.

A new superconducting transformer will be designed which allows rating of the test CC conductor samples up to 45kA under different cooling conditions. The superconducting transformer is composed with two concentric layer-wound superconducting solenoids with the primary inside the secondary. The primary of the transformer, consisting of 3820 turns solenoid coil, is wound by 0.87mm NbTi superconducting strand, the maximum operating current is about ±200A. The 45 kA secondary conductor, consisting of 4 turns of rectangular cable-in-conduit type based in 0.87mm NbTi superconductor, is wound directly on the top primary in order to have a high couple.

This paper describes the principles of transformer, the designed parameter analysis of the superconducting transformer, stress and strain analysis on the superconducting coils.

Keywords: ITER CC test facility, Superconducting transformer, NbTi, Conductor

1. Introduction

ITER CC will be manufactured in China. The CC conductor short sample will be tested to assess the performance before coils manufacturing and winding. A test facility will be set up at the Institute of Plasma Physics, the Chinese Academy of Sciences.

The aim of this test facility is to provide a 5 T DC bias field. This test facility is constructed to superconductor studies: short sample tests, stability studies, losses studies, etc. The current in the test samples is supplied by a superconducting transformer instead of using an expensive power supply and large, power-consuming current leads. The induced current method of feeding superconducting loops is particular advantageous at the very high currents required for testing ITER conductors. Recently, the facility has been developed with a new superconducting transformer generating currents up to 45 kA in the test sample. The design parameter of the superconducting transformer are: the maximum sample current 45 kA, the maximum secondary circuit resistance 10 nΩ, the maximum measurement time 400s, secondary current measurement accuracy 0.5%, and primary power supply(bipolar) maximum operating current 200A.

2. Transformer circuit feature and design principle

A superconducting transformer for current step-up consists of two inductively coupled superconducting coils, a high-turn primary and a low-turn secondary circuit which contains the test conductor**[1][2]**. By energizing the primary coil, a current will be induced in the secondary turns. Fig.1 shows the equivalent circuit of the transformer. The governing equations for the circuit are

$$\begin{aligned} L_p \cdot \dot{I}_p + M \cdot \dot{I}_s + R_p \cdot I_p &= E \\ (L_s + L_{sp}) \cdot \dot{I}_s + M \cdot \dot{I}_p + R_j \cdot \dot{I}_s &= 0 \end{aligned} \qquad (1)$$

Where, L_p and L_s are self-inductance of the primary and secondary, L_{sp} is self-inductance of the sample, R_s is resistance of the sample(when going to normal), R_p and R_j are resistance of the circuit including the primary and the joint in the secondary circuit, M is mutual inductance between primary and secondary, I_p 和 I_s are current in the primary and secondary.

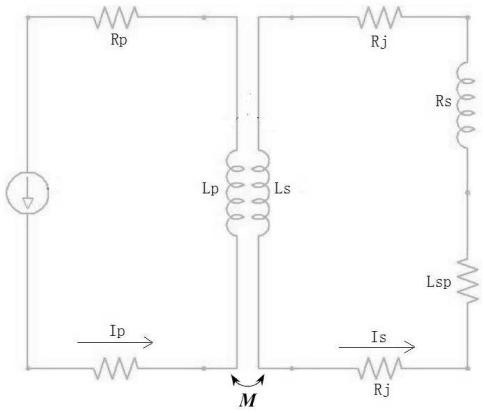

Fig.1 Equivalent circuit of the superconducting

For simplicity, in these equations, we have assumed $-dI_p/dt = C$ =constant and that the resistance of the sample is zero (the sample is in the superconducting state). We obtain, with the starting condition $I_s(t=0)=0$

$$I_s = \frac{MC}{R_j}(1-e^{--t/\tau}) \qquad (2)$$

Where τ is the time constant given by $\tau = (L_s + L_{sp})/R_j$.

Equation (2) can be written in a more convenient way since the constant C is given by $C = -(I_p(t) - I_0)/t$

$$I_s(t) = \frac{M}{L_s + L_{sp}}(I_p(t) - I_0)\cdot\frac{\tau}{t}\cdot(1-e^{-\frac{1}{\tau}t}) \qquad (3)$$

Equation (3) allows us to obtain the two important pieces of information related to the transformer: the current transformer ratio and the maximum current that can be induced in the secondary.

The ideal current transformer ratio, also called the current amplification factor, i.e. the ratio between the current in the secondary and the current variation in the primary, can be obtained from equation(3) in the limit $t/\tau \to 0$

$$\alpha_0 = \frac{L_s}{I_p - I_0} = \frac{M}{L_s + L_{sp}} = \frac{k\cdot(L_p\cdot L_s)^{\frac{1}{2}}}{L_s + L_{sp}} \qquad (4)$$

Where, k is the coupling constant between primary and secondary.

The maximum current that can be induced in the secondary circuit, obtainable from Equation (2) $t/\tau \to \infty$

$$I_{s\max} = \frac{M\cdot c}{R_j} \qquad (5)$$

Equation (4) and (5) say that in order to reach a high transformation ratio, it is not only sufficient to have a high turn ratio and close coupling between the primary and secondary coil, but it is also necessary to have a low inductance of the secondary load, i.e. of the test sample and the secondary inductance is slightly high than the sample inductance. In order to achieve a secondary time constant which is large compared to the measuring time, the sum of the joint resistance in the secondary loop R_s must have a value lower than $10^{-8}\Omega$.

3. Transformer design parameter and conductor design concept

Based on these design principles, a superconducting transformer which supplies 45 kA by charge the primary with less than 200A has been designed. The superconducting transformer is composed with two concentric layer-wound superconducting solenoids with the primary inside the secondary. The primary of the transformer, consisting of 3820 turns solenoid coil, is wound by 0.87mm NbTi superconducting strand supplied by Russia which has a Cu:NbTi ratio of 1.38, the maximum operating current is about ±200A. The 45 kA secondary conductor, consisting of 4 turns of rectangular cable-in-conduit type based in 0.87mm NbTi superconductor, is wound directly on the top primary in order to have a high couple. This concentric coil configuration leads a computed coupling coefficient of 0.7. In order to keep the inductance of the secondary load as low as possible, a test conductor will be curved U shape and wound by double spire. The main characteristics of the superconducting transformer are summarized in table1.

For high current secondary conductor the cable-in conduit concept (CICC) has been chosen. It consists of a multistage cable enclosed in a high-strength steel jacket. The conductor is designed to carry currents up to 45 kA. Table 2 present the main characteristics of the secondary conductor.

Table1 Main characterized of the45kA transformer

	Primary	Secondary
Winding type	Lay-wound	Layer-wound
Number of turns	3820	4
Winding i.D.	77.8 mm	124 mm
Winding o.D.	114 mm	164 mm
Winding length	180 mm	180 mm
Inductance	0.503H	1.17E-6H
Max.operating current	±200 A	45 kA
Superconductor	UNK NbTi	UNK NbTi
Coefficient of coupling	0.74	0.74

Table2 characteristics of the 45 kA secondary conductor

Strand diameter	0.87mm
Cable pattern	3×3×7×7
Number of superconducting strands	294
Number of copper strands	147
Cu:NbTi ratio	2.38
Conduit thickness	1.5mm
Void fraction inside the conduit	34%
Conductor dimensions	17.5×33.5 mm^2
Maximum operating current	45 kA
$I_{op\max}/I_c$ at 45kA 45kA and 5T	0.28

A key element of the conductor design was the choice of the superconductor. The conductor with the largest current carrying capacity which is at present expected for testing is the ITER correction conductor coil based on NbTi strands. There will be no significant difference between the critical currents of a secondary coil based on NbTi strands and that of a wind-and-react Nb3Sn secondary coil at 5T and 4.2K. Based on its relative simple fabrication and use, the strain tolerant and cheaper NbTi superconductor has been favored.

To obtain desired critical current, a cable design was made using 294 NbTi superconducting wires in four cabling stages. The 0.87 mm diameter NbTi wire with a Cu:NbTi ratio of 1.36 was supplied by Russia. The first two stages are triplet configurations. The third stage is a 7-element cable (6 around 1). In the last stage, 7 subcables are twisted and subsequently compacted to a rectangular shape. 147 copper wires are incorporated in the cabling layout by replacing one of the superconducting wires in the first cable stage by a copper wire. This will help the conductor to withstand the rise of conductor temperature and helium pressure following a quench. The fabrication of the secondary conductor was divided into two parts: (1) cabling and (2) jacketing.

4. Stress and stain analysis of transformer coil and conduit

For high field superconducting transformer coils, the structure of a superconducting magnet is made of composite. In general, composite materials contain a few bonded components, each of which is with quite different structural properties such as superconducting wire, epoxy-resin and conduit 316LN stainless steel in the

coils that cause many hard points in the stress-strain characteristics. However, to solve the stress problem in composite structures, an analysis has to be made to obtain the effective structural properties based on the mechanical characteristics of individual materials in the composite. In some cases, the properties of material are averaged according to the size of space occupied by different materials. the three-dimensional finite element analysis model is created. The finite element stress and strain analysis has been carried out and main results are show intable3.

It is obvious that the rectangular conduit is not the ideal shape to withstand large internal helium pressure as developed during quenching at high currents. To provide information on deformation and stress on the conduit when the secondary coil was quench at high currents. We also used the three-dimensional finite element analysis model. The analysis results on different inner pressures are shown in the table4. In order to get information on the effect of the inner pressure on the conduit, the father experiment will be able to carry out to make sure that the mechanical integrity of the conduit was not affected.

Table3 Calculated stress and stress on the primary and secondary coils

Primary				Secondary			
X-stress	1.46MPa	X-strain	0.026%	X-stress	0.9MPa	X-strain	0.007%
Y-stress	2938MPa	Y-strain	0.047%	Y-stress	3.95MPa	Y-strain	0.006%
Z-stress	10.2MPa	Z-strain	0.037%	Z-stress	0.87MPa	Z-strain	0.003%

Where: X=Radial direction, Y=circumferential direction, Z=Axial direction

In order to protect the secondary winding package against uncontrolled deformation following a quench, a stainless steel reinforcement shell surrounds the secondary coil. Increase the thickness of the steel jacket itself is not viable solution as this may effects the bending ability of the conductor.

Table4. Deformation and stress on the conduit in different pressures

	Item of calculated	Value		Item of calculated	Value
A	deformation（mm）	0.407	B	deformation（mm）	0.814
	Von mises stress（MPa）	470		Von mises stress（MPa）	939
	Membrane stress（MPa）	365.6		Membrane stress（MPa）	731.3
	Bending stress（MPa）	134.3		Bending stress（MPa）	268.6
	Membrane + Bending（MPa	499.1		Membrane + Bending（MPa）	998.1

Where: A-3MPa pressure, B-6MPa pressure

5. Summary

ITER CC will be manufactured in China. The design and analysis of a new superconducting transformer for the ITER CC short samples generating currents up to 45 kA has been demonstrated. The design of the CICC type secondary conductor was guided by consideration of handling, stress and stain analysis, mechanical strength and safely. The transformer works as a low noise current source which allows the use of sensitive criteria in samples short sample tests, stability studies, losses studies, etc.

Acknowledgements

This work was partly supported by the JSPS-CAS Core University Program in the field of Plasma and Nuclear Fusion.

References

[1] G. Pasztor, E Aebli, B. Jakob, P. Ming, E Sigrist, P. Weymuth,, Proc, of 11th Int. Conf. On Magnet Technology(MT-11) 467-470

[2] G. Pasztor, Alexander Anghel, Bertrand Blau. ect, Proc, of 15th Int. C onf. On Magnet Technology(MT-15) 839-842

Applications of tungsten coated materials for divertor and first wall materials

K.Tokunaga[1], Y.Yahiro[1], N.Yoshida[1], N.Ashikawa[2], M.Tokitani[2], S.Masuzaki[2]
, A.Komori[2],N. Noda[2], K.Ezato[3], S.Suzuki[3], M.Akiba[3], A. Kobayashi[4]

1 Research Institute for Applied Mechanics, Kyushyu University, Kasuga, Fukuoak 816-8580, Japan
2 National Institute for Fusion Science, Toki, Gifu 509-5292, Japan
3 Japan Atomic Energy Agency, Naka, Ibaraki 311-0193, Japan
4 Joining and Welding Research Institute, Osaka University, Ibaraki, Osaka, 567-0047, Japan
E-mail of corresponding author: tokunaga@riam.kyushu-u.ac.jp

Abstract

W-coated carbon tile and W-coated reduced activation ferritic / martensitic (RAF/M) steel have been fabricated and have been investigated to apply as the divetor and the first wall/blanket. The W-coated carbon tiles have been exposed to hydrogen divertor plasma discharges in the LHD. No exfoliation and cracks have been observed on the tiles. Detail surface analyses are now underway. On the other hand, tungsten has been successfully coated on RAF/M steel (F82H) substrate by plasma spraying technique. Surface morphology of the deposited W and adhesion property between the substrate and the coatings have been investigated by SEM/TEM/EDS and XRD. In addition, microstructure and phase transformation behavior of F82H on the interface before and after heat treatment have been observed by OIM.

Keywords: Tungsten, Coating, Carbon, Low activation material, Reduced activation ferritic/martensitic steel

1. Introduction

Tungsten is potential candidate for an armor of the firsr wall and the divertor plate because of its low erosion yield and good thermal properties. The disadvantages of tungsten are its heavy weight and the brittleness below DBTT. For the near term application, tungsten coated carbon tile could be convenient because of light weight and good mechanical and thermal property of the carbon materials. On the other hand, in the case of DEMO reactor, neutron damage will be a critical issue. Structure materials of the first wall/blanket and the cooling channels of divertor will be made by low activation materials. Tungsten coated reduced activation materials could be convenient for the first wall/blanket because the thickness of tungsten on the first wall/blanket is designed about 2 ～ 3 mm and the coating technique can be used for this. In the present work, plasma sprayed tungsten

has been also successfully coated on reduced-activation ferritic/martensitic steel (RAF/M) F82H substrate.

2. Experiments

Tungsten coatings on graphite by plasma spray (PS) or physical vapor deposition (PVD) were produced and their performance under high heat flux loading has been examined. Plasma sprayed tungsten coated materials are very useful as the tungsten armor of the high heat flux components because a coating rate is high and thick coatings of tungsten can be possible. Tungsten coatings on CFC and isotropic fine grain graphite have been successfully produced by vacuum plasma spray (VPS) technique and their good thermal and adhesion properties have been confirmed by high heat flux tests[1,2,3]. Furthermore, VPS-W coated CX-2002U and IG-430U were brazed on the OFHC with a cooling tube. Their thermal response on the mock-ups has been carried out under an actively cooling condition using electron beams[4]. In addition, surface modifications such as blistering and hydrogen isotope/helium retention of VPS-W irradiated by a low energy and high flux hydrogen isotope/helium have been also investigated[5,6].

Recently, higher density VPS-W coated CFC and isotropic fine-grained graphite compared to the previous one have been developed[7]. In the present work, VPS-W coated CFC and isotropic fine-grained graphite have been exposed to LHD divertor plasma to evaluate its performance for the LHD divertor plate.

Tiles (20mm x 20mm x 10mm) of carbon/carbon composite CX-2002U and isotropic fine grained graphite IG-430U made by Toyo Tanso Co. were coated with tungsten by vacuum plasma spraying technique(VPS). The thickness of the VPS-W layer was 0.5 mm and its density was 98% of the theoretical value. The VPS-W coated CX-2002U and IC-430U were mounted on the probe head. They were transferred to the divertor-leg position by using the retractable material-probe system equipped with the LHD, and then exposed to successive hydrogen discharges with magnetic axis of 3.75 m and 3.6 m. In the case of magnetic axis of 3.75m, the VPS-W coated tiles were exposed to successive 20 discharges of 2s (shot-#73474-73439, 40 s in total), by NBI heating (7.7 MW(2s), 5.1 MW(1s)). On the other hand, in the case of magnetic axis of 3.6 m, the VPS-W coated tiles were exposed to successive 23 discharges of about 2s (shot-#75747-75769, about 40 s in total), by NBI heating (3.5 MW(2s), 3.5 MW(1.5s)). Typical electron density(ne) in core plasma and Te(～Ti) in the divertor region were 6 - 8 x 10^{19} m^{-3} and a few 10 eV. The temperatures of the VPS-W coated carbon tiles were monitored by thermocouples inserted to the carbon tiles of position of 2.5mm beneath from the surface.

After the exposure, surface morphology, microscopic damage and chemical composition were examined by means of scanning electron microscopy (SEM) and energy dispersive spectroscopy (EDS), respectively. In addition, chemical composition including in hydrogen has been examined

by Rutherford Backscattering Spectrometry (RBS) and Elastic Recoil Detection(ERD) .

In addition, tungsten coating on reduced-activation ferritic/martensitic steel (RAF/M) F82H substrate (F82H: Fe-8Cr-2W) by Atmospheric Plasma Spraying (APS), Vacuum Plasma Sprayin(VPS) and Gas Tunnel Type Plasma Spraying (GTP). Surface morphology of the deposited W and adhesion property between the substrate and the coatings have been investigated using SEM/EDS and XRD. Microstructure and phase transformation behavior of F82H on the interface before and after heat treatment have been also observed using OIM. Heat flux tests using electron beam have been carried out.

3. Results

In the case of magnetic axis of 3.75 m, four lines were observed on the probe head along the divertor leg. The color of the four lines changed from metallic sliver to typically red and blue by the exposure. EDS analyses showed that C was included in the color change area. In addition, large amount of hydrogen also exists in this area. This four change area is considered to be re-deposited layer and corresponds to the divertor structure. Cracks on the surface and exfoliation between the joint interface of VPS-W and carbon on the VPS-W coated carbon tiles were not formed. On the other hand, in the case of magnetic axis of 3.6 m, footprint trace of divertor leg on a retainer plate made by tungsten seemed to be molten and re-solidified. However, macro and microscopic cracks were not formed on the VPS-W coated carbon tiles. These results indicates that the thermal and adhesion properties between the substrate and coatings were good under high heat flux by LHD divertor plasma.

Tungsten was sprayed on F82H with blast surface by PS in argon atmosphere. The thickness of the coated layer is about 70μm. Preliminary pulse heat load test showed that joining of the coating is quite good. Detachment of the coated layer did not occur until melting of the F82H substrate. OIM observation showed that no structure change occurred by blast treatment but structure of matrix was modified by heat due to the plasma spray. In addition, fine grains were formed up to 50 μm from boundary in F82H area and grain size of tungsten was about a few μm. Misorientation map calculated using OIM image indicated that strain is formed up to deeper area. Particullary, strain near boundary is high. Distortion is also caused by heat due to the plasma spray. The microstructure and distortion can be recovered by additional heat treatment after the coating of the plasma spray, however, ferrite phase is formed in the interface between W and F82H.

4. Summary

W-coated carbon tile and W-coated RAF/M F82H have been fabricated and have been investigated to apply as the divertor and the first wall/blanket. The W-coated carbon tiles have been exposed to hydrogen plasma discharges in the LHD. No exfoliation and cracks have been observed

on the tiles. Detail surface analyses are now underway. In addition, the W-coated carbon tile is going to be exposed to long duration LHD plasmas to evaluate life time as LHD divertor material. Tungsten has been successfully coated on F82H substrate by plasma spraying technique. Heat flux tests and hydrogen isotope/He irradiation experiment will be carried out on the tiles. In addition, the diffusion behavior of hydrogen isotope will be carried out using imaging plate (IP) technique because tritium transfer from the plasma to the blanket is very important issue.

Acknowledgements

This work was partly supported by the JSPS-CAS Core University Program in the field of Plasma and Nuclear Fusion.

References

[1] K. Tokunaga, N. Yoshida, N. Noda, T. Sogabe, T. Kato,J.Nucl.Mater.258-263(1998)998-1004.

[2] X. Liu, S. Tamura, K. Tokunaga, N. Yoshida, N. Noda, L. Yang, Z. Xu, J.Nucl.Mater. 329-333(2004)687-691.

[3] S. Tamura, X. Liu, K. Tokunaga, Y. Tsunekawa, M. Okumiya, N. Noda, N. Yoshida、J.Nucl.Mater. 329-333(2004)711-716.

[4] K. Tokunaga, N. Yoshida, Y. Kubota, N. Noda, Y. Imamura, T. Oku, A. Kurumada, T. Sogabe, T. Kato, L. Plöchl, Fus. Eng. Des. 49-50(2000)371-376.

[5] K. Tokunaga, R.P. Doerner, R. Seraydarian, N. Noda, Y. Kubota, N. Yoshida, T. Sogabe, T. Kato, J.Nucl.Mater. 313-316(2003)92-96.

[6] K. Tokunaga, M.J. Baldwin, R.P. Doerner, N. Noda, Y. Kubota, N. Yoshida, T. Sogabe, T. Kato, B. Schedler, J.Nucl.Mater. 337-339(2005)887-891.

[7] K. Tokunaga, Y. Kubota, N. Noda, Y. Imamura, A. Kurumada, N. Yoshida, T. Sogabe, T. Kato, B. Schedler, Fus. Eng. Des. 81(2006)133-138.

Proposal of Split and Segmented-type Helical Coils for the Heliotron Fusion Energy Reactor

N. Yanagi [1], K. Nishimura [1], G. Bansal [2], A. Sagara [1] and O. Motojima [1]
1 National Institute for Fusion Science, Toki, Gifu, 509-5292 Japan
2 Institute for Plasma Research, Bhat, Gandhinagar, Gujarat, 382-428 India
E-mail of corresponding author: yanagi@LHD.nifs.ac.jp

Abstract

Configuration optimization is carried out for the heliotron-type fusion energy reactor FFHR. One of the issues is to find sufficient clearance between the ergodic region and the blankets so that direct loss of alpha particles is minimized and the heat flux on the first walls is reduced. It has been found that a fairly large clearance is obtained by employing a low helical pitch parameter for the helical coils and by splitting them in such a way that the current density becomes higher at the inboard side of the torus and lower at the outboard side. In order to construct such complicated helical coils in the continuous manner with a huge size, we propose that half-pitch segments prefabricated with high-temperature superconductors can be assembled. .

Keywords : heliotron, FFHR, configuration optimization, split-type helical coils, high-temperature superconductor, segmented-type helical coils

5. Introduction

Based on the successful progress of fusion relevant plasma experiments in the Large Helical Device (LHD) [1], the conceptual design studies on the heliotron-type fusion energy reactor FFHR are being conducted both on physics and engineering issues [2]. For FFHR, a magnetic configuration similar to that of LHD is employed so that the confined plasma is current-free and the steady-state operation is realized. Though further optimization of the configuration is still being pursued, the present idea gives the major radius of 14-18 m with the toroidal magnetic field of 6-4 T in order to generate 3 GW fusion power. The stored magnetic energy of the superconducting coil system is in the range of 120-150 GJ.

In these studies, the helical pitch parameter, γ, defined by $(m/l)(a_c/R_c)$, for continuous helical coils (having the toroidal pitch number m, poloidal pole number l, average minor radius a_c and major radius R_c), has been chosen to be lower than 1.25 that was adopted for the present LHD. This choice is made for the purpose of reducing the electromagnetic hoop-force on the helical coils while ensuring sufficient blanket space (thickness > 1 m) between the core plasma and the helical coils [3]. The configuration proposed in 2005, FFHR-2m1, has $\gamma = 1.15$, $m = 10$, $l = 2$, $a_c = 3.22$ m and $R_c = 14$ m.

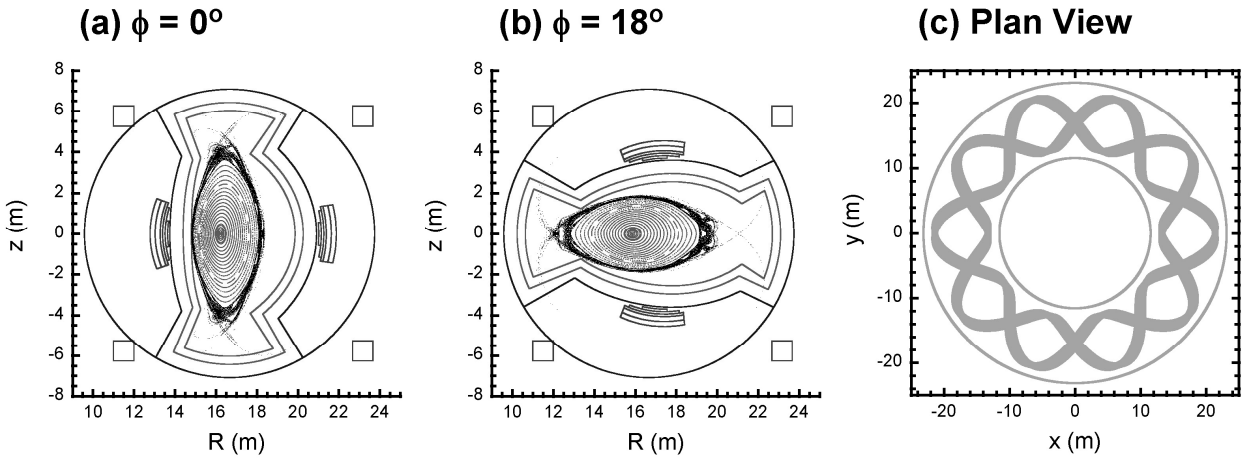

Fig. 1 Vacuum magnetic surfaces of FFHR-2m2 at (a) toroidal angle $\phi = 0°$ and (b) $\phi = 18°$. A plan view of the coil system is shown in (c).

One of the most difficult issues with this configuration is the interference between the ergodic region of magnetic field lines and blankets at the inboard side of the torus. In order to reduce the heat flux on the blankets, "helical x-point diverter (HXD)" concept was proposed [4]. However, this choice gives an extremely high heat flux on the limiter-like structures, and the confinement of alpha particles is deteriorated by cutting the magnetic field lines in the ergodic region where alpha particles are still confined. In this respect, two approaches are being considered to secure more sufficient clearance. One is to enlarge the major radius of the helical coils, and the latest design, FFHR-2m2, gives R_c = 17.33 m and $\gamma = 1.20$. As shown in Fig. 1, the vacuum magnetic surfaces of this configuration are shifted inward, and the magnetic axis is located at R_p = 16.0 m. The inward-shifted configuration is supposed to have good confinement of high-energy particles.

6. Proposal of split-type helical coils

The other approach for ensuring a sufficient blanket space while having a smaller major radius is the modification of the coil configuration. It was previously found that the symmetry of magnetic surfaces is significantly improved, without shifting the magnetic axis inward, by increasing the current density of the helical coils at the inboard side of the torus and decreasing at the outboard side [5]. This can be practically realized by splitting the helical coils in the poloidal cross-section at the outboard side. However, we also observe that the ergodic region is not easily removed from the blanket area at the inboard side by simply splitting the helical coils while maintaining the helical pitch parameter to be around 1.15 or higher. In order to overcome this difficulty, we newly found that a drastically larger clearance is obtained by reducing the helical pitch parameter to be as low as $\gamma = 1.0$ together with splitting. Figure 2 shows an example of the vacuum magnetic surfaces with such a configuration. Here the major and minor radius of the helical coils are 15.0 m and 3.0 m,

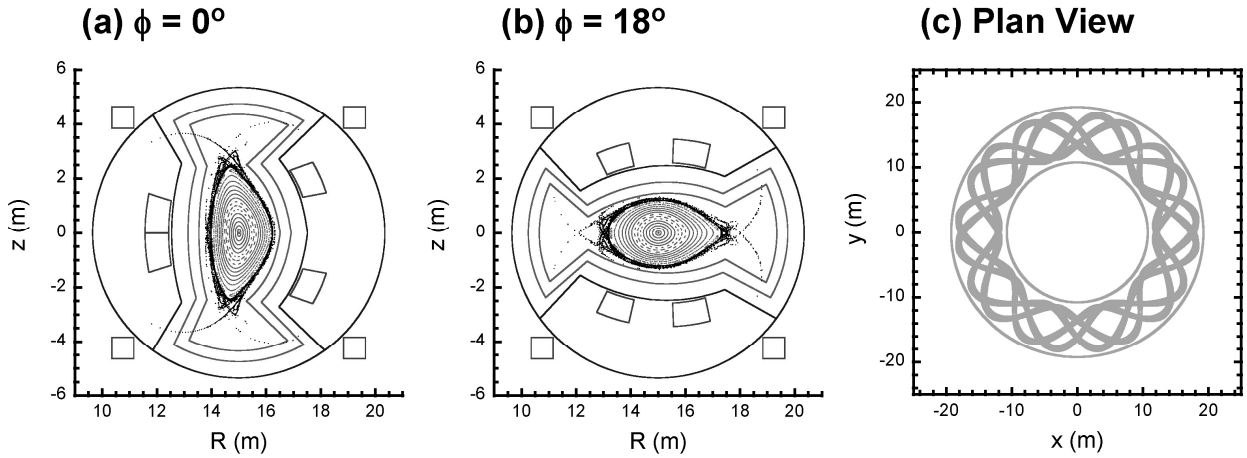

Fig. 2 Vacuum magnetic surfaces of FFHR-2S at (a) toroidal angle $\phi = 0°$ and (b) $\phi = 18°$. A plan view of the coil system is shown in (c).

respectively. The helical pitch modulation parameter α is selected to be +0.1 for this case. As is seen in Fig. 2, the ergodic region is clearly displaced from the blankets.

Here we should note that such a low helical pitch parameter of $\gamma = 1.0$ has never been examined so far, as it has been well known that one is almost in the so-called forbidden-zone for generating magnetic surfaces with a $l = 2$ heliotron configuration [6]. We understand that the low helical pitch parameter is effective for making the ergodic region compact, while the splitting of helical coils at the outboard side ensures larger closed magnetic surfaces. The basic physical properties of this configuration are being examined including the orbits of high-energy particles. The field properties including the plasma beta is our future studies. It should also be stressed that the helical coils experience smaller electromagnetic forces by having a smaller helical pitch parameter, which is one of the fundamental benefits of the FFHR concept.

7. Proposal of segmented-type helical coils

From the engineering viewpoint for realizing the above described split-type helical coils with the huge size of FFHR, here we propose "segmented-type" fabrication [7]. As shown in Fig. 3 (b), we employ a number of joints between the half-pitch segments which are prefabricated separately. Here we also propose that high-temperature superconductors (HTS) are adopted so that the surplus refrigeration power can be effectively used to remove the heat generated by the joints between the segments [8]. The HTS conductor (shown in Fig. 3(a)) are cut in step-like structures and then overlapped and joined with superconducting sides facing each other [7].

Since the HTS conductor has large temperature margin, the temperature rise at a joint may not be a big concern for the cryogenic stability. For a temperature rise of 5 K, the power density of 990 W/m^3 can be allowed, which means that joint resistance of 3 nΩ is even acceptable [7]. On the other

hand, according to the joint resistance measured with single tapes, it is expected that the overall joint resistance of a 100 kA conductor can be as low as 0.06 nΩ, which requires only 300 kW of additional refrigeration power for the entire system. It should be also noted that the helical coils assembled in segments has a further possibility that they can be demountable for maintenance as was originally proposed in [8] with NbTi superconductors and later in [9] with HTS conductors.

8. Summary

A new magnetic configuration for the heliotron-type fusion energy reactor FFHR is proposed by splitting the helical coils in the poloidal cross-section and by employing a low helical pitch parameter of $\gamma = 1.0$, which ensures a large clearance between the ergodic region and blankets. The continuous helical coils with such a complicated three dimensional structure can be assembled by prefabricating half-pitch segments using high-temperature superconductors.

Acknowledgements

The authors are grateful to the FFHR group for valuable discussion and support. This work was partly supported by the JSPS-CAS Core University Program in the field of Plasma and Nuclear Fusion.

References

[1] O. Motojima et al., Fusion Eng. Des., **81** (2006) 2277-2286.
[2] A. Sagara et al., Fusion Eng. Des., **81** (2006) 2703-2712.
[3] S. Imagawa, et al., J. Plasma Fusion Res. SERIES, **5** (2002) 537-540.
[4] T. Morisaki et al., c**81** (2006) 2749-2754.
[5] K. Nishimura and M. Fujiwara, J. Phys. Soc. Japan, **64** (1995) 1164-1171.
[6] K. Uo, Nuclear Fusion, **13** (1973) 661-664 .
[7] G. Bansal et al., Plasma and Fusion Research, **3** (2008) S1049.
[8] K. Uo et al., Proc. 14th Symp. Fusion Techonol., vol. 2 (1986) 1727-1732.
[9] H. Hashizume et al., Fusion Eng. Des., **63** (2002) 449-454.

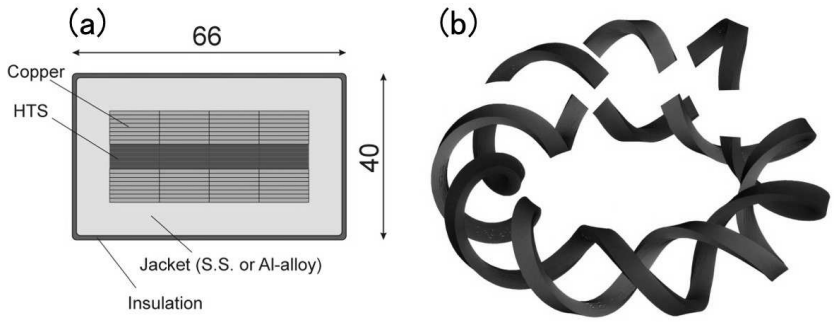

Fig. 3. (a) Design of high-temperature superconductor with 100 kA current capacity and (b) illustrative image of segmented-type helical coils.

Neutronics studies on advanced liquid blanket systems for helical reactor FFHR2

T. Tanaka[1], A. Sagara[1], Z. Li[2], T. Muroga[1], Q. Zeng[3], L. Lu[3], J. Zhang[3], Y. Wu[3]

1 National Institute for Fusion Science, Japan

2 Southwestern Institute of Physics, China

3 FDS Team, Institute of Plasma Physics, Chinese Academy of Sciences, China

Abstract

In the design activity of the helical reactor FFHR2, neutronics investigations have been conducted for four types of Flibe cooled and Li cooled blanket systems. Results of neutnronics investigations based on Monte-Carlo transport calculations indicate that the most important neutronics issue of the original FFHR2 design was significantly high fast neutron fluxes on the superconducting coils due to neutron streaming through the divertor pumping areas. At present, the new Discrete Pumping with Semi-closed Shield (DPSS) concept, which closes most part of the divertor pumping areas, has been proposed to suppress the neutron streaming. Since the accurate simulation of neutron streaming through the openings of the pumping ducts is considered to be essential for the DPSS concept, a collaborative trial of accurate neutronics analysis has been started with the 3-D neutronics calculation system MCAM, which has been developed by the FDS team in the ASIPP and has powerful functions to import CAD geometry data.

Keywords: Helical reactor, FFHR2, Neutron transport, 3-D calculation, MCAM

1. Introduction

Since a neutnronics performance of a fusion blanket system is one of important factors to decide the materials, material compositions, blanket space, component geometry etc. in a fusion reactor, neutronics investigations for advanced liquid cooled blanket systems for the helical reactor FFHR2 have been investigated from the start of the design activity [1, 2]. The original blanket concept for FFHR2 is a Flibe cooled blanket system with solid Be neutron multiplier. The reduced activation ferritic steel of JLF-1 is adopted as a structural material and the original concept is designated as Flibe+Be/JLF-1 blanket. In the design studies of FFHR2, Flibe-STB (STB; Spectral-shifter and Tritium breeder Blanket) concept has been newly proposed to suppress irradiation damages on the structural material with thick carbon armor [3]. Concepts of Li/V-alloy and Flibe/V-alloy blankets adopting vanadium alloy as the structural material have been also studied as the alternatives for the higher temperature operation of FFHR2 [4]. Progress in the neutronics studies on the four types of advanced liquid blanket systems for FFHR2 has been introduced in the presentation.

2. Optimization of compositions and thicknesses of blanket layers

In the design activity of FFHR2, parameters related to the neutronics studies are the neutron wall load of 1.5 MW/m^2 and blanket space of 1.2 m. These parameters indicate that the 14 MeV neutron flux from the core plasma is 6.7 x 10^{13} n/cm^2/s and both tritium fuel breeding and radiation shielding are required to be achieved in the blanket layer of <1.2 m in thickness. From the start of the FFHR2 design activity, the feasibility of the tritium breeding and radiation shielding has been studied with neutron and gamma-ray transport calculations using the ANISN or MCNP codes. The calculation geometry is a 1.5-D cylindrical or 3-D simple torus model as shown in Fig. 1. After optimizations of the material compositions and layer thicknesses, the compatibilities between the tritium fuel breeding and radiation shielding have been achieved for all the four blanket concepts, i.e. Flibe+Be/JLF-1, Flibe-STB, Li/V-alloy and Flibe/V-alloy, with the total blanket thicknesses of 0.9-1.2 m. The calculated local tritium breeding ratios (local TBRs) were 1.23-1.34 and fast neutron fluxes of >0.1 MeV were attenuated to <~1.0 x 10^{10} n/cm^2/s at outside of the radiation shield, which is the design target of FFHR2 to avoid critical irradiation damages on the superconducting magnet.

3. Neutronics issues in helical reactor

For understanding of neutronics features in FFHR2, simulation of the helical shaped components has been required in the neutron and gamma-ray transport calculations. A three dimensional neutronics calculation system has been constructed for quick generation of the helical component geometry data for the MCNP code and for 3-D visualization of calculated results [5]. Geometries of helical shaped components in the FFHR2 design such as helical coils, breeding and shielding blankets can be defined approximately by simple numerical expressions. In the process using the calculation system, coordinates of the 3-D helical components were calculated from the design drawing of the vertical cross section of FFHR2 according to the numerical expressions. Since this approach could generate 3-D geometry data with a small amount of effort, the system were used successfully for improvement of the tritium breeding and shielding performances by the quick feedback between the neutronics evaluations and design modifications.

By using the calculation system, the coverage ratio of the original FFHR2 blanket configuration

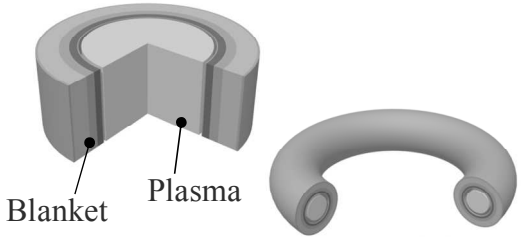

Fig. 1 Cylindrical and simple torus model for optimization of material compositions and layer thicknesses

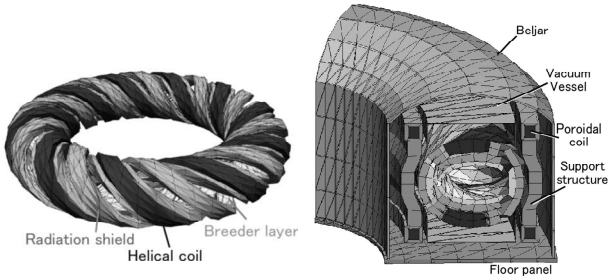

Fig. 2 Three-dimensional neutronics calculation geometry to simulate helical components of FFHR2 [5].

was estimated to 60-70% and the total TBR was 0.82 for the Flibe+Be/JLF-1 blanket due to significant neutron leakage through the divertor pumping areas. After modifying the blanket configuration according to the evaluations, the coverage increased to ~80 % and total TBR of 1.08 was obtained. The total TBRs for the Flibe-STB, Li/V-alloy and Flibe/V-alloy were 0.97-1.05. The results indicate that all of the four blanket systems proposed for FFHR2 would achieve the total TBRs of >1.0 by further design efforts.

The most important neutronics issue in the 3-D calculations was neutron streaming through the divertor pumping areas at outer side of the torus. The streaming neutrons were reflected by the support structures and the fast neutron flux at the backside of the helical coils reached ~5 x 10^{11} n/cm^2/s, while the design target is 1.0 x 10^{10} n/cm^2/s. To suppress the neutron streaming, the new Discrete Pumping with Semi-closed Shield (DPSS) concept has been supposed based on the neutroncs analysis. Since the most of the divertor pumping areas are closed in the DPSS concept, the preliminary analysis indicated that the fast neutron flux at the superconducting coils would be suppressed close to the design target of 1.0 x 10^{10} n/cm^2/s. However, more accurate neutronics analyses are required to estimate the impact of the neutron streaming through the discrete pumping ducts. It is considered that import of CAD data into neutronics calculations are effective and required especially for simulation of the neutron streaming.

4. New collaborative trial for further neutronics studies

For the neutronics analysis using the CAD data of FFHR2, complicated 3-D geometry data need to be converted into input data for a neutronics calculation code. A large amount of efforts will be required for the development of a powerful conversion software program and data processing. The FDS team in ASIPP has been conducting the development of the conversion software MCAM (Monte Carlo Automatic Modeling) for many years and the powerful functions of not only data conversion but also visualization and data processing have been already demonstrated in the ITER neturonics calculation model etc [6]. A collaborative trial of converting the complicated FFHR2 CAD data to input data for the MCNP code has just been started with the MCAM system.

The CAD data of FFHR2 have already been imported in the MCAM system as shown in Fig. 3. The technical issue in the data conversion is processing of the complicated spline surfaces of the FFHR2 components. As to the helical coils, conversion to input data for the MCNP code has been implemented successfully and the neutron transport calculations have been performed. At present, further tests and modification of the system are underway in the FDS team to convert the full model of FFHR2.

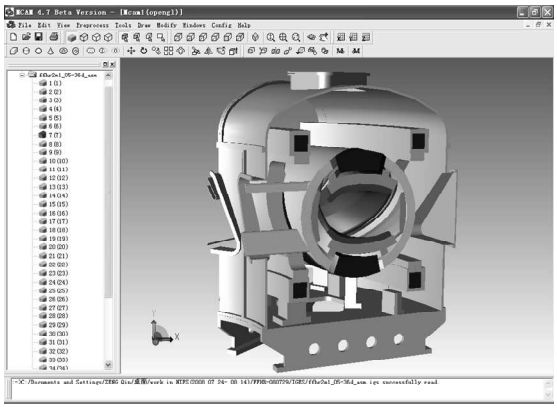

Fig. 3. FFHR2 CAD data imported to MCAM system. Conversion to input data for the MCNP calculation code is underway at the FDS team in ASIPP.

In the collaborative study with the MCAM system, accurate analysis and improvement of neutronics performances of FFHR2 with the DPSS concept can be performed by focusing on the impact of the neutron streaming through the pumping ducts. The integrated functions for spline surface processing will be installed to the MCAM system through the tests with the FFHR2 CAD data and will be released in the new version of the MCAM system. The validation of the analysis is planned by comparison with our previous results simulating the helical component geometry.

5. Summary

Neutronics studies for the helical reactor FFHR2 have been conducted from the start of the reactor design activity. In the present studies simulating the 3-D helical geometry, most important neutronics issue is neutron streaming through divertor pumping areas and improvement of the shielding performance with the DPSS concept has been proposed recently. For the analysis of neutronics performances of the DPSS concept, accurate neutron transport calculations through the pumping ducts is required to be performed by using the FFHR2 CAD data. A new collaborative trial for importing the FFHR2 CAD data into neutronics analysis has been started with the Mote Carlo automatic modeling system MCAM developed by the FDS team in ASIPP.

Acknowledgements

This collaboration work was supported by JSPS-CAS Core University Program.

References

[1] A. Sagara *et al.*, Fusion Engineering and Design **29** (1995) 51-56.

[2] H. Yamanishi *et al*., Fusion Engineering and Design **41** (1998) 583-588.

[3] A. Sagara *et al.*, Nuclear Fusion **45** (2005) 258-263**.**

[4] T. Tanaka, T. Muroga, A. Sagara., Fusion science and technology **47** (2005) 530-534.

[5] T. Tanaka, A. Sagara, T. Muroga, M.Z. Youssef, Nuclear Fusion **48** (2008) 035005.

[6] Y. Li, L. Lu, A. Ding, H. Hu, Q. Zeng, S. Zheng and Y. Wu, Fusion Engineering and Design **82** (2007) 2861-2866.

Pb-17Li Acoustic Properties for Ultrasonic Doppler Velocimetry

T. Kunugi[1], Y. Ueki[1], T. Yokomine[2], M. Hirabayashi[3], T. Hinoki[4], Shimoda[4] and K. Ara[3]
1 Dept. of Nuclear Engineering, Kyoto University, Kyoto, 606-8501 Japan
2 Dept. of Engineering Science, Kyushu University, Fukuoka, 816-8580 Japan
3 O-arai Engineering Center, Japan Atomic Energy Agency, Ibaraki, 311-1393 Japan
4 Institute of Advanced Energy, Kyoto University, Uji, Japan
E-mail of corresponding author: kunugi@nucleng.kyoto-u.ac.jp

Abstract

In lead-lithium (Pb-17Li) liquid metal blanket concept, Pb-17Li eutectic alloy circulates both as breeder and coolant under a strong plasma-confining magnetic field, experiencing magneto-hydro-dynamic (MHD) force: Lorentz force. The present paper focuses on Ultrasonic Doppler Velocimetry (UDV) as an effective diagnostic to measure the Pb-17Li flow in the presence of the strong magnetic field. This paper describes a favorable wetting material for high-temperature transducer and the acoustic property database of Pb-17Li eutectic alloy. The material analyses after high temperature measurements are performed to discuss the durability of titanium transducer.

Keywords : Pb-17Li, Acoustic properties, Ultrasonic Doppler Velocimetry

1. Introduction

In a liquid metal fusion blanket concepts, lead-lithium eutectic alloy (Pb-17Li) circulates as a breeder (e.g. HCLL blanket [1]), or both as a breeder and a coolant (e.g. DCLL blanket [2]). Especially in the DCLL blanket, full turbulence closure modeling for MHD flows combined with buoyancy effects is very difficult [3]. Prototypic physical experiments have been required to study the major multiple effects, but have not been conducted yet in spite of their own significance.

In order to comprehend the Pb-17Li flow combined with buoyancy force in a strong magnetic field, Ultrasonic Doppler Velocimetry (UDV) was expected as an appropriate diagnostic. The UDV is based on a pulsed ultrasonic echography together with detection of the instantaneous Doppler shift frequency [3]. The UDV is a non-invasive flow measuring technique applicable to liquid metals.

The UDV technique has not been applied to Pb-17Li flow. An ultrasonic transducer should be temperature-resistant, and also needs to have favorable ultrasonic transmission at the material interface between liquid Pb-17Li and the surface material of the transducer. The UDV requires a sound speed of the target fluid to evaluate the time of flight (TOF) of a pulsed ultrasonic. In

addition, the acoustic impedances, i.e., the product of the density and the sound speed, characterize the ultrasonic behaviors at the material interface: acoustic transmission, reflection and refraction.

2. Ultrasonic transmission test

Firstly, the ultrasonic transmission test was conducted. The insufficient wetting of Pb-17Li against the transducer material surface prevents the ultrasound from transmitting efficiently at the material interface. In order to clarify the transmission characteristics, the ultrasonic transmission test was performed. Figure 1 shows the ultrasonic transmission test apparatus. Tests were conducted under an Ar-filled glove box. Titanium (Ti) was used as the transducer surface material. Titanium has the favorable compatibility with the oscillator at high temperature because the thermal expansion coefficient of Ti is comparable with the oscillator material ($LiNbO_3$).

The holder was filled with the Pb-17Li. The transducers were connected to the ultrasonic emitter-receiver, and the pulsed ultrasonic waves were emitted into the liquid Pb-17Li through the test material. Ti plate was wetted at 420 degree C for around 10 hours. The temperature-resistant transducers were fixed on the test materials by the connectors. The transducer (IHI Inspection & Instrumentation Co., Ltd.,) was endurable up to at 500 degree C. The main emission frequency was 4 MHz. At the beginning of the Pb-17Li wetting, the ultrasonic transmission at the interface was sufficient for evaluating the signals through the Pb-17Li. Figure 2 shows the ultrasonic transmission signal through the stagnant Pb-17Li.

3. Acoustic properties of Pb-17Li

Figure 3 shows the apparatus to evaluate the sound speed in the Pb-17Li. The material of the apparatus was SUS304. The Ti high-temperature transducers were attached to the apparatus, so that the distance between the two transducers was precisely 100.0 mm. The temperature of the Pb-17Li was measured by the thermocouple inserted into the vertical hole and was adjusted by a temperature controller. The transducer was endurable up to around 500 degree C. The main emitting frequency was 4 MHz. The ultrasonic waves emitted into the liquid Pb-17Li, travelling through it and received by the other transducer. The received signals were recorded by a digital oscilloscope. Before the measurement of the Pb-17Li, a preliminary check was performed using an ethanol at room temperature. The measured sound speed in the ethanol was within 1% error compared to the reference value. Figure 3 also shows the schematic view of the sound speed measurement. The transmission time was evaluated by the time difference between the transmission paths A and B, since the shoe lengths of two transducers were equal. The sound speed in the Pb-17Li was evaluated by the pulsed ultrasonic transmission path-length between the emitter and the receiver divided by the TOF of pulsed ultrasonic waves. Figure 4 shows the dependency of the sound speed in the Pb-17Li on temperature. The sound speed in the Pb-17Li has linearity to temperature, and thus the

sound speed was evaluated by the linear approximation method. The experimental correlation equation relating the sound speed in the Pb-17Li, C_{PbLi}, to the liquid temperature, T ($240 < T\,[C] < 510$) is given as follows;

$$C_{PbLi}\,[m/s] = 1876\text{-}0.3058\,T \quad (1)$$

Using the Pb-17Li density [6], the acoustic impedance of Pb-17Li, $Z_{PbLi} = \rho_{PbLi}\,C_{PbLi}$, is given as follows;

$$Z_{PbLi}\,[kg/m^2\,s] = 1.87\times10^7 - 6.20\times10^3\,T + 0.513\,T^2 \quad (2)$$

The horizontal error bar shows the temperature measuring error by the thermocouple. The vertical error bar shows the sound speed measuring error.

4. Effects of surface structure at liquid-wall interface

Two material analyses were conducted to clarify the surface characteristics effects on the ultrasonic transmission. One was the surface roughness measurement using an atomic force microscope (AFM). The other analysis was a scanning electron microscopic (SEM) observation with an energy dispersive spectrometer (EDX). After the transmission test, the Pb-17Li was adherent to the Ti test plate. The Pb-17Li adherents were removed chemically using the mixture solution of an acetic acid, the ethanol and a hydrogen peroxide (1:1:1) until the test plate weight kept constant. Firstly, the wetted surface was observed by an optical microscope, and the surface roughness and the submicron structure were measured using the AFM. The arithmetic roughness of the wetted surface increased around 700% compared to the original surface (14.84 nm before Pb-17Li exposure, 100.8 nm after the exposure). The other Ti test plate after the ultrasonic transmission test was set in an epoxy resin and cut it before polishing the cutting surface. A cross-section of resin-(Pb-17Li)-substrate interface was observed using the SEM with the EDX. Figure 5 shows the SEM images of the cross-sectional Ti plate, Pb element mapping, and Ti element mapping. It showed the Pb-17Li was adherent to the Ti surface, but no micro-scale corrosion was observed. Taking the two results into consideration, the Pb-17Li corrosion effects were limited to the submicron scale in the time scale for achieving sufficient ultrasonic transmission for the UDV measurement. From the point of view of transducer durability, it is favorable to achieve the sufficient transmission at the beginning of the Pb-17Li exposure, and not to have serious damages in time scale for achieving the sufficient transmission.

5. Conclusion

The conclusions of this study regarding the development of Pb-17Li flow speed measurement using high-temperature UDV technique are as follows:

I. Titanium has favorable sound characteristic to Pb-17Li eutectic alloy. It is confirmed that Titanium high-temperature transducer is suitable for UDV measurement of lead-lithium flow.

II. The sound speeds in Pb-17Li were measured in the temperature range from 240 up to 510 degree C. The sound speed in Pb-17Li shows the linearity in temperature, as well as other liquid metals. The experimental correlations of the two acoustic properties were obtained.

III. Pb-17Li corrosion thickness of Titanium was limited to submicron meter after the ultrasonic transmission for UDV measurement. The durability of titanium high-temperature transducer was confirmed in the range of the present experimental conditions.

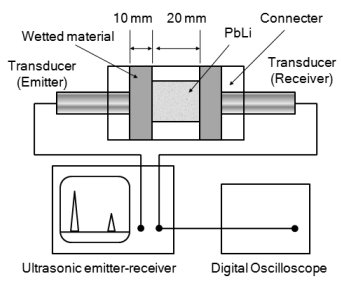

Fig. 1 Ultrasonic transmission test apparatus

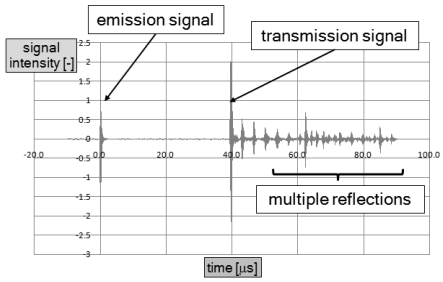

Fig. 2 ultrasonic transmission signal through Pb-17Li

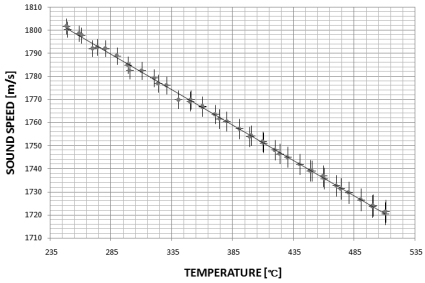

Fig.4 Dependency of sound speed in the Pb-17Li on temperature

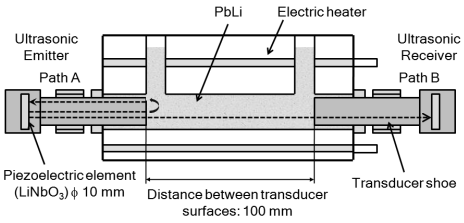

Fig. 3 Sound speed measurement apparatus

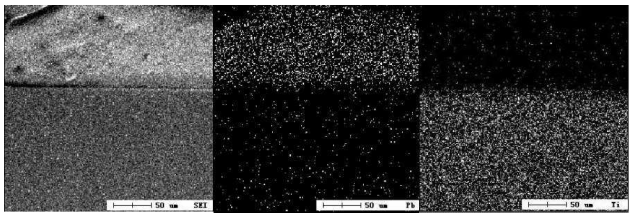

Fig.5 SEM images of cross-sectional Ti plate

Acknowledgements

The authors were grateful for the great financial support from the Japanese Ministry of Education, Culture, Sports, Science and Technology via the TITAN project. A part of this research was conducted under the Collaboration Program of the Laboratory for Complex Energy Processes, Institute of Advanced Energy, Kyoto University. This work was partly supported by the JSPS-CAS Core University Program in the field of Plasma and Nuclear Fusion.

References

[1] G. Rampel et al., Fusion Engineering and Design, **75-79**, (2005), 917-922

[2] C. P. C. Wong et al., Fusion Engineering and Design, **81**,(2006), 461-467

[3] S. Smolentsev et al., "Characterization of key magnetohydrodynamic phenomena in PbLi flow for the US DCLL blanket", Fusion Eng. And Design, in press

[4] Y. Takeda, Experimental Thermal and Fluid Science, **10**, (1995), 444-453

[5] B. Shultz, Fusion Engineering and Design, **14**, (1991), 199-205

Annihilation behavior of irradiation defects produced by 14 MeV or thermal neutron irradiation in ternary lithium oxides

Yasuhisa Oya[1], Hirotada Ishikawa[1], Sachiko Suzuki[1], Haibo Liu[2], Tianyong Luo[2], Kaiming Feng[2] and Kenji Okuno

[1]Radioscience Research Laboratory Faculty of Science, Shizuoka University, 836 Ohya, Suruga-ku, Shizuoka 422-8529, Japan

[2]Southwestern Institute of Physics, Chengdu, China

E-mail of corresponding author: syoya@ipc.shizuoka.ac.jp

Abstract

The differences on the annihilation behavior of irradiation damages between 14 MeV and thermal neutrons in ternary lithium oxides were studied by means of ESR. It was found from isothermal annealing experiments that annihilation process of irradiation defects consists of two processes, namely the fast and the slow annihilation processes. Comparing to the experimental results for the thermal neutron-irradiated samples, the activation energies of the slow annihilation process were significantly different. This result would relate to the density of irradiation defects, which clearly depend on the contribution of the recoil particles produced by nuclear reaction for the introduction of irradiation damages

Keywords: Tritium breeding materials, 14 MeV neutron, Thermal neutron, Irradiation damage, Electron Spin Resonance

1. Introduction

In blanket systems for D-T fusion reactors, tritium breeding materials are introduced, where energetic tritium is produced by the nuclear reaction. Especially, tritium detrapping behavior from trapping sites such as irradiation defects would strongly correlate to tritium inventory. It is well known that irradiation defects are generated in the tritium breeding materials by the recoil particles. It has been reported that such irradiation defects could affect the tritium release processes. Okuno et al. reported that the chemical states of tritium in neutron-irradiated Li_2O correlated with the annihilation process of F^+-center, which is oxygen vacancy occupied by one electron [1]. In our previous studies, it was revealed that tritium release behavior associated with annihilation behavior of irradiation defects for ternary lithium ceramics; tritium release was triggerd with annealing F^+-center or E'-center [2-11]. In D-T fusion reactors, 14 MeV neutrons are also irradiated into the tritium breeding materials and various irradiation defects could be induced into those materials during the following processes; (1) collision processes with energetic tritons and α particles which are generated by $^6Li(n, \alpha)T$ and $^7Li(n, n'\alpha)T$, (2) collision processe with energetic neutron, (3) cascade scattering following collision processes of neutron. These irradiation defects are also expected to interact with the produced tritium. Therefore, the present study has been focused on the annihilation behavior of irradiation defects produced by 14 MeV neutron irradiation.

2. Experiments

Lithium ortho-silicate (Li_4SiO_4) provided by FZK, lithium aluminate ($LiAlO_2$) pebbles purchased from Kawasaki Heavy industries Ltd. and sintered lithium meta-silicate (Li_2SiO_3) purchased from Aldrich Co. were used as samples. All samples were preheated at 1173 K for 3 hours under a reduced pressure of He atmosphere in quartz tube in order to remove hydroxides. After heating, the tubes were sealed. Thereafter, the samples were irradiated with 14 MeV neutrons at ambient temperature using the Fusion Neutronics Source (FNS) at the Japan Atomic Energy Agency (JAEA). The 14 MeV neutron fluence was 6.2×10^{14} n cm^{-2}. The isothermal annealing of the 14 MeV neutron-irradiated samples followed. After each annealing step, the samples were immediately cooled to 77 K and the annihilation of irradiation defects introduced by neutron irradiation were measured by means of Electron Spin Resonance (ESR). The temperature ranges were 400-600 K in accordance with the results of isochronal annealing experiments which were reported previously [2, 7] and those experiments were continued over 8 hours.

3. Results

Figure 1 shows typical ESR spectra for 14 MeV or thermal neutron-irradiated Li_4SiO_4. The ESR spectrum for non-irradiated Li_4SiO_4 is also shown as reference [2].

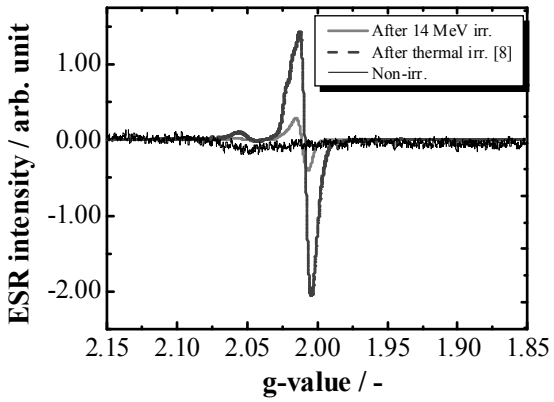

Fig. 1 ESR spectra for 14 MeV or thermal neutron-irradiated Li_4SiO_4. ESR spectrum for the sample without neutron irradiation is also shown as reference[2].

The peak analysis for all the samples revealed that the *g*-values for these peaks were almost the same. The F^+-center or E'-center was mainly formed but oxygen radicals were also observed. To evaluate the difference between 14 MeV and thermal neutron irradiations, the production ratios of the F^+-center or E'-center and the densities of irradiation defects which would influence on the recovery of those defects were estimated. From these estimations, it was found that the production ratios of the F^+-center or E'-center and the densities of irradiation defects for 14 MeV neutron-irradiated samples were less than those for thermal neutron-irradiated ones, suggesting that these results would affect the kinetics for the annihilation of irradiation defects.

Isothermal annealing experiments were performed to evaluate the activation energy for the annihilation of irradiation defects. A typical result of an isothermal annealing experiment at 573 K for 14 MeV neutron-irradiated Li_4SiO_4 is shown in Fig. 2.

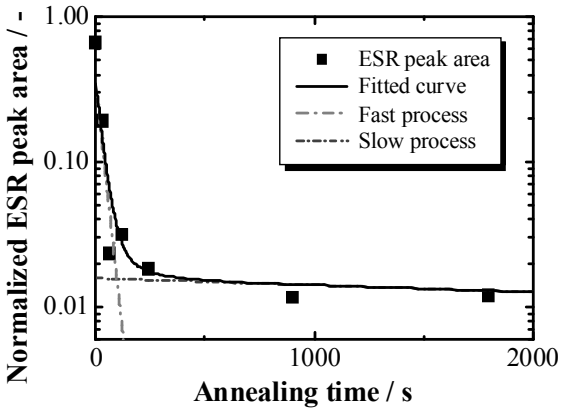

Fig. 2 Isothermal annealing curve at 573 K with the fitted curve from equation (1).

This figure shows that the annihilation processes of irradiation defects consist of two processes, namely, the fast and the slow annihilation processes, which are consistent with the previous studies for the thermal neutron-irradiated samples and those tendencies can be also observed for 14 MeV neutron-irradiated Li_2SiO_3 and $LiAlO_2$. The annihilation kinetics can be expressed by the combination of two first-order reactions as follows;

$$[def] = [f]^0 \exp(-k_f t) + [s]^0 \exp(-k_s t) \qquad (1)$$

where [*def*] means the number of all irradiation defects detectable by ESR at annealing time t, $[f]^0$ and $[s]^0$ are the initial number of irradiation defects for fast and slow processes, respectively. From these hypotheses, rate constants for these annihilation processes, k_f and k_s, were determined and the activation energies for these processes, E_f and E_s, were also determined by Arrhenius plots. The activation energies for the fast and slow processes are summarized in Table.

Table Activation energies of the fast and the slow annihilation processes for the 14 MeV and the thermal neutron-irradiated Li_4SiO_4, Li_2SiO_3 and $LiAlO_2$.

$LiAlO_2$	Fast process	Slow process
14 MeV neutron	0.34±0.01 eV	0.64±0.02 eV
Thermal neutron	0.35±0.03 eV	1.1±0.1 eV
Li_2SiO_3	Fast process	Slow process
14 MeV neutron	0.12±0.01 eV	0.47±0.03 eV
Thermal neutron	0.12±0.02 eV	0.63±0.01 eV
Li_4SiO_4	Fast process	Slow process
14 MeV neutron	0.13±0.05 eV	0.39±0.03 eV
Thermal neutron	0.12±0.07 eV	0.56±0.01 eV

The activation energies for the fast process, E_f of the 14 MeV neutron-irradiated sample are almost the same as that of the thermal neutron-irradiated one. However, the activation energies for the slow process, E_s for the 14 MeV neutron irradiation are smaller than those for the thermal neutron irradiation. For the fast annihilation process, the present results suggested that this process might result from migration of electrons which were trapped in the potential valley to the various

irradiation defects and that there was no correlation with tritium release. According to the ESR experimental results, the fast process caused the complete annihilation of irradiation defects except for F^+-center or E'-center. In the slow annihilation process, the F^+-center or E'-center were annihilated for both of the 14 MeV and the thermal neutron-irradiated samples. It is thought that the F^+-center or E'-center are annihilated by recovering O^- with diffusion of O^- and at this time tritium release is initiated. However, the activation energies for the 14 MeV neutron-irradiated samples were clearly different from those for the thermal neutron-irradiated ones. As mentioned above, the densities of irradiation defects were quite different between 14 MeV and thermal neutron-irradiated ones, indicating that the recovery of O^- to F^+-center or E'-center for the thermal neutron-irradiated samples require a higher activation energies since the various defects would remain in the vicinity of the diffusion path of O^-.

4. Summary

The annihilation behaviors of irradiation defects produced by 14 MeV neutron irradiations for $LiAlO_2$, Li_2SiO_3 and Li_4SiO_4 were compared to those produced by thermal one. The annihilation of irradiation defects consisted of two processes, namely, a fast and a slow annihilation process. Compared to thermal neutron-irradiated samples, E_f are almost the same while E_s for the 14 MeV neutron irradiations are smaller than those for the thermal ones. The fast annihilation process was attributed to the annihilation of various irradiation defects by migration of trapped electrons in the potential valley. The slow annihilation process was contributed to the annihilation of F^+-center or E'-centers and the difference of E_s was attributed to the influence of the difference in the densities of irradiation defects, that is, the recovery of O^- for the thermal neutron-irradiated sample requires a higher activation energy compared to the 14 MeV neutron irradiated case.

Acknowledgements

This work is supported by JSPS-CAS CUP program and the collaboration program of Fusion Neutronics Source, Japan Atomic Energy Agency. The work was partly carried out using an instrument at the Center for Instrumental Analysis of Shizuoka University.

References

[1] K. Okuno and H. Kudo, J. Nucl. Mater. **138**(1986)31-36.
[2] Y. Nishikawa et al., J. Nucl. Mater. **367-370**(2007)1371-1376.
[3] Y. Morimoto et al., Fus. Technol. **39**(2001)634-638.
[4] S. Akahori et al., J. Radiochem. Nucl. Chem. **255**(2003)257-260.
[5] M. Oyaidzu et al., J. Fus. Sci. Tec. **48**(2005)638-641.
[6] M. Oyaidzu et al., J. Nucl. Mater. **329-333**(2004)1313-1317.
[7] M. Oyaidzu et al., Fus. Eng. Des. **81**(2006)583-588.
[8] M. Oyaidzu et al., J. Radioanalytical Nucl. Chem. **272**(2007)657-660.
[9] M. Oyaidzu et al., Fus. Sci. Tec. **52**(2007)1002-1006.
[10] M. Oyaidzu et al., J. Nucl. Mater. **375**(2008)1-7.
[11] H. Ishikawa et al., Fus. Sci. Tec. **54**(2008)127-130.

PWI Study for LHD Based Upon Material Probe

Y. Nobuta[a] , N. Ashikawa[b], H. Yagihashi[a], Y. Yamauchi[a], T. Hino[a], S. Masuzaki[b], K. Nishimura[b], A. Sagara[b], N. Oyabu[b], N. Noda[b], A. Komori[b], O. Motojima[b] and LHD Experimental Group[b]

1 Laboratory of Plasma Physics and Engineering, Hokkaido University, Sapporo, 060-8628 Japan
2 National Institute for Fusion Science, Toki-shi, Gifu-ken, 509-5292 Japan
E-mail of corresponding author: y-nobuta@eng.hokudai.ac.jp

Abstract

In order to investigate the change of wall surfaces and plasma wall interactions, material probes were installed at the inner walls of LHD along the toroidal and poloidal directions in the 10th experimental campaign. Impurity deposition, erosion thickness and gas retention were examined for material probes. Boron deposition, which was caused by boronization, was observed to be dominant on the surface of probes in the vicinity of glow discharge anodes. The retained amounts of discharge gases and eroded thickness were large near the glow anodes, since the incident flux near the anode was large. Comparing with data of previous campaigns, it was found that the hydrogen retention was increased with the total time of glow discharge of each campaign.

Keywords : LHD, retention, erosion, deposition, hydrogen

1. Introduction

It is quite important for improvements of plasma performance to deepen the understanding of the plasma-wall interaction (PWI). For this reason, the wall condition needs to be investigated. Material probe, which means a small sample installed on the plasma-facing wall, is useful for learning about wall conditions, such as deposition, erosion and gas retention. Material probes have been systematically installed on the plasma-facing wall of LHD in each experimental campaign from the first experimental campaign conducted in 1998. Results obtained from the analyses by the material probes were referred to in the next experimental campaigns, and contributed to improving the wall conditioning technique and to understanding of the plasma-wall interactions in LHD [1-4]. In the 10^{th} experimental campaign, ten material probes were installed at the plasma-facing wall along toroidal direction to investigate the impurity deposition, gas retention and erosion. In this study, these results are briefly presented.

2. Experimental

In LHD, the first wall and the divertor target tiles were made by 316L stainless steel and graphite, respectively. In the 10th experimental campaign, about 5500 shots of hydrogen discharges were carried out. Before the series of main discharge experiments on each day, glow discharge cleanings using helium, hydrogen, neon and argon were conducted using two graphite anodes. In glow discharges, total pressure was ~1 Pa, discharge current 10 A at each electrode and voltage 210-410 V [5]. In order to reduce oxygen level in core plasma, boronization using glow discharge with a mixture of helium (90 %) and diborane (10 %) gas was conducted two times during the 10th experimental campaign.

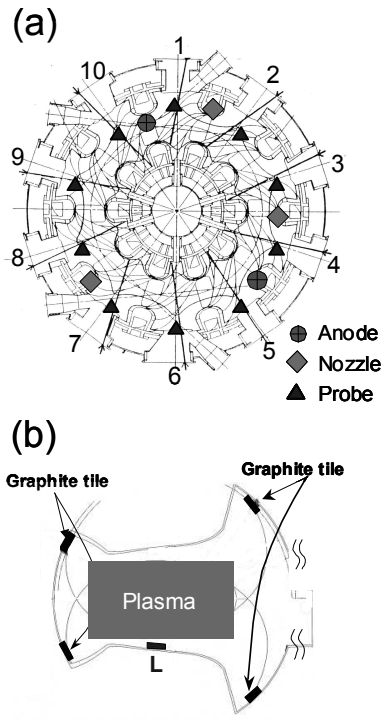

Fig.1. Material probe positions placed along toroidal direction (a) and poloidal position (b).

Figure 1 shows the positions of the material probes along the toroidal direction (a) and the poloidal direction (b). In the 10th experimental campaign, the material probes were located at each toroidal sector, namely there were ten probe positions. The poloidal position of these probes was at the bottom of the first wall (Fig.1 (b)). In every probe position, both stainless steel and silicon probes were set in the sample holder. The size of each probe was 10x20x1 mm. The number of toroidal sectors and the positions of both anodes and diborane-inlet nozzles are also shown in Fig.1 (a). The positions of the two anodes were at the 4.5U and 10.5U ports, and the diborane-inlet nozzles were at the 1.5L, 3.5L and 7.5L ports. After the 10th experimental campaign, the probes were extracted from the vacuum chamber, and the depth profile of atomic composition and the retained amounts of discharge gases were analyzed by Auger electron spectroscopy (AES) and thermal desorption spectroscopy (TDS), respectively.

3. Results

The silicon probes placed along the toroidal direction was partially coated by boron film, and the boron film was partly covered by stainless steel mask. A method of preparing the boron-coated silicon probe was reported elsewhere [6]. In order to measure the eroded thickness, the mask was removed after the campaign, and then the change of height was

measured by using a surface profiler using a contact needle with a height resolution of 10 nm. Fig.2 shows the eroded thickness of the pre-coated boron film on the silicon probe. In this figure, the positions of the glow anodes are also shown. One can see that the eroded thickness was larger near the anodes. At sector 5, the pre-coated boron film disappeared, which means that the eroded thickness was at least 500 nm. The results are due to larger incident flux during glow discharge and suggest that erosion of the first wall in LHD occurred mainly during glow discharge.

Fig.3 shows the thickness of boron film deposited during boronization. The thickness significantly depended on toroidal location. Thick boron film was observed in the vicinity of the anodes. Diborane was easily dissociated and/or ionized near the anodes during glow discharge due to large current density. This might be the reason for the large deposition near the anodes. For the probes with thick boron film, the boron concentration was 60-90 at.%. The boron film contained oxygen with a concentration of 1-5 at%, indicating the boron film gettered oxygen during boronization.

Fig.4 shows the retained amounts of hydrogen of stainless steel probe. Data of the 7-9th experimental campaigns are also shown in this figure for reference. The hydrogen retention close to the anodes was a factor of 2-10 larger than that far from the anodes due to large incident flux near the anodes during glow discharge. The results indicate that hydrogen was accumulated in the first wall mainly during glow discharge. Comparing with previous experimental campaigns, it was found that the retained amounts of hydrogen have been reduced between each experimental campaign. This might be caused by a decrease of the total time of glow discharge using hydrogen (7th: 700 h, 8th: 500 h, 9th: 290 h, 10th: 250 h). In LHD, glow discharge cleaning using helium has been conducted. It is reported that helium glow discharge cleaning is effective on reducing hydrogen retained in stainless-steel wall [7]. The total time of glow discharge using helium has increased

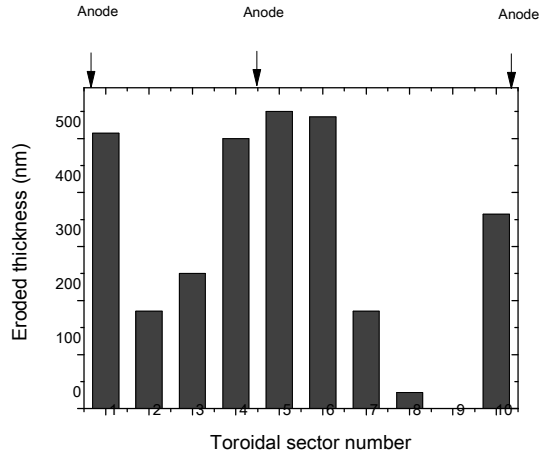

Fig.2 Eroded thickness of pre-coated boron film mounted in toroidal direction.

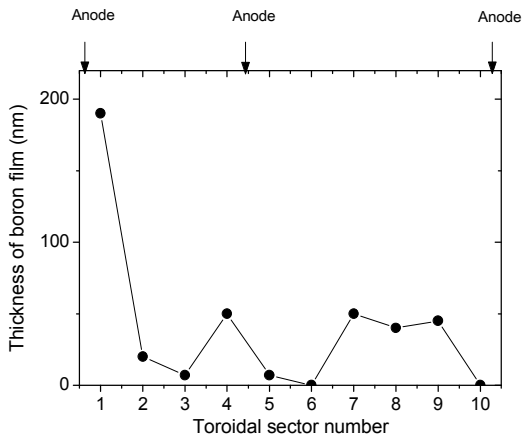

Fig.3 Thickness of boron film deposited during boronization.

with experimental campaign (7th: 100 h, 8th: 100 h, 9th: 240 h, 10th: 400 h). This might also be the reason of the reduction of hydrogen retention.

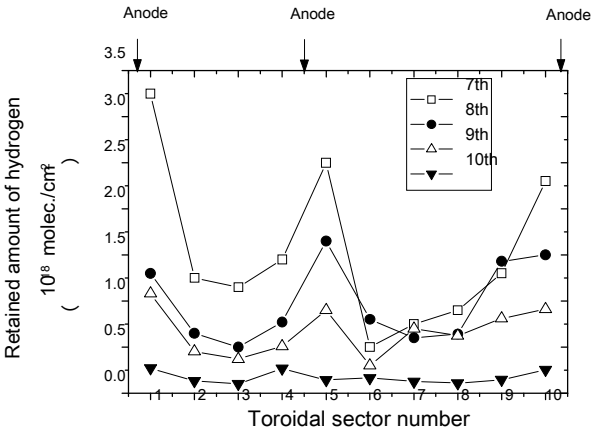

Fig.4 Retained amounts of hydrogen in stainless steel probes along toroidal direction in 7th-10th campaign.

4. Summary

Material probes were installed on ten toroidal locations in LHD. Retained amounts of hydrogen, eroded thickness and boron film thickness were measured after each campaign. The thickness of the boron film deposited during boronization was observed to be large at the wall close to the anodes. Retained amount of hydrogen and eroded thickness of pre-coated boron film were large near the anodes. These results suggest that hydrogen retention and erosion in LHD occurred mainly during glow discharge due to large incident flux. These results are useful for understanding of wall conditions and the plasma wall interaction in LHD.

Acknowledgements

This work was supported by the Collaboration Study Program in National Institute for Fusion Science. This work was partly supported by the JSPS-CAS Core University Program in the field of Plasma and Nuclear Fusion.

References

[1] T. Hino et al., J. Nucl. Mater 313–316 (2003) 167–171.

[2] T. Hino et al., J. Nucl. Mater. 290–293 (2001) 1176–1179.

[3] T. Hino et al., Nucl. Fusion 44 (2004) 496–499.

[4] N. Ashikawa et al., J. Nucl. Mater., 363–365 (2007) 1352–1357.

[5] S.Masuzaki et al., J. Nucl. Mater, 290-293 (2001) 12-18.

[6] T. Hino et al., Fus. Eng. Des, 81 (2006) 127–131.

[7] T. Hino et al., Fus. Eng. Des., 72 (2005) 339-344.

Effect of Thermal Ageing on Mechanical Properties of Reduced Activation Ferritic / Martensitic Steels

Yanfen Li [1, 2], T. Nagasaka [3], T. Muroga [3]

[1] The Graduate University for Advanced Studies, Toki-shi, Gifu-ken 509-5292, Japan
[2] Institute of Plasma Physics, Chinese Academy Sciences, Hefei, Anhui, 230031, China
[3] National Institute for Fusion Science, Toki-shi, Gifu-ken 509-5292, Japan
E-mail of corresponding author: li.yanfen@nifs.ac.jp

Abstract

In this work, the effect of thermal ageing on mechanical properties of JLF-1 (JOYO-II HEAT) and CLAM (HEAT 0603) steels have been studied at temperatures ranging from 823 to 973 K. The results showed that the hardness increased slightly and tensile properties did not change significantly after ageing at 823 K for 2000 h. However, the hardness and the tensile strength decreased after ageing above 823 K. The creep properties were improved after ageing at 823 and 873 K for 2000 h for the both steels. Contrarily, the creep property degraded significantly after ageing at 973 K for 100 h. Compared to JLF-1 steel, CLAM steel has higher hardness, tensile and creep strength but has higher susceptibility to thermal ageing. The lower heat treatment temperature and higher Ta level of CLAM are considered as the possible reasons.

Keywords: structure material, RAFM steels, thermal ageing, mechanical properties

1. Introduction

Blanket is one of the important components of fusion reactors, which provides the primary heat generation and transfer, and tritium breeding systems. Currently, reduced activation ferritic / martensitic (RAFM) steels are considered as the primary candidates for blanket structural components because of their most matured industrial infrastructure and relatively good radiation resistance [1]. JLF-1 and CLAM are the reference steels for Japan and China, respectively [2, 3].

For fusion applications, the long-term thermal stability of these steels at the blanket operation temperature is one of the critical issues. At present, understanding of the mechanical properties and microstructural change by long-term service at high temperature, which is called as thermal ageing, is not sufficient for RAFM steels.

In this work, the effect of thermal ageing at temperatures ranging from 823 to 973 K on mechanical properties of JLF-1 and CLAM steels was investigated.

2. Experiments

The materials used were JLF-1 (JOYO-II-HEAT) and CLAM (HEAT 0603) steels. Their chemical compositions and the detailed heat treatment conditions are listed in Tables 1 and 2.

The SSJ specimens with a gauge size of 5 x 1.2 x 0.25 mm^3 were machined along the roll direction. Then, these specimens underwent ageing experiments in the temperature range of 823 to 973 K under high vacuum.

The Vickers hardness was measured by using a Vickers Hardness testing Machine under a load of 300 g with loading time of 30 s at room temperature. The tensile tests were conducted at an initial strain rate of 6.67×10^{-4} s^{-1} and the test temperatures from room temperature (RT) to

873 K. The uniaxial creep tests up to rupture were performed at 823 K with the applied stress of 250 MPa in a vacuum of < 1 x 10^{-4} Pa.

Table 1 Chemical composition of JLF-1 and CLAM steels in wt%

	Cr	W	C	Mn	V	Ta	O	N	S	Fe
JLF-1	9.00	1.98	0.09	0.49	0.20	0.083	0.0019	0.0150	0.0005	Bal.
CLAM	8.94	1.45	0.13	0.44	0.19	0.15	-	-	0.004	Bal.

Table 2 Heat treatment conditions for JLF-1 and CLAM steels

Type of steel	Normalization	Tempering
JLF-1	1323 K / 60 min / air cool	1053 K / 60 min / air cool
CLAM	1253 K / 30 min / air cool	1033 K / 90 min / air cool

3. Results and discussion

3.1 Hardness measurement

The hardness results are plotted in Fig. 1. They show that the hardness values of CLAM steel were higher than those of JLF-1 at all conditions. After ageing at 823 K for 2000 h, the hardness increased slightly for JLF-1 and CLAM steels. On the contrary, softening occurred above 823 K. The softening of JLF-1 steel was smaller than CLAM.

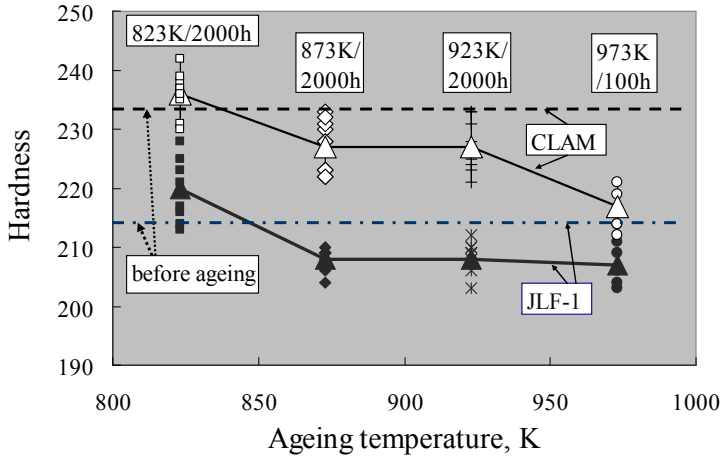

Fig. 1 Hardness change of JLF-1 and CLAM steels by thermal ageing.

3.2 Tensile properties

The tensile tests were conducted from RT to 873 K for all samples of JLF-1 and CLAM and the results are presented in Fig. 2 to 4.

The ultimate tensile strength (UTS) and yield strength (YS) of CLAM steel were higher and total elongation (TE) were smaller than those of JLF-1 steel, in agreement with the hardness data. Compared to other RAFM steels, both steels exhibit adequate strength and ductility level.

As shown in the figure, no significant degradation of tensile properties (UTS, YS and TE) for both steels was detected by ageing at 823 K for 2000 h. Similar behavior after thermal ageing treatments were also observed for F82H [4] and Eurofer'97 steels [5].

However, above 823 K, especially at 973 K, the ageing resulted in a decrease in UTS and YS, accompanied by an increase in TE.

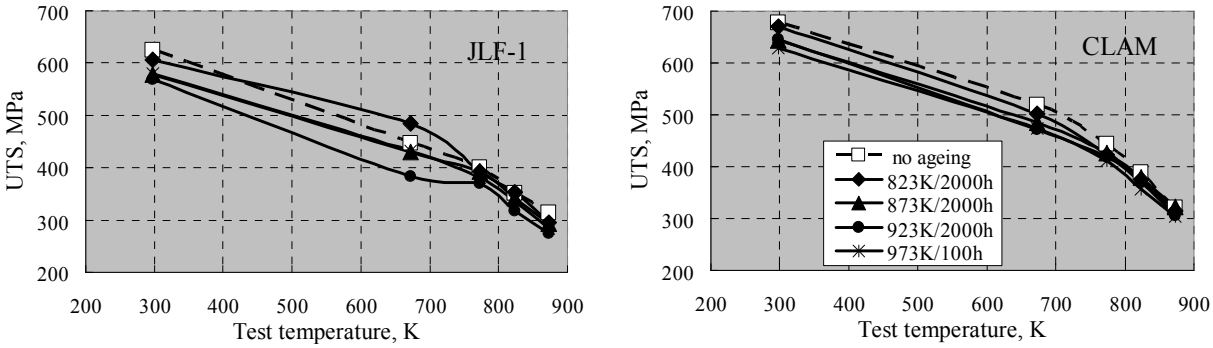

Fig. 2 the effect of thermal ageing on ultimate tensile strength (UTS)

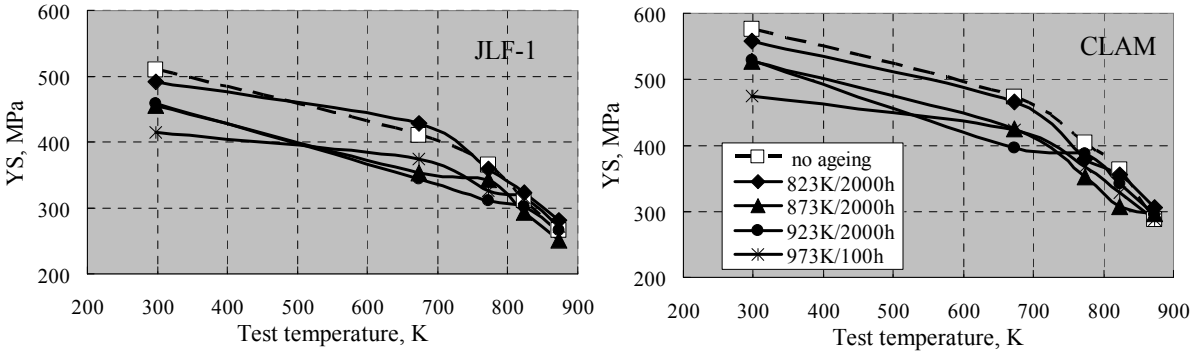

Fig. 3 the effect of thermal ageing on yield strength (YS)

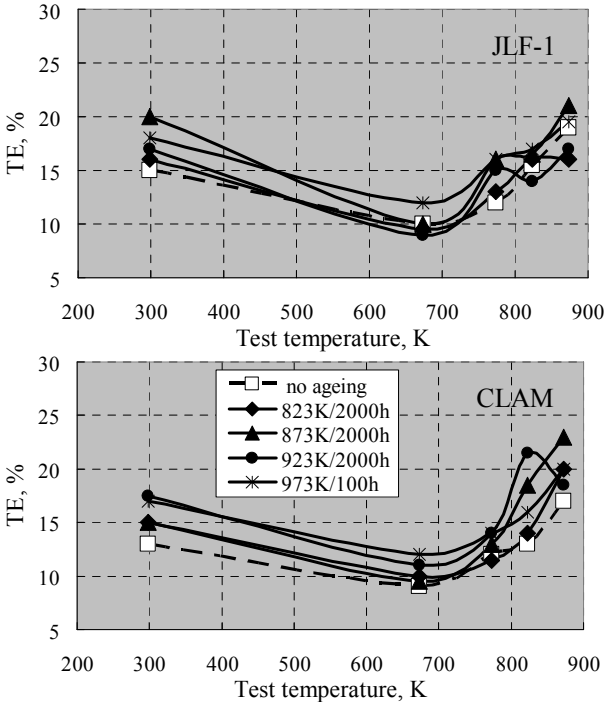

Fig. 4 the effect of thermal ageing on total elongation (TE)

3.3 Creep properties

The uniaxial constant load creep tests were conducted at 823 K with the applied stress of 250 MPa and the creep curves are showed in Fig. 5. The typical creep curves of the present steels, similar to that observed in other RAFMs, were composed of the primary or transient region, where the creep rate decreases with time, steady state region with the minimum creep rate, and the tertiary or accelerated creep region characterized by an increasing creep rate until the material rupture.

For CLAM steel, after ageing at 823 to 923 K for 2000 h, the minimum creep rate decreased and the rupture time increased. Similar to CLAM, by ageing at 823 and 873 K for 2000 h for JLF-1, the creep rupture time increased. But further ageing at 923 K for 2000 h returned the properties to almost the level of no aging. On the other hand, ageing at 973 K for 100 h caused a significant degradation in creep properties, which is consistent with the results of hardness. Although the minimum creep rate is smaller and rupture time is longer for CLAM than those of JLF-1, CLAM is more susceptible to thermal ageing than that of JLF-1.

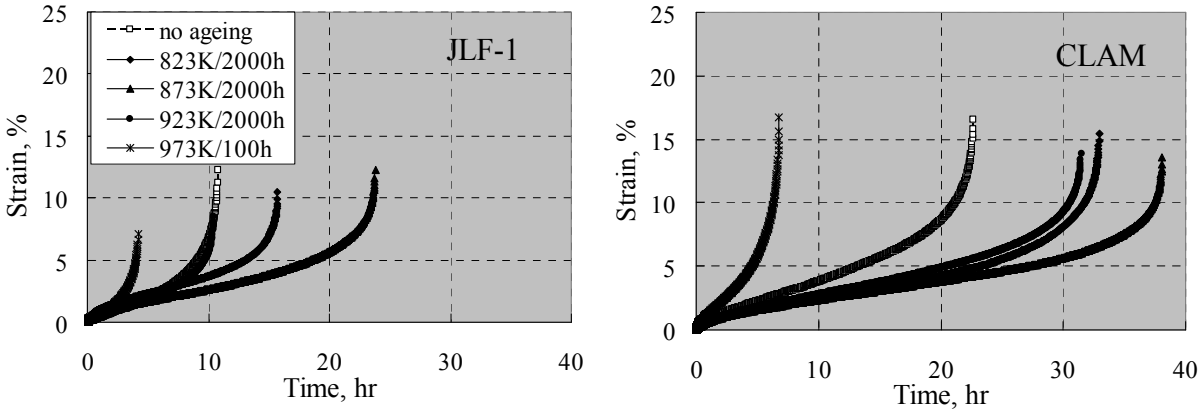

Fig. 5 Creep curves of JLF-1 and CLAM steels tested at 823 K with 250 MPa stress

4. Summary

The ageing experiments were carried out for JLF-1 and CLAM in the temperature range of 823 to 973 K and the mechanical properties were investigated. The conclusions of the study are listed below:

(1) The hardness increased slightly after ageing at 823 K for 2000 h for the both steels. However, ageing above 823 K caused a decrease in hardness.

(2) No significant decrease of tensile strength was detected by ageing at 823 K for 2000 h. However, the tensile strength decreased and total elongation increased after ageing above 823 K, especially for ageing at 973 K.

(3) The creep strength increased after ageing at 823 and 873 K for 2000 h for both steels. However, the creep property degraded significantly after ageing at 973 K for 100 h.

(4) These results indicated that the mechanical strength increased after ageing at 823 K for 2000 h and decreased after ageing above 823 K.

(5) CLAM steel has higher hardness, tensile and creep strength, but has higher susceptibility to thermal aging than those of JLF-1. The lower heat treatment temperature and higher Ta level of CLAM are considered as the possible reasons.

Acknowledgements

This work was carried out based on NIFS Budget Code NIFS07UCFF003 and NIFS07GCFF003. This work was also supported by JSPS-CAS Core University Program.

References

[1] T. Muroga, M. Gasparotto and S. J. Zinkle, Fusion Eng. & Des., **61-62** (2002) 13-25.
[2] A. Kohyma, Y. Kohno, M. Kuroda, et al., J. Nucl. Mater. **258-263** (1998) 1319-1323.
[3] Q. Huang, C. Li, Y. Li, et al., J. Nucl. Mater. **367-370** (2007) 142-146.
[4] L. Schäfer, M. Schirra, J. Nucl. Mater. **283-287** (2000) 662-666
[5] R. Lindau, A. Möslang, M. Schirra, Fusion. Eng. & Des. **61-62** (2002) 659-664.

Nano-scale Plasma-Material Interaction in Long-Term Metallic Samples Left in LHD

T. Tokunaga[1], Y. Ohtawa[1], N.Yoshida[2], M.Tokitani[3], N.Ashikawa[3], T.Akiyama[3], K.Kawahata[3]
1 IGSES, Kyushu University, Kasuga, 816-8580 Japan
2 Research Institute for Applied Mechanics, Kyushu University, Kasuga, 816-8580 Japan
3 National Institute for Fusion Science, Toki, 509-5292 Japan
E-mail of corresponding auther: toku-ta@riam.kyushu-u.ac.jp

Abstract

Microstructural change of metallic samples (Cu, CuCrZr alloy, SUS, Mo) left on the erosion dominant area of the first wall in LHD for one experimental cycle were examined. In SUS and Mo net erosion was only 140-150nm. On the other hand in Cu and CuCrZr alloy with surface was strongly modified by sputtering and local re-deposition of the sputtered Cu atoms. In all samples examined, dense nano-scale He bubbles at the saturation level were formed in the directly below the bombarded surface. It is considered that they were formed by He main plasma discharge and He glow discharge cleaning and the sputtering dominant surface of the first wall more or less kept such damage structure.

Keywords: LHD, plasma-wall interaction, helium plasma, hydrogen recycling

1. Introduction

Plasma facing surfaces such as the first wall and the divertor suffer very strong bombardment of plasmas under main plasma discharges and also wall conditioning. These particles cause surface erosion by sputtering at or near the surface. They also cause irradiation damage in the sub-surface region of the plasma facing materials [1]. The sputtered atoms, on the other hand, re-deposit on the surface after transportation. Due to such synergistical processes, properties of the surface changes depending on the extent of each process. If the deposition is dominant, deposited layer covering the original surface determine the surface properties. In case of TRIAM-1M, for example, co-deposit of Mo and O caused very strong retention of H in it [2]. It was also reported that the strong damage formed directly under the surface by He ion irradiation seriously changed the behavior of H in metals [3].

Active control of PWI is getting more and more important according to the improvement of plasma parameters, especially the plasma duration time getting longer. It often occurs that uncontrolled desorption of H from the wall or divertors results in termination of the plasma discharge [4]. The first step for controlling of PWI is to understand the change of plasma facing surfaces such as structure and chemical component. In the present work, therefore, nano-scale microstructure change of the test sample placed on the inner wall of the vacuum vessel of Large Helical Device (LHD) was examined by TEM, LSM and SEM to know the

underling mechanism of the phenomena.

2. Experimental

As illustrated in Fig1, well polished metallic samples of Cu, Cu-0.8Cr-0.2Zr alloy, SS316 and Mo were left on a vacuum vessel of LHD for 4 months in the cycle 10 to expose the plasmas. The distance between the samples and the plasma was 28cm. In the experimental cycle various kind of plasma discharge were carried out as summed up in Table 1. In addition to H plasma discharges, He plasma discharges were often carried out. In case of the glow discharge cleaning He was major working gas. After the end of the cycle 10 experiments, the samples were taken out, and subsequently surface morphology and internal structure directly under the plasma facing surface were examined in details by means of scanning electron microscopy (SEM), laser scanning microscopy (LSM) and transmission electron microscopy (TEM).

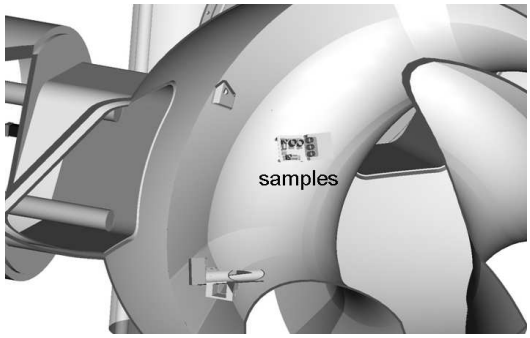

Fig.1 Position of the samples in LHD

Table 1 Discharge in Cycle 10

Discharge	Number of Dis.	Total Dis. Time****	Total Fluence of High Energy Particles*****
H Main Dis. *	4531	9062s (2.52h)	9.0×10^{22} H/m²
He Main Dis. **	1601	3202s (0.89h)	3.2×10^{22} He/m²
Ne, Xe Main Dis.***	233	466s	
H_2-GDC	18	266.8h	1.5×10^{23} H/m²
He-GDC	41	418.2h	2.4×10^{23} He/m²
Ne-GDC	4	61.7h	4×10^{22} Ne/m²
Ar-GDC	3	17.4h	1×10^{21} Ar/m²

* Including H pellet discharges (104 times)
** Including He+H discharges (115 times)
*** H+Ne, H+Xe, Ne discharges
**** Assuming average discharge time to be 2s.
***** assuming flux of keV order neutrals on the first wall to be 1×10^{18}H/He/m²s for main discharges, and assuming average ion flux under GDC to 1.6×10^{17}ions/m²s.

3. Results and Discussion

Effects of the plasma exposure depend on the materials as shown in Fig. 2 where photographs and SEM micrographs of each sample are summarized. In case of SUS316 and Mo, original metallic luster has been kept well but it has lost in Cu and CuCrZr alloy. It is clear that the surfaces of the former are considerably smooth but those of the latter are covered by the dense fine projections. According to the LSM measurement, all of the samples were eroded; net erosion for Cu, SUS316 and Mo are >2200nm, about 140nm and about 130nm, respectively. Deposition of the impurities was not detected. It is worth to note that the net erosion of SUS316 and Mo is very small; nevertheless they were placed close to the plasma (28cm).

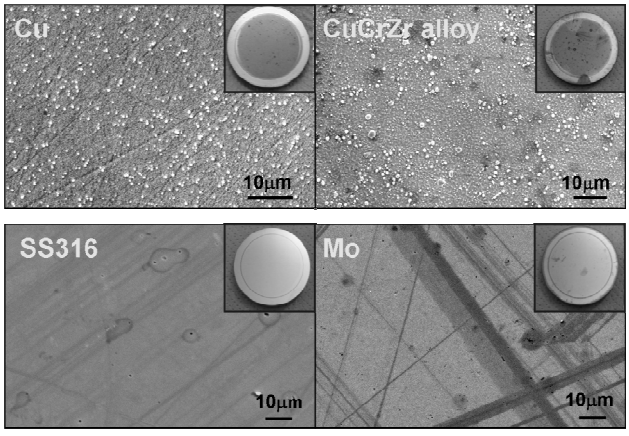

Fig.2 Photographs and SEM micrographs of the samples.

Magnified SEM micrographs of the rough Cu surface are shown in Fig 3. It is interesting that the density of the projections in meso-scale is not uniform but strongly depends on crystal grains. The size of the projections, however, does not depend much on the crystal grains. As can be seen in the highly magnified micrograph, they have odd shape like flowers with overlapping petals as a narcissus or a table coral. Surface of the petals has a concave curvature. Their size and eight are about 1μm and 0.5μm, respectively. These results indicate that the Cu atoms sputtered from the surface around the projection form it by re-depositing on the underside of the petals.

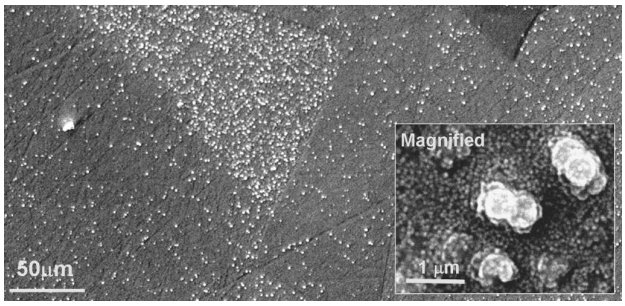

Fig.3 Magnified SEM micrographs of Cu

As can be seen in the highly magnified micrograph in Fig.3 surface of the cupper sample is uneven in nano-scale. In order to know the details of the surface morphology and also sub-surface structure, cross sectional TEM specimens were picked up by using FIB. Fig.4 is a TEM micrograph of a cross sectional specimen. Some 10 nm-scale projections like a sharp pyramid are formed on the surface very densely. They correspond to the uneven surface observed in the SEM micrograph in Fig.3. Continuous image contrast from the sub-surface region to the projections indicates that they were carved by sputtering but not by re-deposition as the meso-scale projections shown in Fig.3. Formation of the meso-scale deposited projections and some 10nm-scale carved projections seem major origins of the optical reflectivity reduction. One should pay attention that such surface roughing increases effective surface area and may change vacuum properties.

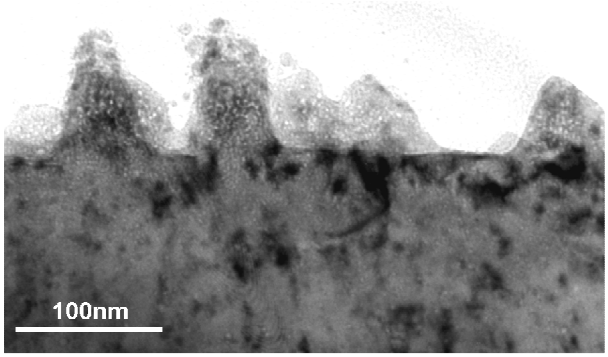

Fig.4 Cross sectional TEM micrograph of Cu.

It is remarkable that very dense nano-scale cavities are formed in the pyramid-like projections and subsurface region up to 60-70 nm deep. Cross sectional TEM images of SUS316 and Mo is shown in Fig.5. In these samples no deposited projections and no remarkable carved projections are formed, but nano-scale fine cavities are formed densely as Cu. According to He plasma bombardment experiments, the cavities are He bubbles formed under He plasma discharges and He glow discharge cleaning. It is known that H plasma and Ne plasma do not form such cavities

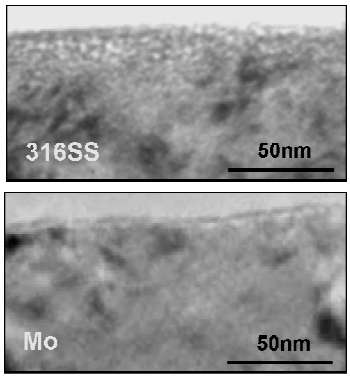

Fig.5 Cross sectional TEM micrographs of SUS316 and Mo.

even at very high fluence. One should note that He plasma bombardment plays a major role for the internal damage in the metallic first wall in LHD.

According to the fundamental study on the irradiation effect of low energy He ion in metals, density of nano-scale He bubbles saturates at the fluence about $1x10^{21}He/m^2$. Comparing with these results, one can say that formation of He bubbles in the present samples have already reached to the saturation level. On the other hand, He plasma exposure experiments performed in LHD indicate that the He bubble density saturates only by exposing for about 100s. As listed in Table 1, He was often used for main plasma discharge experiments as well as glow discharge cleaning in LHD. It means that dense He bubbles at saturation level always exist in the sub-surface region of the erosion dominant part of the first wall of LHD excepting just after Ne glow discharge cleaning. It is known that formation of He bubbles, in actual dense dislocation loops are formed together, enhances retention of H very much and the behavior of its thermal desorption also changes. One should take the irradiation effect of He plasmas into account for understanding and controlling of the H recycling, which is especially important for long duration discharge.

In general, properties of the plasma facing surface change depending on the balance of the sputtering erosion and the impurity deposition. Though the surface properties of the sputtering dominant area were studied in the present work, those of the deposition dominant area are also important to understand the PWI globally. Comprehensive studies of the plasma facing surface of LHD in nano- and micro-scale are now going on.

4. Summary

Microstructural change of metallic samples (Cu, CuCrZr alloy, SUS, Mo) left on the erosion dominant area of the first wall in LHD for one experimental cycle were examined by means of SEM. LSM and TEM. In SUS and Mo, which have rather low sputtering yield, net erosion was only 140-150nm. On the other hand in Cu and CuCrZr alloy with rather high sputtering yield the surface was strongly modified by sputtering and local re-deposition of the sputtered Cu atoms. Surface roughening due to these processes may reduce vacuum properties.

In all samples examined, dense nano-scale He bubbles at the saturation level are formed in the directly below the bombarded surface. It is considered that they were formed by He main plasma discharge and He glow discharge cleaning. Because He was often used for the discharges in LHD, the sputtering dominant surface of the first wall more or less kept such damage structure. It is likely that accumulation of defects such as bubbles enhances the retention of H very much and affects hydrogen recycling.

Acknowledgements

This work was partly supported by the JSPS-CAS Core University Program in the field of Plasma and Nuclear Fusion.

References

[1] N. Yoshida, et al., J. Nucl. Mater. 337-339 (2005) 946-950
[2] M. tokitani, et al., J. Nucl. Mater. 367-370 (2007) 1487-1491
[3] H. Iwakiri, et al., J. Nucl. Mater. 307-311 (2002) 135-138
[4] M. Tokitani, et al., J. Nucl. Mater. 363-365 (2007) 443-447

Preliminary Electromagnetic Analysis of Correction Coils for ITER

Wu Weiyue, Liu Xufeng, Du Shuangsong, Zen Wenbin, Du Shijun,
Wei Jing, Liu Changle, Han Shiqiang, Liu Liping

Institute of Plasma Physics Chinese Academy of Sciences
PO Box 1126, Hefei, Anhui 230031, P.R. China
E-mail of corresponding author: wuwy@ipp.ac.cn

Abstract

The Correction Coils System (CCs or CC) in ITER consists of eighteen individual multi-turn coils arranged in three groups (Top, Side and Bottom) around the TF coils. It was used to compensate field errors arising from misalignment of the coils and winding deviations from the nominal shape as a result of fabrication tolerances, joints, leads and assembly tolerances. The six side coils are also used for feedback control of plasma resistive wall mode (RWM) disturbances.

The top and bottom coils is located between TF cases and PF6 coil and consists of six saddle type coils covers a 60° sector and spans three TF coils in the toroidal direction at upper and lower of the TF coil. The side coils is located between TF cases and both of PF3 coil, PF4 coil and consists of six quadrilateral shape type coils arranged around the toroidal circumference with a 40° sector and each coil spans only two TF coils at aside of the TF coil. All Corrections Coils (lower, side and upper) are then attached to the TF coil cases.

The electromagnetic field and forces acting on the CC winding are calculated with the CC current and ITER presented design scenario (burn time), which includes TF in operating, PF system discharge, plasma initiation, current ramp-up and heating to a driven burn.

The CCs experience electromagnetic forces due to their self-field and the field of the TF coils, PF coils and CS coils. During calculating, the geometrical dimensions of all coils are originally defined in the reference of ITER Design Description Document DDD 11 Magnet Section 1. It was an engineering description (ITER_D_22HV5L v2.2) in 2006 version.

Keywords: Correction, electromagnetic

1. Introduction

The magnet system for ITER consists of eighteen toroidal field (TF) coils, a central solenoid (CS, it was 6 pieces assembly together), six poloidal field (PF) coils and eighteen correction coils, as shown on fig.1 and fig. 2. Table 1 shows the Major Parameters of the Correction Coils (CCs) [1].

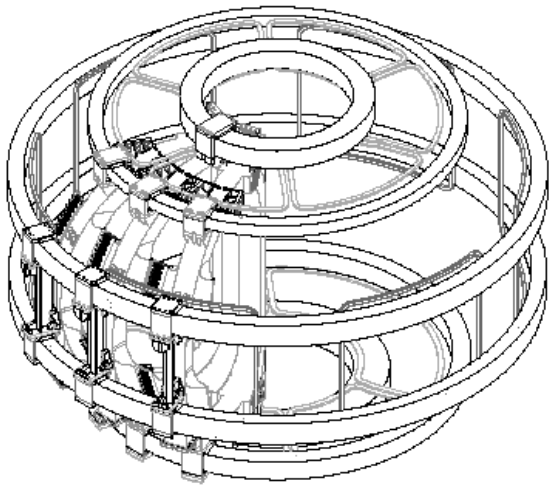

Fig. 1 The magnet system for ITER

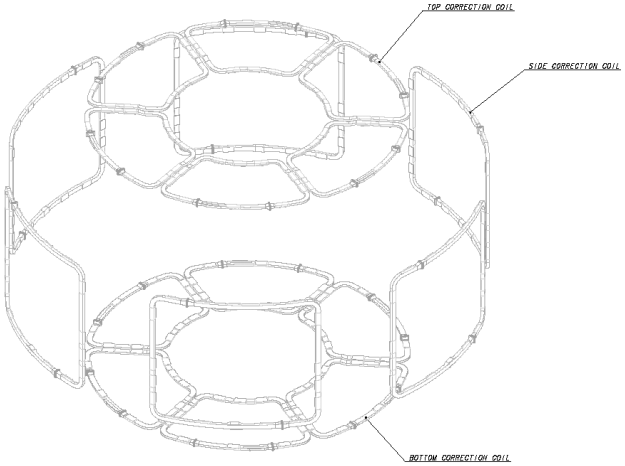

Fig. 2 The correction coils for ITER

Table 1. Major Parameters of the Correction Coils

Parameters	Top	Side	Bottom
Number of coils	6	6	6
Average turn length (m)	17.7	28.7	17.7
Turns per coil	14	20	18
Nr x Nz	7 × 2	5 × 4	9 × 2
Total conductor length per coil (m)	251	573	323
Number of conductors per coil	1	1	1
dR (winding section) (m)	0.1554	0.127	0.2158
dZ (winding section) (m)	0.0604	0.1048	0.0604
Coil case thickness	0.020	0.020	0.020
dR (coil section) (m)	0.2114	0.167	0.2558
dZ (coil section) (m)	0.1004	0.1448	0.1004

The CCs use a 10KA cable-in-conduit conductor using NbTi superconductor. The cable includes 240 SC strands and does not have any central cooling channel. The SC stand diameter is 0.73mm.The cable is conservatively designed to operate up to 6T and 5K.The cable is formed square with a square outer steel jacket. Jacket outer dimension is 19.2mm × 19.2mm.

The current capacity of top CCs (TCC) is 140 kA at 5T. The current capacity of side CCs (SCC) is 280 kA at 5T. The current capacity of the bottom CCs (BCC) is 180 kA at 5T. Detailed parameters are given in Table.2. The CCs are self supporting for loads along the conductor, but are supported for lateral loads by the TF coil case.

2. Electromagnetic Analysis on the field

The electromagnetic field and force acting on the CCs winding are calculated by the EFFI code, which was developed by Lawrence Livermore National Laboratory (USA) [2].

(ア) Self magnetic field

The CCs contribute to the magnetic field was shown in fig. 3 and 4. The self-field of the CCs at equator plane (z=0.568m) is about 20 to 30 Gauss on the radius R=6.4m. It is 0.5 Tesla on the body of the bottom coil and 0.4 Tesla on the side coil that the radius R=6.4m. Fig. 5 show the field on the bottom and fig. 6 shown it on the side from 0° to 180° include more than two coils.

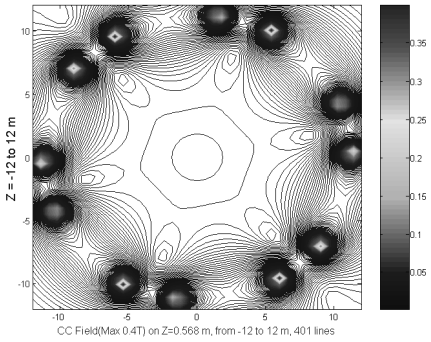

Fig. 3 Magnetic field at plasma equator plane

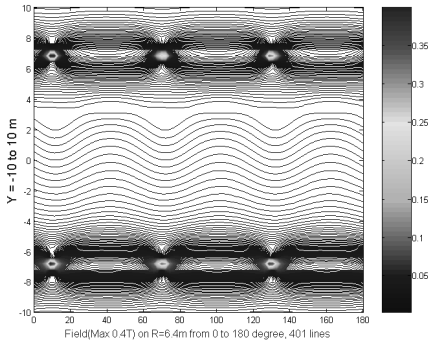

Fig. 4 Magnetic field at plasma equator plane

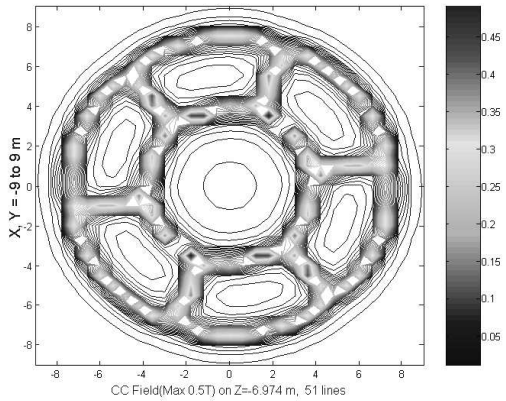

Fig. 5 The self field on bottom coil

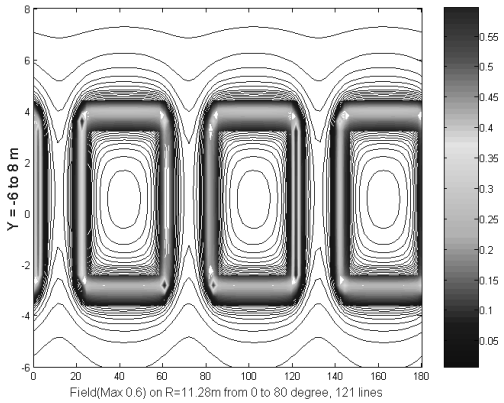

Fig. 6 The self field on side coil

(イ) Currents of the PF and CS

The currents of PF, CS and plasma were shown in fig. 7. It was takes from ITER DDD (Design Description Document) 2006(Table 1.1.4-5 Reference Scenario, Currents unit is MA-turn for each coil). The results show the peak integrated field on CCs in different moment. It was that on bottom in SOF

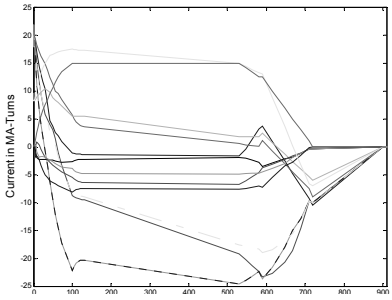

Fig. 7 Currents of PF, CS, Plasma

(4.94 Tesla, most from PF6), on top coil in XPF (2.81 Tesla, most from PF1) and on side in EOB (2.62 Tesla, most from PF3).

(ウ) Electromagnetic Analysis on the force

The Currents for the calculation of the electromagnetic forces was different for each type coils of CCs. The Electromagnetic force along the perimeter of the bottom coil is shown in Fig.8 and 9. Along the perimeter of bottom coil, it was divided 401 sections that each length is about 44.5 mm. The peak force at one section is 3908 Newton on bottom and 1572.3 on top[3].

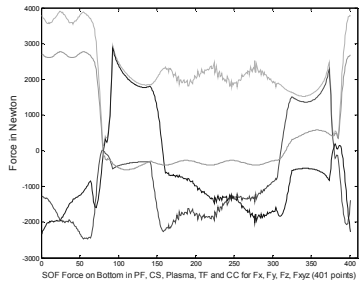

Fig. 8 Force on Bottom coil along perimeter

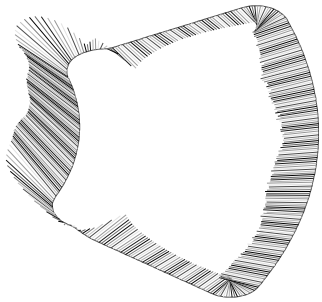

Fig. 8 Force on Bottom coil in 3D view

Along the perimeter of side coil, it was divided 400 sections that each length is 61.4 mm. The peak force is 2643.3 Newton on one section.

3. Conclusion

The magnetic field from CCs at plasma area is 20 ~ 30 Gauss. In ITER magnetic system, it was in different moment for the peak field on each type correction coil. The maximum field on bottom coil is 4.94 Tesla and the force is 3909 Newton per section (44.5mm) in SOF, on side is 2.62 Tesla and the force is 2643.3 Newton per section (61.4mm) in EOB, on top is 2.81 Tesla and the force is 1572.3 Newton per section (44.5mm) in XPF.

Acknowledgements

This work was partly supported by the JSPS-CAS Core University Program in the field of Plasma and Nuclear Fusion.

References

[1] DDD (Design Description Document) ITER_D_22HV5L v2.2, 2006

[2] Chen Wenge, The Design of Correction Coils (ITA 11-15), work report, 2005.10

[3] Du Shuangsong, Correction Coils, work report, 2008.09

Key Issues on Development of Superconducting Magnet Technology toward to DEMO

A. Nishimura
Fusion Engineering Center, National Institute for Fusion Science, Toki, Gifu 509-5292 Japan
E-mail of corresponding author: nishi-a@nifs.ac.jp

Abstract

When DEMO plant is foreseen, some new technologies would be needed to design and construct the superconducting magnet system. In this study, some key issues newly discussed and developed in Japan are presented, which include (1) design code of TF magnet structure established by JSME, (2) network of neutron irradiation investigation on superconducting magnet materials, (3) new design concept of superconducting conductor for huge electro-magnetic force, and (4) others.

Keywords: DEMO plant, Superconducting magnet system, Neutron irradiation, Design code.

1. Introduction

The ITER project is undergoing under the construction agreement by seven countries/parties, European Union, United States, Russia, India, Korea, China and Japan. DEMO will be designed based on ITER experiment and create Deuterium-Tritium (D-T) burning plasma and generate a lot of 14 MeV neutrons. To yield the plasma and keep it stable, the superconducting magnet system is desired to provide a large-scale magnetic field. DEMO will have larger plasma volume (the miner radius) and the coil current will increase even the magnetic field at the plasma axis is the same. It means that the electro-magnetic force will increase drastically and the support structure for the force will become more complicated and important which require new developments and technologies.

In this paper, some important issues will be discussed supposing the DEMO plant. First, the superconducting magnet case will be focused and the cryogenic structural material with higher yield stress and toughness will be discussed following a short introduction of TF coil case structural code established by Japan Society of Mechanical Engineers, JSME. Then, the importance of the neutron irradiation study will be explained and the new collaboration scheme recently developed will be described showing the neutron irradiation effect on the critical current. The third issue will be the superconducting conductor design to reduce the degradation of the critical current under high electro-magnetic force. In the last part, other concerning issues will be summarized.

2. Structural Materials Issue

ITER requires about 14 m high and 9 m wide toroidal field (TF) magnets which provide 5.3 T at plasma axis. The maximum electro-magnetic force on TF magnet will be 15.9 MN/m and this huge

force would turn and bend the TF magnet. The maximum electro-magnetic force on the TF conductor will be about 800 kN/m. (11.8 T x 68 kA) In case of DEMO, the force will increase to about 1500 kN/m. (15 T x 100 kA) To support the huge force, a lot of structural material is needed. If the yield stress does not increase in the future, the structural material will occupy over 90 percent of the cross section of the magnet. Therefore, higher yield stress cryogenic structural material is desirable with higher toughness to make a slim magnet.

JSME established the construction code in Japanese named "JSME Construction Standard for Superconducting Magnet of Fusion Facility (temporary title)". The code consists of seven chapters and Appendixes. The chapter tiles (temporary) are General requirements, Materials, Design, Fabrication (Quality control), Non-destructive testing, Leak test and pressure proof test and Glossary. The English version is under consideration and will be available in next spring in 2009. "Materials" specifies four structural materials, FMJJ1, FM316LNL, FM316LNM, and FM316LNH. The three 316LN steels are classified by the content of (C+N). FM316LNL contains less than 0.08 wt% of (C+N), and FM316LNM and FM316LNH contain from 0.08 to 0.13 wt% and 0.013 to 0.18 wt%, respectively. Since the yield and ultimate tensile strengths at 4 K have a good linear relation with (C+N), these three steels are specified to show certain yield and ultimate tensile strengths. The temperature dependence of the strengths is analyzed and the regression curves are formed in a quadratic equation of which coefficients are given in tables in the code. The regression curves give definitely smaller strengths than experimental results, so the users are able to apply these values as the design stress or the design ultimate tensile strength. When an owner or a fabricator wants to use a material which is not listed in the code, he submits application form to the committee in JSME to get an approval. The approval process is also specified in the code.

The standardization is important to educate the workers and keep the high level technologies. The new construction code will be referred by ITER, JT60SA and other devices.

3. Collaborative Investigation on Neutron Irradiation Effect

The neutron generated in the burning plasma will penetrate through the blanket to the superconducting magnet space. Also, the neutron will stream out of the ports to outside of the plasma vacuum vessel. So, the superconducting magnet will be irradiated by neutron and gamma ray yielded by isotopes which are formed by neutron irradiation. To

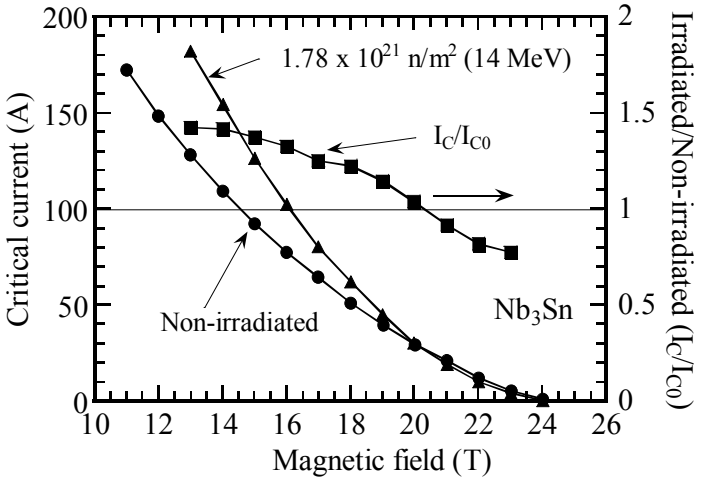

Fig.1 Change in critical current against magnetic field.

carry out the study on neutron irradiation effects, the collaboration network among researchers working in different fields must be built up and deep and wide discussions must be continued sharing the individual experience and knowledge. The collaborative scheme is under construction in Japan and the typical test results are shown in Fig.1 [1]. The magnetic field dependence of the critical current of Nb_3Sn wire after 14 MeV neutron irradiation of 1.78 x 10^{21} n/m^2 has been clarified and it should be noted that B_{C2} did not change being about 25.5 T after irradiation. These data are the world first and the mechanism for the changes is now under investigation.

4. Countermeasure against Huge Electro-magnetic Force

In case of DEMO, the electro-magnetic force becomes very huge and the support structure must be designed carefully. The strand is damaged by the compression stress by the electro-magnetic force and the critical current degrades. Also, the cyclic energizing of the magnet deteriorates the coil performance. So, a countermeasure must be considered against the huge electro-magnetic force.

In the strand level, the use of Nb_3Al must be considered as well as a strengthened stabilizer or a harder surface material such as CuNb matrix. In the cabling level, Rutherford cable type conductor or a smaller capacity conductor may be applicable, but increase of inductance due to the increase of turn numbers should be noticed and a multi-power supply system may be considered. Regarding a free space in a cable-in-conduit conductor, the reduction of the void ratio has been carried out, and the void ratio was reduced to about 27-28 % and the twist pitch was elongated to be about twice and more for the ITER TF conductor. Since the wire motion occurs because of the free space, the new trial to fill the space with water ice has been performed as show in Fig.2 [3,4]. After the cyclic loading up to 1000 cycles, any degradation was not observed in the critical current. From this result, it is clarified that the prevention of the wire motion constricts the degradation of the critical current.

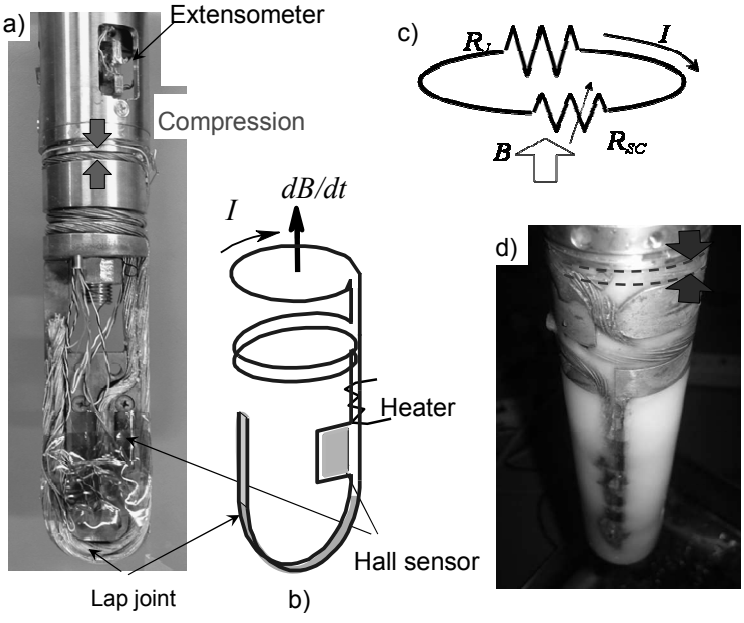

Fig.2 Sample for wire motion effect on critical current.

5. Other Concerns

DEMO or a fusion reactor system has not been built in the world and there is a free-floating anxiety on the construction of the reactor. As for the superconducting magnet, the cold leak of the helium, the joint electric resistance and the insulation voltage

are the most concerned issues. Such unshapen fear will be able to be carted off by a sever acceptance test. So, the concept for the acceptance test and the meaning must be considered.

The vacuum space for the thermal insulation in the cryostat will be activated by the penetrated and streamed out neutrons. Therefore, human beings cannot enter into the cryostat because of the heavy irradiation. However, the insulation breaks on the piping, sensor cables and conductor joints will be arranged in this space. It must be performed to prepare countermeasures against unexpected trouble and emergencies.

6. Summary

Some important issues are summarized and new information is presented in this paper. To develop DEMO plant after ITER project, a lot of preparative works must be done. At present, the key issues must be listed and a plan for development should be formed. The collaborative studies will be encouraged to realize a real component and a commercial fusion reactor.

Acknowledgements

The authors would like to express his thanks to Drs. Y. Hishinuma, T. Tanaka, T. Muroga at National Institute for Fusion Science, Mr. M. Sakamoto at The Graduate University for Advanced Studies, Dr. S. Nishijima, Y. Izumi at Osaka University, Drs. I. Sato, K. Watanabe, G. Nishijima, H. Kurisita, T. Shikama at Tohoku University, K. Takakura, Drs. K. Ochiai, T. Konno, T. Henmi, N. Koizumi, K. Okuno at Japan Atomic Energy Agency for their contribution to perform this study.

Part of this work was supported by Grant-in-Aid for Scientific Research (#16560725), NIFS-JAEA collaboration program in 2008 on mechanical property evaluation of radiation-proof insulation material for ITER TF coil, NIFS collaboration research programs (NIFS04KOBF008, NIFS07KOBF014), Fusion Engineering Research Centre program at NIFS (NIFS06UCFF013, NIFS08UCFF005) and Budget for Nuclear Research of the MEXT.

The superconducting tests at high magnetic field were performed at the High Field Laboratory for Superconducting Materials, Institute for Materials Research, Tohoku University.

This work was partly supported by the JSPS-CAS Core University Program in the field of Plasma and Nuclear Fusion.

References

[1] A. Nishimura, et al., “Neutron Irradiation Effects on Superconducting Wires and Insulating Materials”, presented at SOFT-25, Rostock, Germany, September (2008).

[2] K. Seo, et al., ”Critical current of mechanically loaded Nb_3Sn superconducting multi-strand cable”, IEEE Trans. Appl. Supercond. 17, 1390 – 1393 (2007).

[3] K. Seo, et al., ”Mitigation of critical current degradation in mechanically loaded Nb_3Sn

superconducting multi-strand cable by icemolding", Submitted to Plasma and Fusion Research, The Japan Society of Plasma Science and Nuclear Fusion Research (JSPF).

Characterization of Thick Vacuum Plasma Sprayed Tungsten Coatings on Water-cooled Copper Alloy Substrate

Y. Niu[1], X. Zheng[1], H. Ji[1], C. Ding[1], J. Chen[2], Y. Yahiro[3], N. Yoshida[4]

1 Shanghai Institute of Ceramics, Chinese Academy of Sciences, Shanghai, 200050 China

2 Institute of Plasma Physics, Chinese Academy of Sciences, Hefei, 230031 China

3 Interdisciplinary Graduate School of Engineering Sciences, Kyushu University, Fukuoka, 816-8580 Japan

4 Research Institute for Applied Mechanics, Kyushu University, Fukuoka, 816-8580 Japan

E-mail of corresponding author: yrniu@mail.sic.ac.cn, xbzheng@mail.sic.ac.cn

Abstract

In this work, thick tungsten coating (1.8mm) was fabricated by vacuum plasma spraying technology on water-cooled copper alloy substrate. The microstructure of the coating was characterized using scanning electron microscopy (SEM) and transmission electron microscopy (TEM). The joint interface of the coating and substrate was emphasized. The bonding strength and thermal property of the coating were analyzed. The results showed that the coating was mainly composed of well melted tungsten particles and exhibited lamellar structure. Grains of 0.5-1μm sizes were found inside of the coating and grains of nanometer size appeared at the area near the interface. The adhesion of the coating and substrate was well. The bonding strength was about 35MPa and the thermal conductivity of the coating was about 105 $W \cdot m^{-1} \cdot K^{-1}$ at room temperature.

Keywords: vacuum plasma spraying, tungsten coating, microstructure, copper alloy substrate

1. Introduction

Tungsten is one of the potential candidates for the plasma facing materials in fusion experiment devices, for its special properties such as highest melting point of all metals, high energy threshold for physical sputtering; low deuterium etching; good thermal conductivity and high temperature strength and dimensional stability [1-2]. Plasma spraying technology has intensive applications in industrial fields, for its advantages such as high deposition efficiency, cost effectiveness, ability of fabrication of large area and flexibility for automatic production [3]. The plasma spraying technology enables the preparation of a broad variety of coating materials, including high melt point materials and has become the most favorite way to prepare W coating now [4-5]. The microstructure of coatings had great influence on the properties of coatings and well microstructure warranted the needed properties of coatings. At the same time, the joint interface of the coating and substrate was critical to the application of the coating.

In this work, thick tungsten coatings were prepared on the surface of water-cooled copper alloy. The microstructure of the coating was analyzed. The interface of the coating and copper alloy substrate was focused. And the bonding strength and thermal conductivity of the coating were examined. The aim of the work is to identify the microstructure of the interior and interface of tungsten coating on copper alloy substrate and afford the basic properties of the coating.

2. Experiments

A vacuum plasma spraying system (A-2000, Sulzer Metco, Switzerland) with a F4-VB torch was applied for the spray campaign. Argon and hydrogen were used as plasma forming gases. Water-cooled copper alloy was applied as substrate. The Twin-System (Plasma-Technick, Switzerland) was applied for a powder feeding. A tungsten coating with thickness of 1.8mm was fabricated.

The surface morphology and cross-sectional microstructure of the coatings were observed using a scanning electron microscopy (SEM, EPMA-8705QH, Shimadzu, Japan). The transverse section (perpendicular to the spraying direction) microstructure of the coatings was characterized with a transmission electron microscopy (TEM, JEM-200CX, JEOL, Japan). The bonding strength of the coating was evaluated according to ASTM C 633-79. The thermal diffusivity of the coating was examined by the laser flash method (Netzsch, LFA427). The thermal conductivity was calculated from the values of density, specific heat and thermal diffusivity.

3. Results

Figure 1 presented the surface morphology of vacuum plasma sprayed tungsten coatings (VPS-W). The coating was mostly composed of well melted particles. From the morphology of high magnification, it was noticing that there were microcracks appeared on the surface. It was supposed that microcracks were related to the stresses in the coating.

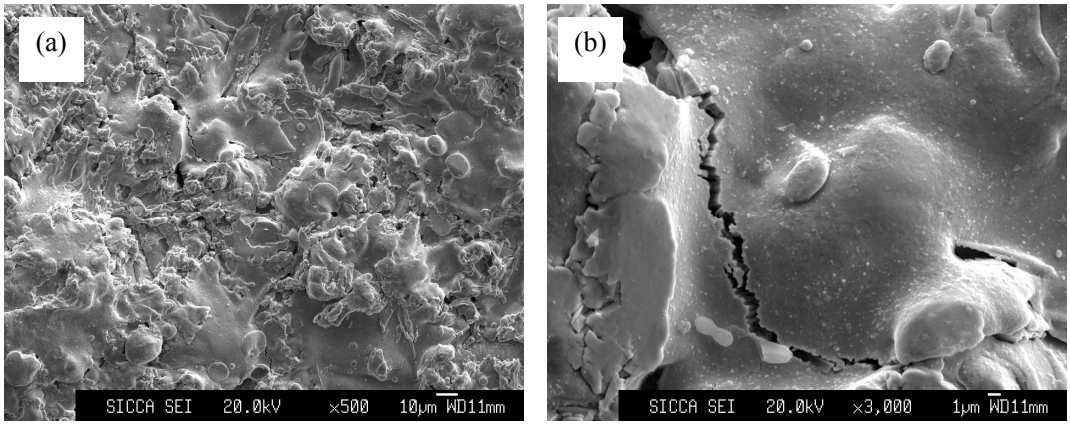

Fig. 1 Surface micrographs of VPS-W coating: (a) low magnification; (b) high magnification.

The cross-section of VPS-W coating was showed in Fig. 2. It can be seen that VPS-W coating was compact and mostly composed of layers of well-flattened splats. The pores were mainly in linear shape which was related to the interface of splats and few pores in circular shape were found. And there were few un-melted particle found in the coating, as the arrow pointed. Then we focused on the combination of the coating and copper alloy substrate. The interface of the coating and substrate was illustrated in Fig. 2(b). It can be seen that the bonding of VPS-W coating and copper alloy substrate was tight and no microcracks or pores formed at the interface.

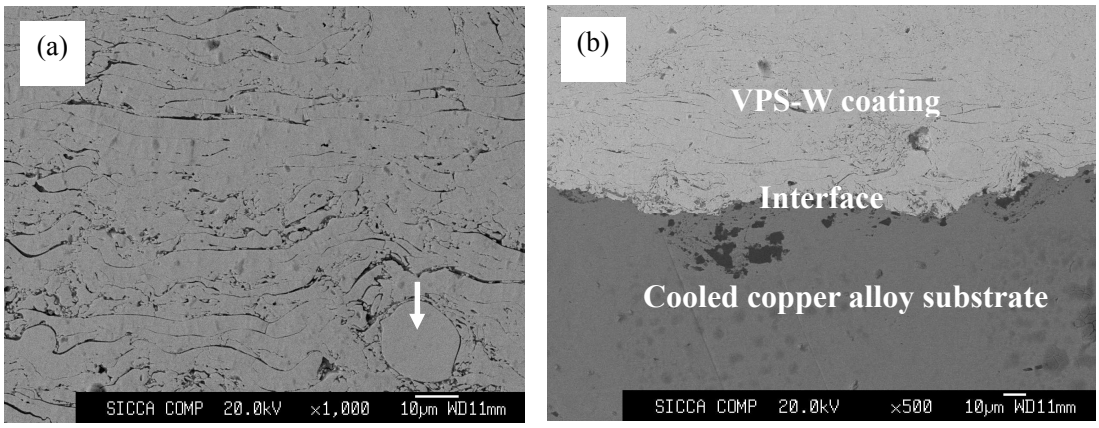

Fig. 2 Cross-section of VPS-W coating: (a) interior of VPS-W coating; (b) interface of VPS-W coating.

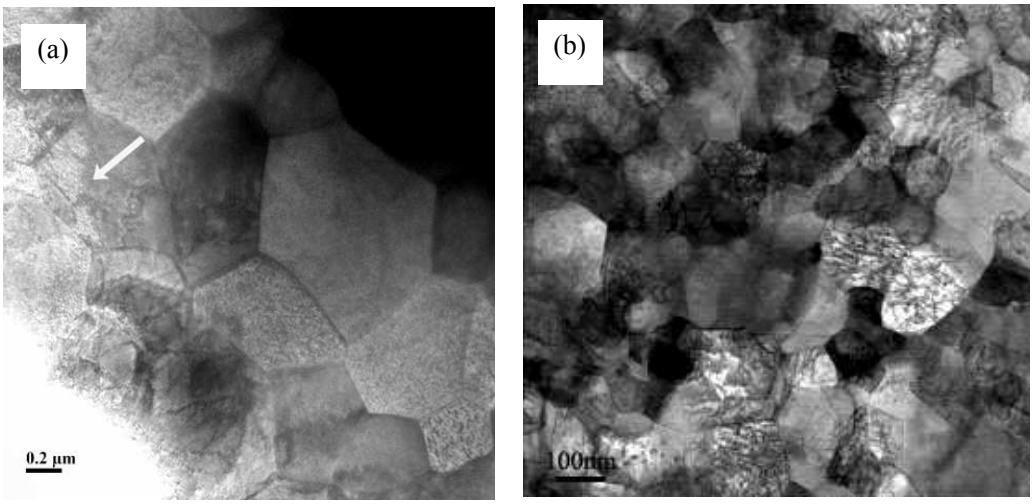

Fig. 3 TEM micrograph of VPS-W coating: (a) interior of VPS-W coating; (b) interface of VPS-W coating.

The TEM images of the transverse section of VPS-W coating were presented in Fig.3. Fig. 3(a) showed that the interior of the coating possessed polycrystalline structure and lots of grains of sizes of 0.5-1μm and irregular shape were observed. Fig. 3(b) expressed the microstructure of the area of VPS-W coating near the interface. It was found that the microstructure of the area near the interface was great different from that of the interior of VPS-W coating. There were grains in size of

nanometers formed. The substrate was cooled down fast by running water. It was thought that the cooling speed of the interface being much faster than that of the interior, which resulted from the fast cooling speed of water-cooled substrate, contributed to the phenomenon. The coefficients of thermal expansion (CTE) between W (4.43×10^{-6} /°C) and Cu (16.8×10^{-6} /°C) was of significant distinction, which would generated residual stress during plasma spraying and may result in bending, microcracking, spalling or delamination phenomena. The water-cooling system which effectively controlled the temperature of substrate was beneficial to reducing the expansion of substrate and therefore the stresses in the coating. It was worth noticing that the phenomenon of mutual diffusion of tungsten or copper atoms was not found at the interface.

The bonding strength of the tungsten coating and copper alloy substrate was about 35±5 MPa, indicating the combination of the coating and substrate was well. The room temperature thermal conductivity is about 105 $W \cdot m^{-1} \cdot K^{-1}$, which was lower than that of bulk tungsten material.

4. Summary

The tungsten coating was prepared on water-cooled copper alloy substrate using vacuum plasma spraying technology. The coating was composed of well-melted tungsten particles and was built up by layers of splats. Grains of 0.5-1μm in irregular shape were formed inside of the coating. The bonding of the coating and the substrate was tight and grains in nanometer size were found in the area near the interface of the coating and substrate. The bonding strength of the coating and substrate was about 35MPa. The thermal conductivity of tungsten coating was about 105 $W \cdot m^{-1} \cdot K^{-1}$ at room temperature.

Acknowledgements

The authors wish to express their thanks to Prof. Guangnan Luo for his constructive proposals and effective discussions during the present study. This work was partly supported by the JSPS-CAS Core University Program in the field of Plasma and Nuclear Fusion.

References

[1] J. Matejicek, P. Chraska, J. Linke, J. Therm. Spray Technol., **16** (2007) 64-83.

[2] T. Hirai, A. Kreter, J. Malzbender, T. Ohgo, V. Philipps, G. Pintsuk, A. Pospieszczyk, Y. Sakaw, G. Sergienko, T. Tanabe, Y. Ueda, M. Wada, Fusion Eng. Des., **81** (2006) 175-180.

[3] D. Matejka, B. Benko, Plasma Spraying of Metallic and Ceramic Materials, John Wiley & Sons Ltd, Czechoslovakia, 1989.

[4] H. Greuner, H. Bolt, B. Boswirth, S. Lindig, W. Kuhnlein, T. Huber, K. Sato, S. Suzuki, Fusion Eng. And Design, **75-79** (2005) 333-338.

[5] B.Riccardi, R. Montanari, M. Casadei, G. Costanza, G. Filacchioni, A. Moriani, J. Nuclear Mater., **352** (2006) 29-35.

Characterization of Dust dynamics in LHD

N. Ashikawa, Y. Tomita, A. Sagara, S.Masuzaki, K.Nishimura and LHD experimental group

1) National Institute for Fusion Science, Toki 509-5292, Japan
e-mail contact of main author : ashikawa@lhd.nifs.ac.jp

Abstract. To investigate the dust properties, their movements were observed by a high-speed (time resolution of 5.3 ms) infrared camera in the Large Helical Device (LHD). Heated dust velocities were estimated to be 1 – 15 m/s in this experiment. We propose a method for revealing the three-dimensional position of heated dust particles using real and reflected images on the wall observed by an infrared camera.
Keywords (bold): Dust dynamics, Fast camera. First

1. Introduction

Investigation of the dust properties in fusion devices, such as their composition, sizes, mechanisms of their production and movement is one of the important issues in next step devices such as ITER from the view points of their impacts of the core plasma properties and safety issues [1]. From macro scale estimation in vessel phenomenon, erosion and re-deposition rates around divertor targets are measured and their modeling is also developed [2-3]. In the other hand, a dust movement for each dust particles is investigated for micro scale phenomena.

Typical investigation methods for various dust properties conducted in fusion devices experimentally are as follows: 1) postmortem dust collection to characterize remaining dusts in vacuum vessel [4-6], 2) observation with high-speed camera to analyze individual dust movements [7], 3) Rayleigh scattering measurement using Thomson scattering system to measure dust density and its spatial profile [8,9], and 4) weight measurement by quartz crystal unit to reveal the growth of the deposition layer [10]. For the safety issues, it is necessary to reveal where dust particles are produced and where they deposit mainly in fusion devices. A theoretical analysis for micron-size spherical shape dust dynamics shows that the velocity of dust particles can be very mobile (velocity of over ~ 10 m/s), and traverse the distances comparable to fusion device radii [11]. Therefore, to predict where dusts deposit, it is necessary to model the dust movement and to compare the model with experimental observations.

In the Large Helical Device (LHD), a large-scale superconducting heliotron–type device with a set of l/m = 2/10 helical coils [12], the postmortem dust collection using a vacuum pumping system with filters was conducted in 2001 [4], 2004 and 2005 [6]. The collected dusts were investigated by using the mass balance method to reveal total weight of dust particles, Energy Dispersive X-ray Spectroscopy (EDX) for analysis of the dust particles composition and Scanning Electron Microscopy (SEM) and Transmission Electron Microscopy (TEM) for analysis of dusts shapes and the size distribution of dust particles. The first wall is made of stainless steel-316L (SS 316L) and divertor plates are made of isotropic graphite (IG430U), respectively. Usually the wall temperature during plasma operation, GDC, and boronization is room temperature and it rises up to 368K when wall baking by hot water is conducted [13, 14]. Mainly two types of dust elements have been observed, and one is spherical-shaped and the other is irregular-shaped dusts. The dominant material of the former type dusts is carbon, and that for the later type is iron. The sizes of carbon and metal dusts are smaller and larger than 1 μm, respectively, and the density increases with decrease of the size. It should be noted that the size distribution is well expressed by an inverse power law size distribution function

(Junge distribution [15]) [4]. Many dust movements have been observed during plasma operations by high-speed cameras for visible and infrared regions, respectively. An infrared camera measurement has an advantage of the good sensitivity to radiation over the visible camera, and thus the infrared camera could measure relatively low temperature dusts moving out of the plasma. This is very useful to reveal dust movements.
In this paper, the observations of the dust movements in LHD using high-speed infrared camera will be presented. A simple theoretical model will be introduced, and the experimental observation will be compared with the model.

2. Experimental setup

In LHD, the high-speed infrared camera, Phoenix in FLIR/Indigo was installed at a viewport which is located at torus outboard side, and its height from the equatorial plane was 0.5 m. The detector type of this infrared camera, is InSb which is sensitive wavelength of 3-5 μm. The camera frame rates depend on the pixel numbers, and 320x254 pixels with 5.3 ms of time resolution was used in this experiment. This time resolution includes an exposure time of 2.4 ms and a data transfer time to memory on the camera of 2.9 ms. Figure 1 shows a schematic drawing of the horizontal cross-section at the height of the camera in LHD, and the field of view of the camera is also shown (insertion). The camera mainly looked at the inner first wall. In the insertion, many tiles can be seen. They are first wall panels made of SS316L as mentioned above, and they are bolted (four bolts per a tile) to the vacuum vessel wall. The distance from the camera to the wall was about 5m.

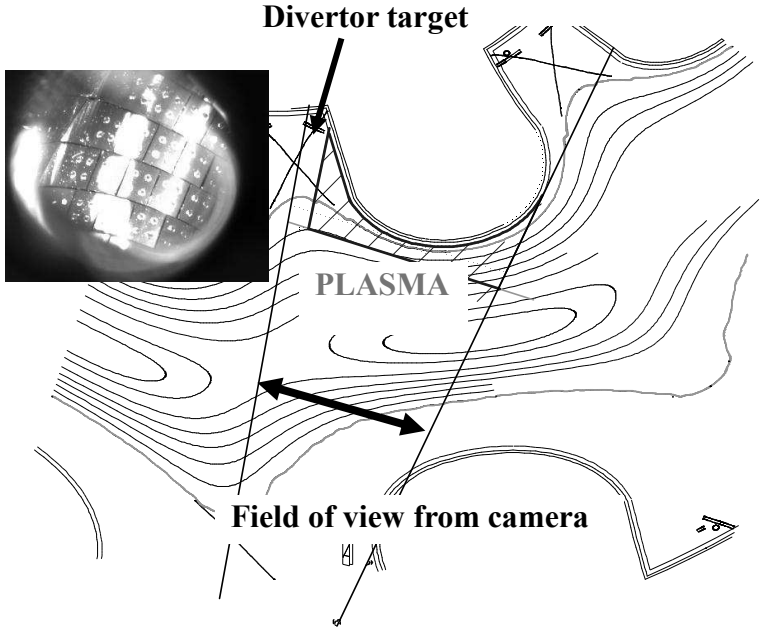

Fig.1 A schematic drawing of the LHD horizontal plane with field of view from infrared camera and a sample image of infrared camera from this field of view. The distance from the infrared camera to the inner wall is about 5m and dust location is estimated in hatched area near the inner wall.

3. Experimental results

The observation of dust particles using the high-speed infrared camera was conducted after the plasma temperature decrease for radiation collapse for many dusts has been observed during this phase. In this case, plasma was not fully collapsed, but neutral beam injection (NBI) heating sustains the low temperature plasma. Such situation can appear for the existence of steady state plasma confinement magnetic surfaces in the heliotron-type device. Dust particles were observed to move various directions, and it seems to be random. It should be noted that we have not detected above mentioned dusts movement by the camera during the glow discharge wall conditioning operation.

We focus on the two dusts, D1 and D2 in Fig. 2, to analyze their movement. Figure 2 shows their movements observed by an infrared camera. Several images are superimposed on these images to show dust trajectories. These two dusts are unique for that their reflection images can be seen on the first wall, and thus, they are considered to move near the inner wall, though the three-dimensional positions of the dusts are not obtained at this stage. Velocities of the dusts on the assumed plane neat the inner wall which is shown in Fig. 1 were estimated, and the time evolutions of the velocity are depicted in Fig.3. As shown in Fig. 2 (a), D1 moved upward straightly, and it seems to move along the helical coil can on this assumed plane. The velocity of dust particle on the plane increased from 5 to 15 m/s during observed time, and it looks to be accelerated with 500m/s^2 in apparent.

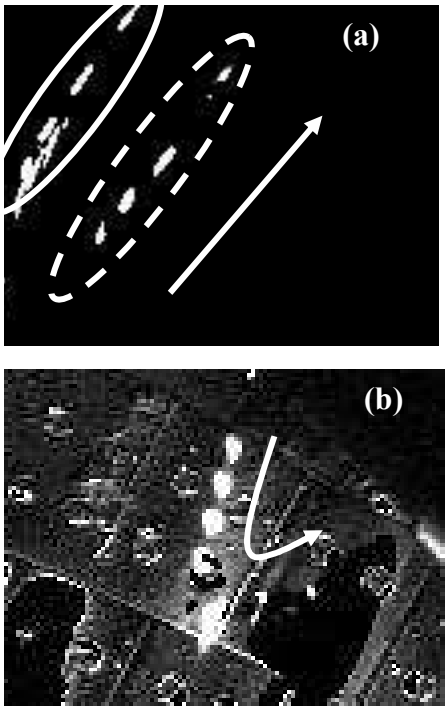

Fig.2 Movement of heated dust particles in after-glow of hydrogen plasma observed by infrared camera. (a) dust, D1, images located in ellipse by solid line and reflected images are shown by dotted line (b) dust, D2, images. Allows show moving directions.

In Fig.2 (b), the distance between real dusts and their reflection images were smaller than those in Fig. 2 (a). The real dust images are indicated at left side in the ellipse by solid line on this picture and their reflected images are shown in the ellipse by dotted line around center of this picture. Apparent velocity of D2 is about 1 to 6 m/s, and is slower than that of D1. Moving direction of D2 is almost vertically downward. After 2.263 s, D2 looks to collide with the wall and then its moving direction is changed clearly as shown in Fig.2 (b). This observation clearly indicates the importance of the dust reflection on the wall to reveal the dust movement.

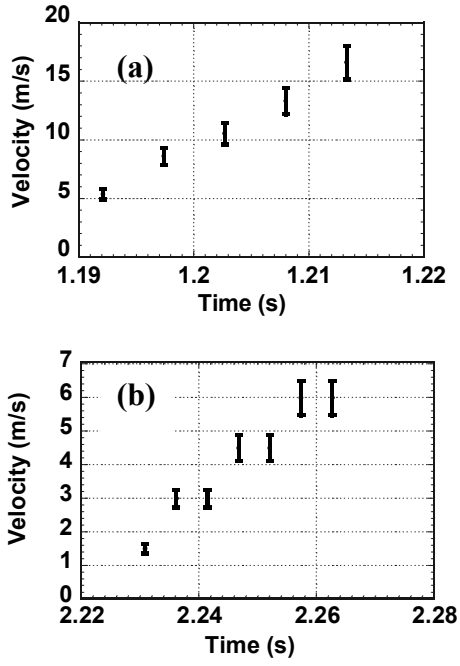

Fig.3 Time evolution of velocity of the dust particle, (a) D1, and (b) D2.

5. Summary

Using the high-speed infrared camera, dust movements were observed in the residual low temperature plasma after radiation collapse in LHD. We focused on the two dusts those real and reflected on the wall radiations could be observed simultaneously. That suggests the dusts were located near the wall. Assumed plane was utilized to analyze the dust movements. The dusts velocities are 1 – 15 m/s in apparent, and they looks to be accelerated. The moving direction of one of dusts was changed clearly after its collision with the wall, and that suggests the interactions between dusts and the wall are important process to predict the dust movement in fusion devices.

We observed the real and reflected images of dust as mentioned above, and we will be able to obtain the real three-dimensional position of dust particles. Unfortunately, we have not obtained that for several technical problems. This is a merit of metallic wall device, and this method can be applied in other fusion devices with metallic wall such as ASDEX-U.

Acknowledgements

This work is supported by a Grant-in-Aid for Scientific Research from Ministry of Education, Science and Culture of Japan (19055005), NIFS budget 07ULPP515 and the JSPS CAS Core University Program in the field of plasma and nuclear fusion.
The authors would like to thank Dr. B. J. Peterson for use of the infrared camera.

References

[1] FEDERICI, G., et al., "Tritium inventory in the ITER PFC's: Predictions, uncertainties, R&D status and priority needs", Fusion Eng. Design **39-40** (1998) 445.
[2] ROTH, J., et al., "Flux dependence of carbon erosion and implication for ITER", J. Nucl. Mater. **337-339** (2005) 970.
[3] KIRSCHNER, A., et al., "Modelling of tritium retention and target lifetime of the ITER divertor using the ERO code", J. Nucl. Mater. **363-365** (2007) 91.
[4] SHARPE, J.P., SAGARA, A., et al., "Characterization of dust collected from ASDEX-Upgrade and LHD", J. Nucl. Mater. **313-316** (2003) 455.
[5] SHARPE, J.P., MASAKI, K., et al., "Characterization of dust collected from NSTX and JT-60U", J. Nucl. Mater. **337-339** (2005) 1000.
[6] KOGA, K., et al., "Characterization of Dust Particles Ranging in Size from 1 nm to 10 μm Collected in LHD", Plasma Fusion Res. to be submitted.
[7] ROQUEMORE, A.L., et al., "3D measurements of mobile dust particle trajectories in NSTX", J. Nucl. Mater. **363-365**(2007) 222.
[8] NARIHARA, K., et al., "Observation of dust particles by a laser scattering method in the JIPPT-IIU tokamak", Nucl. Fusion **37** (1997) 1177.
[9] WEST, P., et al., "Correlation of submicron dust observed in DIII-D during plasma operation with plasma operating parameters", J. Nucl. Meter. **363-365** (2007) 107.
[10] RHODE, V., et al., "On the formation of a-C:D layers and parasitic plasmas underneath the roof baffle of the ASDEX Upgrade divertor", J. Nucl. Mater. **313-316** (2003) 337.
[11] KRASHENINNIKOV, S.I., TOMITA Y., et al., "On dust dynamics in tokamak edge plasmas", Phys. Plasmas **11** (2004) 3141.
[12] MOTOJIMA, O., et al., "Recent advances in the LHD experiment", Nucl. Fusion **43** (2003) 1674-1683.
[13] NISHIMURA, K., et al., "Development of the plasma operational regime in the large helical device by the various wall conditioning methods", J. Nucl. Mater. **337-339** (2005) 431.
[14] ASHIKAWA, N., et al., "Comparison of boronized wall in LHD and JT-60U", J. Nucl. Mater. **363-365** (2007)1352.
[15] JUNGE, C.E., "Air Chemistry and Radioactivity", Academic Press **113** (1965).

Design Integration of the LHD-type Energy Reactor FFHR2 toward Demo

A. Sagara[1], S. Imagawa[1], Y. Kozaki[1], O. Mitarai[2], T. Tanaka[1], T. Watanabe[1], N. Yanagi[1], H. Tamura[1], K. Takahata[1], M. Shoji[1], S. Masuzaki[1], K. Nishimura[1], H. Chikaraishi[1], S. Yamada[1], T. Goto[1], T. Mito[1], T. Muroga[1], N. Nakajima[1], S. Fukada[3,] H. Hashizume[4], Y. Wu[5], O. Motojima[1] and FFHR design group

1National Institute for Fusion Science, Toki, Gifu 509-5292, Japan
2Tokai University, 9-1-1 Toroku, Kumamoto 862-8652, Japan
3Kyushu University, 6-10-1 Hakozaki, Fukuoka, Fukuoka 812-8581, Japan
4Tohoku University, Sendai 980-8579, Japana
5Institute of Plasma Physics, Chinese Academy of Sciences, Hefei, China.
E-mail of corresponding author: sagara.akio@LHD.nifs.ac.jp

Abstract

Three candidates to secure the blanket space are proposed in the direction of reactor size optimization without deteriorating a-heating efficiency and with taking cost analyses into account. For this direction the key engineering aspects are investigated; on 3D blanket designs, it is shown that the peaking factor of neutron wall loading is 1.2 to 1.3 and the blanket cover rate over 90% is possible by proposing Discrete Pumping with Semi-closed Shield (DPSS) concept. On large superconducting magnet system under the maximum nuclear heating of 200W/m^3, CICC and alternative conductor designs are proposed with a robust design of cryogenic support posts. On access to ignited plasmas, new methods are proposed, in which a long rise-up time over 300 s reduces the heating power to 30 MW and a new proportional-integration-derivative (PID) control of the fueling can handle the thermally unstable plasma at high density operations.

Keywords: helical reactor, blanket, COE, nuclear heating, superconducting magnet, ignition

1. Introduction

On the basis of physics and engineering results established in the LHD project, conceptual designs of the LHD-type helical reactor FFHR have made continuous progress from 1991 [1, 2]. Those design activities have led many R&D works with international collaborations in broad research areas [3, 4].

Due to inherent current-less plasma and intrinsic diverter configuration, helical reactors have attractive advantages, such as steady operation and no dangerous current disruption. In particular, in the LHD-type reactor design, the coil pitch parameter γ of continuous helical winding can be adjusted beneficially to reduce the magnetic hoop force (Force Free Helical Reactor: FFHR) while expanding the blanket space, where $\gamma=(ma_c)/(lR_c)$ with a coil major radius R_c, a coil minor radius a_c, a pole number l, and a pitch number m.

2. Candidates to secure the blanket space

The design parameters of FFHR2 are listed in Table 1, which newly includes the recent results of cost evaluation based on the ITER (2003) design. In this base design, one of the main issues is the structural compatibility between blanket and divertor configurations. In particular, the blanket space at the inboard side is still insufficient due to the interference between the first walls and the ergodic layers surrounding the last closed flux surface.

From the point of view of a-heating efficiency over 0.95, the importance of the ergodic layers has been found by collision-less orbits simulation of 3.52MeV alpha particles. Therefore, the reactor size is increased. In this case, as shown in Fig.1, it is expected that there is an optimum size around R_c of 15m by taking into account the cost of electricity (COE), the total capital cost, and engineering feasibility on large scaled magnets.

3. Progress and issues on 3D blanket designs

In the direction of optimizing neutronics performances, the 3D distribution of neutron wall loading is basically important. Under the averaged neutron wall loading of 1.5 MW/m^2, the maximum loading for the uniform and helical source are 2 MW/m^2 and 1.8 MW/m^2, respectively, at the first wall of blankets on the helical coils. Therefore the peaking factor is estimated to be 1.2 to 1.3.

The FFHR blanket designs have been improved to obtain the total TBR over 1.05 for the standard design of Flibe+Be/JLF-1 and long-life design of Spectral-shifter and Tritium Breeding (STB) blanket [2, 3] by enhancement of the blanket cover rate to 80%. More increase of the cover rate over 90% is effectively possible by a new proposal of Discrete Pumping with Semi-closed Shield (DPSS) concept as shown in Fig.2, where the helical divertor duct is almost closed with partly opened at only the discrete pumping ports. This DPSS is very important not only to increase the total TBR over 1.2 but also to reduce the radiation effects on magnets. In fact, as shown in Fig.3, the first neutron fluxes at the poloidal coils just out side the divertor duct and at the side of the helical coils are successfully reduced to the acceptable level lower than 1x10^{22} n/m^2 in 40 years. The total nuclear heating is also reduced from 250kW to 40kW, which means the cryogenics power to be about 12MW and acceptable level below 1% of the fusion output.

Table 1. Design parameters of helical reactor

Design parameters			LHD	FFHR2	FFHR2m1	FFHR2m2
Polarity	l		2	2	2	2
Field periods	m		10	10	10	10
Coil pitch parameter	γ		1.25	1.15	1.15	1.25
Coil major Radius	R_c	m	3.9	10	14.0	17.3
Coil minor radius	a_c	m	0.98	2.3	3.22	4.33
Plasma major radius	R_p	m	3.75	10	14.0	16.0
Plasma radius	a_p	m	0.61	1.24	1.73	2.80
Plasma volume	Vp	m^3	30	303	827	2471
Blanket space	Δ	m	0.12	0.7	1.1	1.15
Magnetic field	B_0	T	4	10	6.18	4.43
Max. field on coils	B_{max}	T	9.2	14.8	13.3	13.0
Coil current density	j	MA/m^2	53	25	26.6	32.8
Magnetic energy		GJ	1.64	147	133	118
Fusion power	P_F	GW		1	1.9	3
Neutron wall load	Γ_n	MW/m^2		1.5	1.5	1.3
External heating power	P_{ext}	MW		70	80	100
α heating efficiency	η_α			0.7	0.9	0.9
Density lim.improvement				1	1.5	1.5
H factor of ISS95				2.40	1.92	1.76
Effective ion charge	Z_{eff}			1.40	1.34	1.35
Electron density	$n_e(0)$	10^19 m^{-3}		27.4	26.7	19.0
Temperature	$T_i(0)$	keV		21	15.8	16.1
Plasma beta	<β>	%		1.6	3.0	4.1
Plasma conduction loss	P_L	MW			290	463
Diverter heat load	Γ_{div}	MW/m^2			1.6	2.3
Total capital cost		G$(2003)		4.6	5.6	6.9
COE		mill/kWh		155	106	87

4. Base design of large superconducting magnet system

The base design for the FFHR2m1 superconducting magnet system has been

preliminary proposed on the engineering base of ITER-TF coils as a conventional option, where the magnet-motive force of helical coils is about 50 MA and the cable-in conduit conductors (CICC) of current 90 kA with Nb3Al strands are wound in the grooves of the internal plates. In this concept, react and wind method is preferred to use conventional insulator and to prevent huge thermal stress. The maximum length of a cooling path is about 500 m that is determined by the pressure drop for the required mass flow against the nuclear heat of 1000 W/m^3. This value has a 5 times margin of the maximum nuclear heating calculated on the FFHR helical coils, in which the gamma-ray heating is dominant and the maximum is about 200 W/m^3.

The total weight of the coils and the supporting structure exceeds 16,000 tons. This weight is supported by cryogenic support posts by adopting the same type of the LHD support post, which is a folded multi plates consisted of Carbon Fiber Reinforcement Plastic (CFRP) and stainless steel plates. The modal and dynamic response analysis using typical earthquake vibrations are the next issue for design optimization.

5. New proposals on access to ignited plasmas

Minimization of the external heating power to access self-ignition is advantageous to increase the reactor design flexibility and to reduce the capital and operating costs of the plasma heating device in a helical reactor. While the fusion power rise-up time in a tokamak depends on the OH transformer flux or the current drive capability, any fusion power rise-up time can be employed in a helical reactor, because the confinement field is generated by the external helical coils. It has been recently found that a lower density limit margin reduces the external heating power,

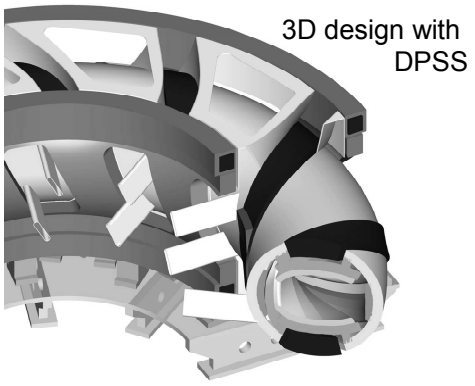

Fig.2 Discrete Pumping with Semi-closed Shield almost closed with partly opened at only th

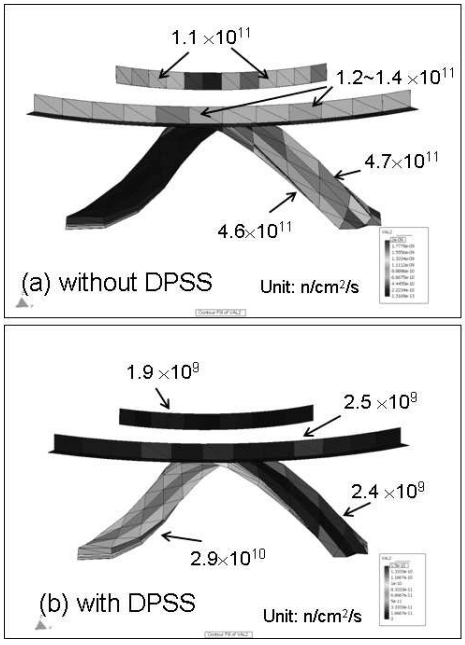

Fig.3 The first neutron fluxes at the poloidal and helical coils (a) without and (b) with the DPSS, where the flux at the rear side of helical coils is high in (a) and one order reduced in (b).

and over 300 s of the fusion power rise-up time can reduce the heating power from such as 100 MW to minimized 30 MW in FFHR2m1 [5].

A new and simple control method of the unstable operating point in FFHR2m1 is proposed for the ignited operation with high-density plasma [6], proportional-integration-derivative (PID) control of the fueling has been used to obtain the desired fusion power

6. Summary

Recent activities on optimizing the base design of LHD-type helical reactor FFHR2m1 is presented. Three candidates to secure the blanket space are proposed in the direction of reactor size optimization without deteriorating a-heating efficiency and with taking cost analyses into account.

On 3D blanket designs, it is shown that the peaking factor of neutron wall loading is 1.2 to 1.3 and the blanket cover rate over 90% is possible by proposing Discrete Pumping with Semi-closed Shield (DPSS) concept. Helical blanket shaping along divertor field lines is a next big issue.

On large superconducting magnet system under the maximum nuclear heating of 200W/m^3, CICC designs of 500 m cooling path and 90 kA with Nb3Al strands and alternative Indirect cooling Nb3Sn conductor designs are proposed with the LHD-type robust design of cryogenic support posts.

On access to ignited plasmas, using the advantage of current-less plasma, new methods are proposed, which are a long rise-up time over 300 s to reduce the heating power to 30 MW and a new proportional-integration-derivative (PID) control of the fueling to handle the thermally unstable plasma at high density operations.

Acknowledgements

This work was partly supported by the JSPS-CAS Core-University Program in the field of “Plasma and Nuclear Fusion”.

References

[1] A. Sagara, O. Motojima, K.Watanabe et al., Blanket and Divertor Design for Force Free Helical Reactor (FFHR), Fusion Eng. and Design, 29 (1995) pp.51-56.

[2] A. Sagara, S. Imagawa, O. Mitarai et al., Improved structure and long-life blanket concepts for heliotron reactors, Nuclear Fusion, 45 (2005) pp.258-263.

[3] A. Sagara, O. Mitarai, S. Imagawa et al., Conceptual design activities and key issues on LHD-type reactor FFHR, Fusion Eng. and Design, 81 (2006) pp.2703-2721.

[4] A. Sagara, T. Tanaka, T. Muroga et al., Innovative Liquid Breeder Blanket Design Activities in Japan, Fusion Sci. and Tech., 47 (2005) pp.524-529.

[5] O. Mitarai, A.Sagara, H.Chikaraishi et al., Minimization of the External Heating Power by Long Fusion Power Rise-up Time for Self-ignition Access in the Helical Reactor FFHR2m, presented at 21st IAEA Fusion Energy Conf., 2006, Chengdu, China.

[6] O. Mitarai, A. Sagara, N. Ohyabu, et al., New Control Method of the Unstable Operating Point in the

FFHR Helical Reactor, Plasma and Fusion Research, Rapid Communications, 2, 021 (2007) .

THE STRUCTURE AND THERMAL ANALYSIS OF ITER EQUATORIAL DIAGNOSTIC PORT PLUG

H.Xie, T.J.Xu, D.M.Yu
Institute of Plasma Physics, Chinese Academy of Sciences

Abstract: The equatorial port plugs is the components in ITER device which will house the complex hardware for diagnostics equipments in vacuum vessel port, as well as nuclear shielding. Because of its complicated constitution and thin shell space structure, the structural and thermal analysis is necessary. According to the results of primary finite element analysis (FEA), the structural reliability can meet the requirements of ITER specifications under the baking condition.

Key words: diagnostic port plug, thermal, structure, finite element analysis

1. Introduction

At the equatorial level, some ITER vacuum vessel ports are used to provide access to the ITER plasma for diagnostics equipments. Filling these ports will be port plugs, which will house the complex hardware for these systems, as well as nuclear shielding. As presently designed, the diagnostics plugs will support first-wall shield modules similar to those lining the rest of the vessel. To remove nuclear heat from the blankets and the front-end structures in these plugs, extensive water-cooling channels will be needed in the plugs. As part of the primary vacuum, these plugs will need low out-gassing and leak rates consistent with ultra-high vacuum conditions, and will be subjected to thermal excursions during bakeout. Base on these requirements, some primary thermal and structure analysis have been done to verify the reliability and feasibility of technology.

2. Structural design for equatorial diagnostic port plug of ITER

The integrated port plug assembly will be inserted into the vacuum vessel port protruding through the blanket back plate to the normal position of the first wall and sealing the primary vacuum at the port flange, as is shown in Fig. 1. The outer portion (outside of vacuum vessel) of equatorial port plug provides vacuum boundary for vacuum vessel, inputs all kinds of pilot signals and outputs all kinds of diagnostic

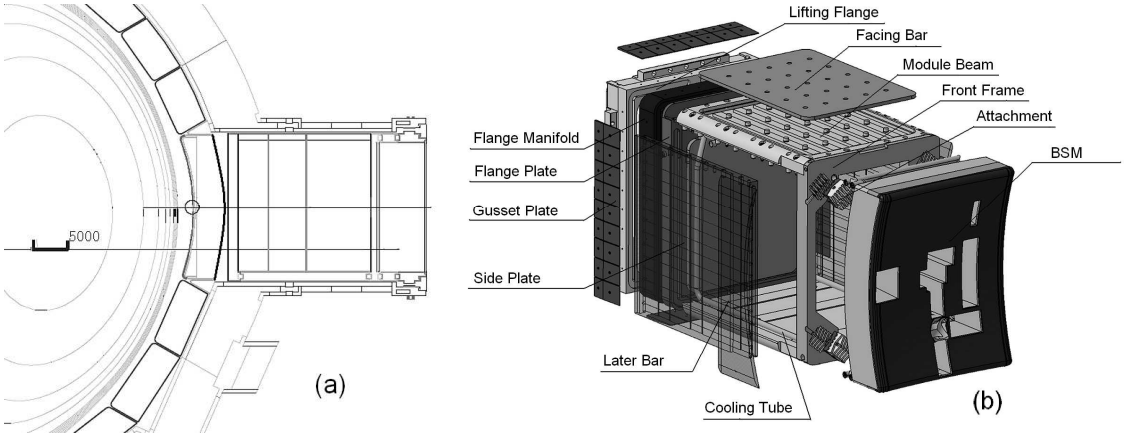

Fig.1 (a) location of port plug in VV port (b) exploded 3-D port plug model

signals. The inner portion (inside of vacuum vessel) provides structure supporting and EM shielding for diagnostic modules and BSM(Blanket Shield Module).

The reference arrangement of equatorial port plug structure has a U shape and continuous top lid, keyed with dowels all round with a rectangular internal aperture for insertion of diagnostic modules from above. The modules for visible IR/TV, soft X ray camera and the collective Thomson scattering etc are fixed to interior space of port plug (not shown in figure).There are an open front frame with first extending diagnostic module, uncooled rear flange plate, welded fabrication of forged flange, and gun-drilled base and side plates. A top plate is made as a sandwich of machined plates seam and spot welded. As one of the key part, BSM should meet the requirements of rigidity, self-alignment, self-load-on and cooling capability.

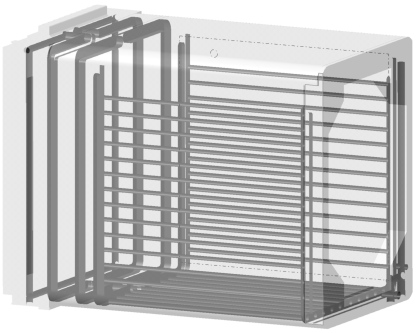

Fig3 The hydraulic circuit of port plug

3. Baking technology of port plug

Baking process can drive out the impurities and gas to get clean ultra-high vacuum condition for plasma current. Whereas, the bakeout will lead to uneven temperature distribution and thermal stress. The proper temperature range is defined from 160 ºC to 200 ºC, some bias data of local region is allowable.

Port plug is a thin-wall structure which has hydraulic pipe inside, therefore, the medium can flow in inner space and bake the port plug. By means of numerical simulation, some basic parameters of circuit, such as distribution of velocity, pressure, temperature and heat flow, can be calculated. The detailed hydraulic circuit layout and flowchart are showed in Fig.3 and Fig.4 respectively.

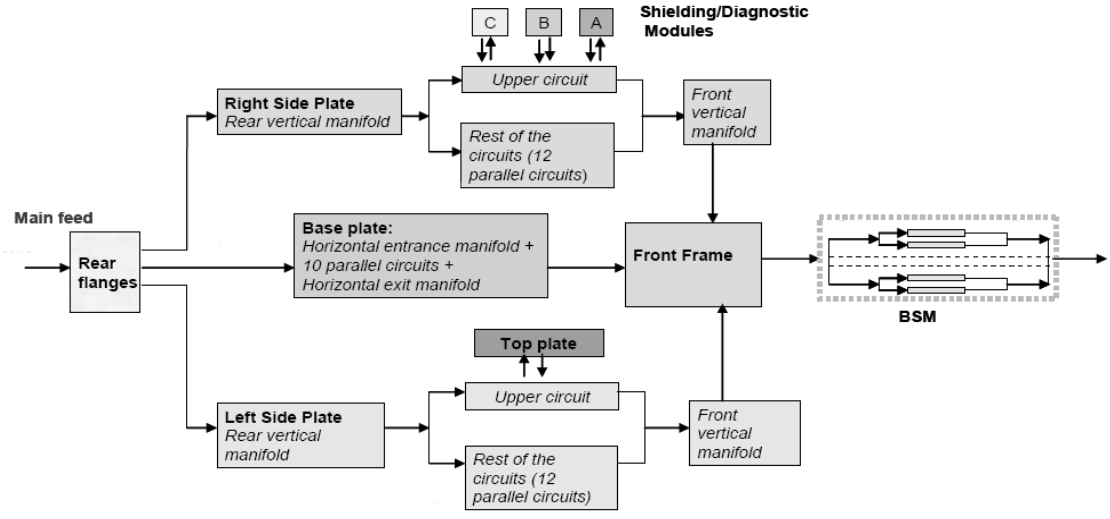

Fig.3 Hydraulic circuit flowchart of the port plug

4. Thermal and structure coupling analysis

4.1 The main parameters and boundary condition

The main material constituting the port plug structure is 316L stainless steel and the medium for heat exchange is hot pressed water. Their main physical parameters are listed in Table.1.

Table 1 The physical parameters of materials

Material	Density Kg/m^3	Specific heat J/Kg.K	Heat conductivity W/m.k	Expansion coefficient/K	Primary stress /MPa
SS316L	7.96×10^3	4.70×10^2	13.94	1.70	147
water(200 ºC)	8.65×10^2	4.51×10^3	0.046	13.77×10^4	

Table 2 The boundary condition for analysis

	Pressure at inlet(MPa)	Pressure at outlet(MPa)	Temperature at inlet(℃)
Medium(Water)	4	0	154

4.2 Thermal analysis

Considering approximate symmetrical configuration of port plug, a model of half plug is used for thermal analysis which is performed by the ANSYS code. The temperature distribution of port plug is shown in Fig 4. The maximum temperature is 197 ºC.

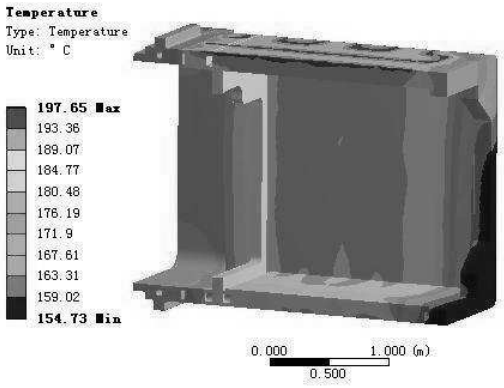

Fig.4 The temperature distribution of port plug (ºC)

4.3 Structural analysis

Structural stress is due to difference of thermal expansion and temperature gradient in different area. Therefore, the result of temperature distribution is used as boundary condition to get structural response, including stress and deformation which are shown in Fig5 and Fig6 respectively. From the analysis of bakeout process it has been found that the maximum stress, 168 MPa, appears in the area of the inner channel and some small local area.

In accordance with the ASME criteria, the maximum von Mises stress (total stress, including the port plug thermal stress, the primary membrane stress and the bending stress) should not exceed three times of material allowable stress.

The allowable stress $[\sigma]$ of SS316L is 147Mpa. Thus, from above analysis, the calculative stress can meet the strength requirements: $\sigma_{max}=P_L+P_b+Q<3[\sigma]$.

The permissible deformation during baking process is below 15mm at radial or cross direction in ITER. The major deformation also appears at some joint area or some corner ends which can be found at lapping interface between the side plate and gusset plate in Fig6. The maximum value is 4.3mm which is lower than requirements.

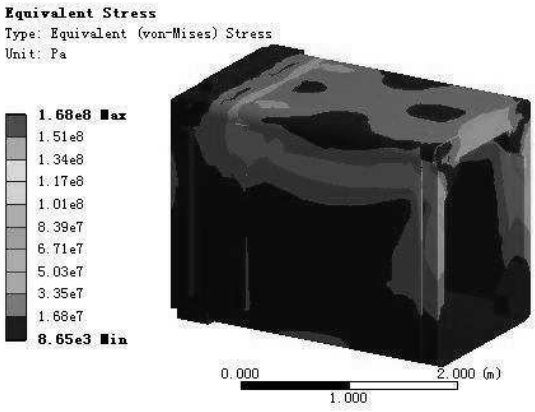

Fig5 The stress distribution of port plug(MPa)

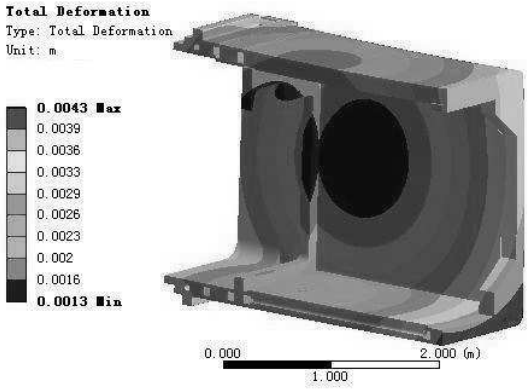

Fig6 The deformation of port plug (m)

5. Summary

The water heating process were put forward to bake the equatorial diagnostic port plug of ITER. The thermal analysis has been carried out to acquire the system temperature and stress distribution. Depending on ASME criteria to verify the the reliability of technology, researching results can provide referenced information to optimize the structure of port plug.

Acknowledgements

This work was partly supported by the JSPS-CAS Core University Program in the field of Plasma and Nuclear Fusion.

Reference:

[1] Doceul L, Walker C, Ingesson C, et al. Fusion Engineering and Design, 2007, 82: 1216~1223

[2] Walker C, Barnsley R, Costley A E, et al. Fusion Engineering and Design, 2005, 74: 685~690

[3] Ciattaglia E, Ingesson L C, Campbell D, et al. Fusion Engineering and Design, 2007, 82: 1231~1237

[7] Li Y B, Wan X G. Superconductivity, 2006, 34(1): 33~36 (in Chinese)

[5] Wan X G, Yao D M, Wang J, et al. Nuclear Fusion and Plasma Physics，2006，26(2): 105~109 (in Chinese)

[6] Liu D Q, Cao Z, Zhou C P, et al. Vacuum, 2003, 2: 31~34 (in Chinese)

[7] Yi L B, Zeng J E, Li G S, et al. Nuclear Fusion and Plasma Physics，2006，26(1): 17~21 (in Chinese)

AGENDA

China-Japan JSPS-CAS Core University Program Seminar on PWI/PFC and Fusion Technologies

Place: Conference Centre at Huangshan International Hotel

Address: No.31 Huashan Road Tunxi, Huangshan (Yellow Mountain) City, Anhui, P.R. China

Date: October 27-29, 2008

Monday, October 27	
8:00	**Opening Address by J.Chen and T.Hino**
	Session 1: Chair Prof.T.Hino and Prof.G.N-,Luo
8:10	**1. Overreview of recent experimental results of HT-7 and EAST** X.Z. Gong, HT-7 and EAST team
8:30	**2. Hydrogen isotope behavior in damaged tungsten by high energy ion beam** Yoshio Ueda，M. Fukumoto, Y. Ohtsuka (Osaka U.), M. Taniguchi, T. Inoue, K. Sakamoto, J. Yagyu, T. Arai (JAEA), I. Takagi (Kyoto U.), N. Yoshida (Kyusyu U.)
8:50	**3. Progress and Status of Chinese Helium-cooled Solid Breeder TBM** Kaiming Feng,G.S. Zhang, T. Yuan, Z. Chen, Z. Zhao, Z.Q. Li, H.B. Liiu, G. Hu, Z. X. Li, X. F. Ye, D.L. Luo,H.Y. Wang, Z. W. Zhou, C.M.Gao, T. Y. Luo, Y. J. Feng
9:10	**4. Deuterium Behavior in the Simultaneous Carbon and Deuterium Ions Implanted Tungsten** Kenji Okuno, Yasuhisa Oya, Yohei Kikuchi, Guangnan Luo, Naoko Ashikawa, Naoaki Yoshida,
9:30	Akio Sagara **5. Recent progress of plasma facing materials at SWIP**
9:50	X.Liu **6. Nano-scale Plasma-Material Interaction in Long-Term Metallic Samples Placed in LHD**
10:05	Tatsuya Tokunaga,Yoshihisa Ohtawa,Naoaki Yoshida(Kyushu University),Masayuki Tokitani,Naoko Ashikawa, Kazuo Kawahata(NIFS) **7. Improvement of Divertor Probes on EAST** W.Zhang
10:20	**Coffee Break**
	Session 2: Chair Prof. M.Matsuyama and Prof. Xiang Liu
10:35	**8. Material Properties of Tungsten Coated F-82H Ferritic/Martensitic Steel as Plasma Facing Armor** Naoaki Yoshida, Yuki Yahiro, Kouichiro Ezato, Satoshi Suzuki, Masato Akiba, Masatoshi Mitsuhara, Hideharu Nakashima
10:55	**9. Vacuum system and wall conditionings in 2008 campaign of EAST** J.S.Hu, X.M Wang, Y.P Zhao, J.G Li and EAST vacuum group
11:15	**10. Deuterium Ion Irradiation Experiment for Tritium Breeding Material and Evaluation of Blanket Tritium Inventory** T.Hino, H. Shibata, Y. Yamauchi, Y. Nobuta, M. Akiba, S. Suzuki, H. Tanigawa
11:35	**11. Project of Tungsten Plasma-facing Materials and Components for EAST** G.N-,Luo and PWI group
11:55	**12. Wall Conditionings Using He, Ne and Ar Gases** Yuji Yamauchi, K. Takeda, Y. Higashi, Y. Nobuta, T. Hino
12:10	**13. The influence of wall condition on hydrogen removal of ICRF cleanings on EAST** Yaowei Yu, Y.W.Yu, J.S.Hu, X.Gao, J.H.Li, Y.Chen and Y.P.Zhao
12:25	**Lunch**

	Session 3: Chair Prof. N.Yoshida and Prof. Y.T.Song
13:30	**14. Tritium Distribution in Surface Layers of Metallic Materials** M.Matsuyama, Z. Chen, K. Nisimura, S. Akamaru, Y. Torikai, Y. Hatano, N. Ashikawa, Y. Oya, K. Okuno, T. Hino
13:50	**15. ERO modelling of hydrocarbon transport and light emission in injection experiments at TEXTOR** Rui Ding, D. Borodin, A. Kirschner,J. Chen, S. Brezinsek, V. Philipps
14:10	**16. Characterization of dust dynamics using high speed camera in LHD** Naoko Ashikawa, Y. Tomita, A. Sagara, S. Masuzaki, K. Nishimura, N. Ohno[1)], G. Kawamura
14:30	**17. Reflection and Diffusion of Atomic Hydrogen on Tungsten Surface: A Molecular Dynamics Study** Z.S.Yang,G.-N Luo
14:50	**18. PWI Study for LHD Based Upon Material Probe** Yuji Nobuta, N. Ashikawa, H. Yagihashi, Y. Yamauchi, T. Hino, S. Masuzaki, K. Nishimura, A. Sagara, N. Oyabu, N. Noda, A. Komori, O. Motojima, and LHD Experimental Group
15:05	**19. Study of Runaway Electrons during Disruptions of Discharges in the HT-7 Tokamak** H.W. Lu, L. Q. HU, S. Y. LIN, G. Q. ZH, and HT-7 team
15:20	**Coffee break**
	Session 4: Chair Prof. Kenji Okuno and Prof. K.M. Feng
15:35	**20. Plasma Facing Components of EAST Tokamak** Y.T. Song
16:55	**21. Tritium Treatment in the Exhaust Gas on LHD Deuterium Experiments** Kiyohiko Nishimura, Y. Asakura, M. Tanaka and T. Kawano
16:15	**22. Preparation and properties of doped carbon for plasma facing component** Z.J. Liu，Q.g.Guo,L.Liu
16:35	**23. Applications of tungsten coated materials for divertor and first wall materials** Kazutoshi Tokunaga, Y.Yahiro, N.Yoshida, N.Ashikawa, M.Tokitani, S.Masuzaki, A.Komori, N. Noda, K.Ezato, S.Suzuki, M.Akiba, A. Kobayashi
16:55	**24. Primary investigation of power deposition pattern on the belt limiter in HT-7** J.F. Ruan, J. L. Chen, J. G. Li, C. Y. Xie
17:10	**25. Characterization of Thick Vacuum Plasma Sprayed Tungsten Coatings on Cooled Copper Alloy Substrate** Y.R. Niu, Xuebin Zheng, Heng Ji, Chuanxian Ding, Junlin Chen, Naoaki Yoshida
17: 25	**26. The strcture and thermal analysis of ITER equatorial diagnostic port plug** H. Xie, T.J.Xu, D.M.Yu
17:40	**End of session**
18:30	**Reception**
Tuesday, October 28	
	Session 5 Chair Prof. Kiyohiko Nishimura and Prof. Y.Wu

8:10 8:30 8:50 9:10 9:30 9:50 10:05	**27. Preliminary Electromagnetic Analysis of Correction Coils for ITER** W.Y. Wu and CC group **28. Design Integration of the LHD-type Energy Reactor FFHR2 toward Demo** Akio Sagara, S. Imagawa,Y. Kozaki, O.Mitarai, T. Tanaka, T. Watanabe, N. Yanagi, H. Tamura, K. Takahata, M. Shoji, S. Masuzaki, K. Nishimura, H. Chikaraishi, S. Yamada, T. Goto, T. Mito, T .Muroga, N. Nakajima, S. Fukada, H. Hashizume, Y. Wu, O. Motojima and FFHR design group **29. R&D Status and Strategy of CLAM and DFLL-TBM Development** Q.Y.Huang and FDS Team **30. Irradiation Effects on Tritium Transport Process in Ternary Lithium Oxide** Yasuhisa Oya, Hirotada Ishikawa, Haibo Liu, Tianyong Luo, Feng Kaiming, Kenji Okuno **31. Tritium Management for Fusion-Based Hydrogen Production Reactor FDS-III** Y.Song, Q. Y. Huang, Y. L. Wang, M.Y. Ni, Y. C. Wu and FDS Team **32. Effect of Thermal Ageing on Mechanical Properties and Microstructure of Reduced Activation Ferritic/Martensitic Steel** Y.F. Li, T. Nagasaka, T. Muroga, Qunying Huang, Yican Wu **33. The superconducting transformer for testing correction conductor short sample** Y. Shi, Yu Wu
10:20	**Coffee break**
  10:35 10:55 11:15 11:35 11:55 12:15	**Session 6 Chair Prof. Akio Sagara and Prof. Q.Y. Huang** **34. Key issues on development of Superconducting magnet technology toward to DEMO.** Arata Nishimura **35. Development of Numerical Solver for Incompressible Multi-Fluid MHD** M.J. Ni **36. Design of Performance Testing System of Superconducting Strand Sampler** J. Qian, Weng Peide, Luo Jiarong, Wu Yu **37. Pb-17Li Acoustic Properties for Ultrasonic Doppler Velocimetry** Takehiko Yokomine, T. Kunugi, Y. Ueki, M. Hirabayashi, T. Yokomine, T. Hinoki, Shimoda and K. Ara **38. Neutronics studies on advanced liquid blanket systems for helical reactor FFHR2** Teruya Tanaka, A. Sagara, Z. Li, T. Muroga, Q. Zeng **39. Proposal of Split and Segmented-type Helical Coils for the Heliotron Fusion Energy Reactor** Nagato Yanagi, K. Nishimura, G. Bansal, A. Sagara, O. Motojima
12:15	**Lunch**
13:30- 17:00	**40. Group Discussions** **(Plasma wall interactions, Plasma facing components, Blanket, Superconducting coils, Demo rector design, Plasma experiments in fusion devices, ITER R&D)**

Wednesday, October 29 2008	
9:00-12:00	**41. Overall Discussions (Future collaborations)**
12:00	**Adjourn**

List of Participants

China-Japan JSPS-CAS Core University Program Seminar on PWI/PFC and Fusion Technologies

	Author	Title	Country	Affiliation	E-mail
1	Tomoaki Hino	Prof.	Japan	Hokkaido University	tomhino@qe.eng.hokudai.ac.jp
2	Yasuhisa Oya	Asso.Prof.	Japan	Shizuoka University	syoya@ipc.shizuoka.ac.jp
3	Kenji Okuno	Prof.	Japan	Shizuoka University	srkokun@ipc.shizuoka.ac.jp
4	Yuji Yamauchi	Asso.Prof.	Japan	Hokkaido University	yamauchi@qe.eng.hokudai.ac.jp
5	Takehiko Yokomine	Asso.Prof.	Japan	Kyushu University	yokomine@ence.kyushu-u.ac.jp
6	Masao Matsuyama	Prof.	Japan	University of Toyama	masao@ctg.u-toyama.ac.jp
7	Yuji Nobuta	Assis.Prof.	Japan	Hokkaido University	y-nobuta@eng.hokudai.ac.jp
8	Yanfen Li		Japan	The Graduate University for Advanced Studies	li.yanfen@nifs.ac.jp
9	Kiyohiko Nishimura	Prof.	Japan	NIFS	nishimura.kiyohiko@LHD.nifs.ac.jp
10	Teruya Tanaka	Asso.Prof.	Japan	NIFS	teru@nifs.ac.jp
11	Akio Sagara	Prof.	Japan	NIFS	sagara.akio@lhd.nifs.ac.jp
12	Arata Nishimura	Prof.	Japan	NIFS	nishi-a@nifs.ac.jp
13	Nagato Yanagi	Assis.Prof.	Japan	NIFS	yanagi.nagato@LHD.nifs.ac.jp
14	Yoshio Ueda	Prof.	Japan	Osaka University	yueda@eei.eng.osaka-u.ac.jp
15	Kazutoshi Tokunaga	Asso.Prof.	Japan	Kyushyu University	tokunaga@riam.kyushu-u.ac.jp
16	Naoko Ashikawa	Assis.Prof.	Japan	NIFS	ashikawa@lhd.nifs.ac.jp
17	Tatsuya Tokunaga	Mr.	Japan	Kyushu university	toku-ta@riam.kyushu-u.ac.jp

18	Naoaki Yoshida	Prof.	Japan	Kyushu University	yoshida@riam.kyushu-u.ac.jp
19	Xianzu Gong	Prof.	China	ASIPP	xz_gong@ipp.ac.cn
20	Liqun Hu	Prof.	China	ASIPP	lqhu@ipp.ac.cn
21	Yuntao Song	Prof.	China	ASIPP	songyt@ipp.ac.cn
22	Weiyue Wu	Prof.	China	ASIPP	wuwy@ipp.ac.cn
23	Guangnan Luo	Prof.	China	ASIPP	gnluo@ipp.ac.cn
24	Xiang Liu	Prof.	China	Southwestern Institute of Physics	xliu@swip.ac.cn
25	Qunying Huang	Prof.	China	ASIPP	qyhuang@ipp.ac.cn
26	Kaiming Feng	Prof.	China	Southwestern Institute of Physics	fengkm@swip.ac.cn
27	Jiansheng Hu	Asso.Prof.	China	ASIPP	hujs@ipp.ac.cn
28	Ming-Jiu Ni	PH.D	China	Graduate University of Chinese Academy of Sciences	mjni@gucas.ac.cn
29	Yadong Li	Dr.	China	ASIPP	yd_li@ipp.ac.cn
30	Chunyi Xie		China	ASIPP	xiecy@ipp.ac.cn
31	Zhongshi Yang		China	ASIPP	zsyang@ipp.ac.cn
32	Han Xie		China	ASIPP	xiehan@ipp.ac.cn
33	Bo Li		China	ASIPP	lib@ipp.ac.cn
34	Hongzhi Liu		China	ASIPP	lzh510@126.com
35	Jiufu Ruan		China	ASIPP	jfruan@ipp.ac.cn
36	Jing Qian		China	ASIPP	jing@ipp.ac.cn
37	Rui Ding		China	Institut für Energieforschung – Plasmaphysik,	rding@ipp.ac.cn

				Forschungszentrum Jülich, Association EURATOM-FZJ, Trilateral Euergio Cluster, D-52425 Jülich, Germany	
38	Yaowei Yu	Student	China	ASIPP	yuyaowei@ipp.ac.cn
39	Yaran Niu	Student	China	Shanghai Institute of Ceramics, Chinese Academy of Sciences, Shanghai	yrniu@mail.sic.ac.cn
40	Yong Song	Dr.	China	ASIPP	ysong@ipp.ac.cn
41	Zhanjun Liu	Dr.	China	Key Laboratory of Carbon Materials, Institute of Coal Chemistry, Chinese academy of Sciences, Taiyuan	zjliu03@sxicc.ac.cn
42	Hongwei Lu	Student	China	ASIPP	luhw@ipp.ac.cn
43	Yi Shi	Student	China	ASIPP	shiyi@ipp.ac.cn
44	Wei Zhang	Student	China	ASIPP	zhangwei@ipp.ac.cn
45	Ju Chen	Student	China	ASIPP	chernju@ipp.ac.cn

Local Organizing Committee

Prof.Junling Chen（ASIPP） jlch@ipp.ac.cn
Ms. Xinfeng Luan (ASIPP) (Tel:) (0)13635609206
Ms. Yuan Wang （ASIPP）(Tel:) (0)13855181152


China-Japan CUP-CAS on PWI / PFC and Fusion Technologies